creative commons

COMMONS DEED

저작자표시-비영리-변경금지 2.0 대한민국

이용자는 아래의 조건을 따르는 경우에 한하여 자유롭게

- 이 저작물을 복제, 배포, 전송, 전시, 공연 및 방송할 수 있습니다.

다음과 같은 조건을 따라야 합니다:

저작자표시. 귀하는 원저작자를 표시하여야 합니다.

비영리. 귀하는 이 저작물을 영리 목적으로 이용할 수 없습니다.

변경금지. 귀하는 이 저작물을 개작, 변형 또는 가공할 수 없습니다.

- 귀하는, 이 저작물의 재이용이나 배포의 경우, 이 저작물에 적용된 이용허락조건을 명확하게 나타내어야 합니다.
- 저작권자로부터 별도의 허가를 받으면 이러한 조건들은 적용되지 않습니다.

저작권법에 따른 이용자의 권리는 위의 내용에 의하여 영향을 받지 않습니다.

이것은 이용허락규약(Legal Code)을 이해하기 쉽게 요약한 것입니다.

Disclaimer

dCollection

공학박사학위논문

특이 파동 조향 및 모드 변환을 위한 반사형 탄성 메타그레이팅

Reflective Elastic Metagratings for Anomalous Wave Steering and Mode Conversion

2023년 2월

서울대학교 대학원

기계항공공학부

김 신 영

특이 파동 조향 및 모드 변환을 위한 반사형 탄성 메타그레이팅

Reflective Elastic Metagratings for Anomalous Wave Steering and Mode Conversion

지도교수 김 윤 영

이 논문을 공학박사 학위논문으로 제출함

2022년 10월

서울대학교 대학원

기계항공공학부

김 신 영

김신영의 공학박사 학위논문을 인준함

2022년 12월

위 원 장 : 김 도 년

부위원장 : 김 윤 영

위 원 : 양 진 규

위 원 : 이 중 석

위 원 : 권 민 우

ABSTRACT

Reflective Elastic Metagratings for Anomalous Wave Steering and Mode Conversion

Shin Young Kim
Department of Mechanical and Aerospace Engineering
The Graduate School
Seoul National University

This dissertation deals with reflective elastic metagratings for anomalous wave steering and mode conversion. Elastic metagratings are newly designed artificial structures governed by the diffraction grating theory and the concept of elastic metamaterials. Recently, elastic metamaterials have been attracting attention as periodic structures which can effectively control the propagation characteristics of elastic waves. Such elastic metamaterials can be practically used in a wide range of industries for patient treatment, non-destructive testing, and vibration absorption by controlling elastic waves and vibrations. However, because of the characteristics of periodic structures, diffraction and interference phenomena of reflected or transmitted waves inevitably occur, and the problem of reduced wave efficiency due

to the occurrence of high-order diffraction modes still has an essential limit in the solution. To overcome this limitation, this thesis proposes novel reflective elastic metagratings which can precisely control the magnitude and direction of each diffraction mode of elastic waves such that wavefronts can be accurately steered as designed.

The goal of this thesis is to realize the anomalous wave steering and mode conversion of elastic waves at the reflection problem in elastic media. By introducing well-designed elastic metagratings, it is possible to solve the innate problem of reduced efficiency of the reflected wave. We solved the problems in two steps. In the first step, the single-mode wave manipulation problem is solved by controlling only the longitudinal waves without considering the shear waves. In this step, several beam-type members are used as the elastic wave scatterers. Based on the theoretical modeling of the members, anomalous steering phenomena of the scattered longitudinal waves are realized through well-designed elastic metagratings. However, it is difficult to control various diffraction modes of the longitudinal and shear waves with beam-type metagratings, because of their few design variables and slender shape which only consider flexural and longitudinal motion. Thus, in the second step, strip-type continuum members with more DOFs including widths are used as wave scatterers to solve the double mode wave manipulation problem which is the simultaneous mode-conversion and steering of the longitudinal (or shear) wave. In this step, diffraction mode amplitudes of longitudinal and shear waves are quantified based on the solution of numerical analysis. Through this analysis, such

mode-converting reflection phenomena are realized through strip-type metagratings. In summary, to achieve the final goal, the design method of reflective elastic metagratings is divided into two steps, and through these steps, high-order diffraction modes of the elastic waves are controlled to realize the anomalous wave steering and mode conversion phenomena. Also, this thesis identifies the phenomena by analyzing the related physics at each step. It is meaningful in that it opens the possibility of practical usage of elastic metagratings by not only experimentally verifying it but also presenting applications in the actual ultrasonic non-destructive testing industry.

Keywords: Elastic metagratings, Diffraction grating theory,
Anomalous wave steering, Elastic mode conversion, Elastic wave scatterers

Student Number: 2016-22851

CONTENTS

ABSTRACT ..... **i**

CONTENTS ..... **iv**

LIST OF TABLES ..... **vii**

LIST OF FIGURES ..... **viii**

CHAPTER 1. Introduction **1**

1.1 Research motivation 1

1.2 Previous works 3

1.3 Research objective and coverage 4

1.4 Outline of thesis 7

CHAPTER 2. Theoretical Background **9**

2.1 Chapter overview 9

2.2 General wave theory in elastic media 10

2.2.1 Elasticity 10

2.2.2 Elastic wave equation 11

2.2.3 Reflection at the traction-free boundary 13

2.3 Diffraction grating theory 15

2.3.1 Grating equation in 1D periodic geometry 16

CHAPTER 3. Elastic Metagratings for Longitudinal Wave Steering **22**

3.1 Chapter overview 22

3.2 Analytical modeling of the elastic wave motion 27

3.2.1 Wave motion in an elastic plate 27

3.2.2 Modeling of the beam-type member 31

3.2.3 Interface coupling conditions 34

3.3 Design of beam-type elastic metagratings.....38

3.4 Design examples 41

3.5 Analysis of the phenomenon 50

3.5.1 Experimental verification 50

3.5.2 Physical interpretation.....52

3.6 Concluding remarks 57

CHAPTER 4. Elastic Metagratings for Anomalous Mode Converting Reflection 70

4.1 Chapter overview 70

4.2 Mathematical descriptions of the wave motion.....75

4.2.1 Full wave motion in an elastic plate 75

4.2.2 Selection of scattered modes 78

4.2.3 Strip-type continuum members 80

4.3 Numerical method for analysis and optimization.....82

4.3.1 Numerical analysis and evaluation.....82

4.3.2 Design optimization method 84

4.4 Design examples 90

4.5 Analysis of the phenomenon 104

4.5.1 Experimental verification 104

4.5.2 Physical interpretation 107

4.6 Concluding remarks 113

CHAPTER 5. Conclusions 129

APPENDIX A. Different optimized solutions for mode-converting reflection 133

APPENDIX B. Transient simulation result and performance 135

APPENDIX C. Effect of the number of beam-type members 138

APPENDIX D. Effect of incidence angle on reflection angle of diffraction modes 141

APPENDIX E. Transfer matrix analysis of mode-converting specular reflection 143

REFERENCES 146

ABSTRACT (KOREAN) 161

ACKNOWLEDGEMENTS 164

LIST OF TABLES

Table 4.1 Number of diffraction modes considered in the metagrating designs... 114

Table 4.2 Initial and optimized values of the design variables in the design optimization. (Initial values were randomly generated)..... 115

LIST OF FIGURES

Fig. 2.1 General case of reflection problem in a traction-free boundary.....19

Fig. 2.2 Two incident case of reflection problem in a traction-free boundary. (a) Longitudinal wave incidence, (b) Shear vertical wave incidence. 20

Fig. 2.3 The periodic slit structure operated as diffraction grating in 1D periodic geometry. The refration of the monochromatic wave in the normal incidence case is presented. 21

Fig. 3.1 A schematic illustration of the elastic metagratings constructed with a periodic array of beam-type members. A unit cell composed of multiple beam-type members is attached to the elastic continuum plate where the longitudinal waves are scattered. 59

Fig. 3.2 The unit cell of the elastic grating with geometric parameters. 60

Fig. 3.3 (a) Illustrations of the longitudinal and flexural motions of a beam-type member. (b) The interface between elastic continuum plate Ω_1 and a beam-type member in Ω_2. 61

Fig. 3.4 The elastic metagrating using a single beam-type member for retroreflection at oblique incidence. (a) The problem definition ($\theta_0 = 60^\circ$, $\theta_{-1} = -60^\circ$), (b) the amplitudes of the normalized modes for the varying length of the beam-type member, (c) numerical simulations of the incident (left) and scattered (right) longitudinal fields, (d) a 2D simulation of the retroreflection from

the elastic metagrating array. 62

Fig. 3.5 The elastic metagratings using two beam-type members for anomalous reflection at normal incidence. (a) The problem definition ($\theta_{\pm1} = \pm60^\circ$), (b) the amplitudes of the normalized mode amplitudes for the varying length of two beam-type members at the gap distance of 0.04 m, (c) numerical simulations of the incident (left) and scattered (right) longitudinal fields, (d) the 2D simulation of the anomalous reflection at the angle of 60° from the elastic metagrating array. 63

Fig. 3.6 The anomalous reflection at normal incidence using the designed beam-type metagrating ($\theta_{\pm1} = \pm45^\circ$, [$L_1, \cdots, L_6$] = [0.02007, 0.02105, 0.05967, 0.06132, 0.06180, 0.06206] m). (b,c) The corresponding wave fields in the periodic unit cell and the 2D simulation results of anomalous reflection, respectively, for the problem defined in (a). (d) The retroreflection using the designed beam-type metagrating ($\theta_0 = 30^\circ, \theta_{-1} = -30^\circ$, [$L_1, \cdots, L_6$] = [0.01666, 0.016, 0.02231, 0.0238, 0.0193, 0.02009] m). (e,f) The corresponding wave fields in the periodic unit cell and the 2D simulation results of retroreflection, respectively, for the problem defined in (d).....64

Fig. 3.7 Beam splitting using the designed metagrating. (a) The problem definition and the designed lengths of the beam-type members ($\theta_{\pm1} = \pm25^\circ, \theta_{\pm2} \approx \pm57.7^\circ$, [$L_1, \cdots, L_6$] = [0.06128, 0.06163, 0.01988, 0.06064, 0.06145, 0.02155] m.), (b) the wave fields in the periodic unit cell,

(c) the 2D numerical simulation of beam splitting at two different angles. 65

Fig. 3.8 Equiangular beam splitting using the design metagrating. (a) The problem definition and the resulted lengths of the beam-type members ($\theta_{\pm 1} = \pm 60^{\circ}$, $\mathrm{Amp}_{-1} : \mathrm{Amp}_{+1} = 1 : 0.85$, [$L_1, \cdots, L_6$] = [0.01970, 0.06509, 0.06109, 0.04680, 0.03658, 0.02075] m.), (b) the wave fields in the periodic unit cell, (c) the 2D numerical simulation of equiangular beam splitting. 66

Fig. 3.9 The experimental setup and result data for verification. (a) The experimental setup with an illustration of the designed elastic metagrating array manufactured in the aluminum alloy plate. (b) The variation of the normalized amplitudes of the reflected longitudinal wave for the anomalous reflection considered in Fig. 3.6(a). (c) The variation of the normalized amplitudes of the reflected longitudinal wave for the beam splitting considered in Fig. 3.7(a).....67

Fig. 3.10 The reflected longitudinal wave fields and the phase profiles over the subcells. (a) The phase profiles in subcells of the metagrating for the abnormal reflection considered in Fig. 3.6(a) and the plot of the phase shift in the scattered longitudinal waves. (b) The phase profiles in subcells of the metagrating for the beam splitting considered in Fig. 3.7(a) and the plot of the phase shift in the scattered longitudinal waves. 68

Fig. 3.11 The reflected longitudinal wave fields and the phase profiles over the

subcells. The phase profiles in the subcells of the metagrating considered in (a) Fig. 3.4(a) and (b) Fig. 3.5(a). The phase shifts in the scattered longitudinal waves are plotted.....69

Fig. 4.1 Conceptual illustrations of the multiply scattered diffraction modes and targeting mode-converting phenomena in this chapter. (a) Multiply scattered longitudinal and shear wave modes from a periodically structured boundary. (b) mode conversion and wave steering realized by the metagratings. ... 116

Fig. 4.2 Theoretical number of propagating diffraction modes in the scattered wave field with respect to the normalized periodicity of the unit cell and the incident angle. (a) Longitudinal wave incidence, (b) shear wave incidence. 117

Fig. 4.3 Configuration of the periodic unit cell of the proposed strip-type metagratings with boundary conditions for numerical analysis and evaluation. (a) Geometrical dimensions of rectangular strip members in the infinitely periodic unit cell, (b) boundary conditions together with the lines for force exitation and spatial FFT. 118

Fig. 4.4 Problem definition and results of Case 1 for longitudinal-to-shear wave mode conversion with a specular angle of $\theta_{s,ref}^{0} = 0°$. (a) Illustration of the reflected and suppressed diffraction modes, (b) number of propagating diffraction modes, (c) convergence history during optimization, (d,e) comparison of the scattered diffraction modes of longitudinal and shear waves, respectively, before and after optimization, (f) comparison of the

scattered wave fields from the initial and designed unit cells, (g) scattered shear wave field from the multiply arranged unit cells. 119

Fig. 4.5 Problem definition and results of Case 2 for longitudinal-to-shear wave mode conversion with a target reflection angle of $\theta_{s,ref}^{+1} = 45°$. (a) Illustration of the reflected and suppressed diffraction modes, (b) number of propagating diffraction modes, (c) convergence history during optimization, (d,e) comparison of the scattered diffraction modes of longitudinal and shear waves, respectively, before and after optimization, (f) comparison of the scattered wave fields from the initial and designed unit cells, (g) scattered shear wave field from the multiply arranged unit cells. 120

Fig. 4.6 Problem definition and results of Case 3 for shear-to-longitudinal wave mode conversion with a target reflection angle of $\theta_{p,ref}^{+1} = 62°$. Note that the unit cells were already configured with the designed geometrical dimensions. (a) Illustrations of the reflected and suppressed diffraction modes, (b) number of propagating diffraction modes, (c) convergence history during optimization, (d,e) comparison of the scattered diffraction modes of longitudinal and shear waves, respectively, before and after optimization, (f) comparison of the scattered wave fields from the initial and designed unit cells, (g) scattered longitudinal wave field from the multiply arranged unit cells. 121

Fig. 4.7 Problem definition and results of Case 4 for splitting an incident longitudinal

wave into both longitudinal and shear waves with reflection angles of $\theta_{p,ref}^{+1} = 70°$ and $\theta_{s,ref}^{-1} = -33°$, respectively. (a) Illustration of the reflected and suppressed diffraction modes, (b,c) comparison of the scattered diffraction modes of longitudinal and shear waves, respectively, before and after optimization, (d) comparison of the incident and scattered wave field from the designed beam-splitting metagrating unit cell, (e,f) scattered longitudinal and shear wave fields from the multiply arranged beam-splitting metagrating unit cells, respectively. 122

Fig. 4.8 Problem definition and results of Case 5 for splitting an incident shear wave into both longitudinal and shear waves with reflection angles of $\theta_{p,ref}^{0} = 0°$ and $\theta_{s,ref}^{+1} = 50°$, respectively. Note that the unit cells were already configured with the designed geometrical dimensions. (a) Illustration of the reflected and suppressed diffraction modes, (b,c) comparison of the scattered diffraction modes of longitudinal and shear waves, respectively, before and after optimization, (d) comparison of the incident and scattered wave fields from the designed beam-splitting metagrating unit cell, (e,f) scattered longitudinal and shear wave fields from the multiply arranged beam-splitting metagrating unit cells, respectively. 123

Fig. 4.9 Application of the proposed metagratings (Case 6): reflection-type mode converter for nondestructive evaluation. (a) Problem definition with two rectangular blocks on which the metagrating plane is attached, (b)

Illustration of the targeting diffraction shear mode, (c) incident longitudinal wave field to and scattered longitudinal wave field from the designed metagrating plane, (d) scattered shear wave propagation through the thick aluminum plate. 124

Fig. 4.10 Experimental setup and measurement data for verifying the beam-splitting metagratings designed in Case 4 (as shown in Fig. 4.7). (a) Experimental setup with the manufactured beam-splitting metagrating array in the 1-mm thick aluminum alloy plate, (b,c) comparison of the experimental and numerical results for beam splitting to (b) longitudinal wave reflection with a target angle of $\theta_{p,ref}^{+1} = 70°$, (c) shear wave reflection with a target angle of $\theta_{s,ref}^{-1} = -33°$. 125

Fig. 4.11 Experimental measurements and numerical simulations for the beam-splitting metagratings including comparison of the traction-free boundary and metagrating. (a) The power of scattered longitudinal and (b) shear wave fields. 126

Fig. 4.12 The surface impedance analysis for the mode-converting specular reflection. (a) The line A-A' where the stress and velocity data for surface impedance calculation are extracted, (b-e) the components of surface impedance with respect to the unit cell line length. 127

Fig. 4.13 The surface impedance analysis for the mode-converting anomalous reflection. (a) The line A-A' where the stress and velocity data for surface

impedance calculation are extracted, (b-e) the components of surface impedance with respect to the unit cell line length. 128

Fig. A.1 The scattered wave fields from the designed metagrating unit cells with different initial values in Cases 1 and 2 in chapter 4. (a) Case 1: the longitudinal-to-shear wave mode conversion with the specular reflection, (b) Case 2: the longitudinal-to-shear wave mode conversion with the reflection angle of $\theta_{s,ref}^{+1} = 45°$ 134

Fig. B.1 The transient analysis of mode-converting anomalous reflection. The transient simulation result at (a) $t = 86\ \mu s$, (b) $t = 264\ \mu s$ 137

Fig. C.1 The performance of metagratings in the respect of the number of beam-type members. The problem is an anomalous longitudinal wave steering with the reflection angle of 60° in Fig. 3.5. The numerical simulation result are presented in both scattered divergence field and FFT in spatial domain using (a) two beam-type members, (b) four beam-type members, (c) six beam-type members. 140

Fig. D.1 The reflection angle of diffraction modes with respect to the periodicity of structure. The longitudinal wave case for (a) normal incidence, (b) oblique incidence of 45° 142

Fig. E.1 The reflection problem of anisotropic effective medium when longitudinal wave normally incidents. (a) The problem definition of reflection problem. (b) Homogenization result showing same performance as proposed

metagratings. 145

CHAPTER 1.
Introduction

1.1 Research motivation

Modern societies of mankind are surrounded by elastic media such as metal, rock, and plastic. These elastic media can be used for the materials of buildings, bridges, airplanes, automobiles, ships, etc. Therefore, the detection of defects in elastic materials and maintenance of mechanical structures become much crucial to protect against potential hazards that lie within the materials.

To detect tiny invisible defects inside solid elastic media, elastic waves have been applied in the field of structural health monitoring [1] and ultrasonic nondestructive testing [2]. Here, elastic waves are energy (or power) carrying disturbances that travel through various elastic media. It should be much easier to detect the defects by using elaborately controlled elastic waves. To achieve high performance in the applications, the propagating mode and direction in the scattered wave field must be efficiently manipulated. However, the efficient mode conversion and wave steering of elastic waves remain challenging, owing to the complex polarization and dispersive properties of elastic wave motions. Even under the incidence of a single-mode elastic wave, various wave modes are scattered in different directions from

boundaries or inhomogeneous interfaces [3,4]. For example, when a longitudinal wave impinges on the arbitrary boundary of an elastic plate, both the longitudinal and shear wave propagate to multiple directions in the scattered field. As a conventional way to manipulate the reflected waves, one can consider taper-shaped wedges used for mode conversion of elastic waves in industrial applications; the tapered wedges are designed to achieve a total internal reflection defined by the critical angle at which only one type of elastic wave can propagate, while other types of waves become evanescent [2,3]. However, the conventional wedge applications employing critical angles are strongly dependent on the working conditions; thus, the efficiency of mode conversion and wave steering is generally poor. Hence, efficient mode conversion and wave steering are still required in elastic wave applications.

In this circumstance, man-made engineered structures called metamaterials are widely studied for anomalous controlling of waves in various media. These metamaterials are thought to have the potentials that can make remarkable outputs in elastic mode conversion and wave steering. Among these metamaterials, metagratings have received much attention for the high performance of steering the wavefronts. Metagratings are newly designed artificial structures governed by the diffraction grating theory and the concept of elastic metamaterials. Throughout the thesis, elastic metagratings will be studied in more detail and applied to solve the problem of anomalous wave steering and mode conversion. In the following sections, previous works on metamaterials, metasurfaces, and metagratings will be briefly

reviewed. Then, the research objective along with the coverage and outline of the thesis will be presented.

1.2 Previous works

As artificially engineered structural materials, metamaterials have attracted considerable attention in recent decades, because they can realize and tailor extreme characteristics in wave propagation [5-12]. Various metamaterials have been proposed for mode conversion or filtering of elastic waves by using anisotropic properties [13-15], negative mass and stiffness [16-18], Fabry–Pérot resonance [19-21], and bimodal impedance matching [22,23]. In [19-21], using the Fabry–Pérot resonance, an incident longitudinal (shear) wave was entirely converted via an anisotropic metamaterial layer into a shear (longitudinal) wave. Recently. A perfect transmission of obliquely incident elastic waves has been reported [24]. While these metamaterials facilitated highly efficient mode conversion in the refraction and transmission of elastic waves, anomalous wave steering in the reflective wave field was not investigated.

Metasurfaces, which are planar versions of metamaterials have been popularly studied for the anomalous steering of elastic waves. In most of the metasurface works, the generalized Snell's law [25] has been employed to realize the anomalous steering of reflected and/or refracted waves by forming various types of phase gradients. Among metasurfaces for elastic wave steering, aligned gaps were set in an elastic

plate to produce phase gradients for steering longitudinal and flexural waves [26,27]. An effective mass-stiffness substructuring model was proposed to refract longitudinal waves in an elastic plate [28]. The disordered pillar resonators were installed on an elastic plate for anomalous deflection and focusing of flexural waves [29]. However, most metasurfaces based on phase gradients inevitably generate undesired multiply scattered modes, because multi-dimensional non-local effects are not fully considered in wave scattering phenomena [30]. In other words, the generalized Snell's law has no mechanism for controlling the scattered modes from the boundaries and inhomogeneous interfaces of the wave-propagating media. Consequently, the wave steering efficiency of phase gradient-based metasurfaces is inherently low, and the mode conversion functionality is fundamentally limited.

To selectively manipulate undesired multiply scattered modes, researchers have investigated metagratings that are governed by the diffraction grating theory [31,32] for electromagnetic [30,33-36] and acoustic wave fields in fluids [37-57] and, very recently for elastic wave field in solids [58-62]. In the metagrating used to manipulate flexural waves, point scatterers based on a mass-spring model were arranged [58,59] and phased grating elements were added to a superstrate of the elastic plate to manipulate guided waves [60].

1.3 Research objective and coverage

This work aims to solve the problem of simultaneous wave steering and mode

conversion in elastic media. The problem will mainly focus on the reflection problem of in-plane elastic waves. It should be noted that accurately controlling the propagating direction and amplitude of each scattered elastic wave is difficult because of the innate coupling motion of longitudinal and shear waves. Therefore, quantifying each diffraction mode of scattered wave and controlling is the main issue. In this point of view, recently researched elastic metagratings will be investigated thoroughly. By using such elastic metagratings, we can solve the issues by calculating the magnitudes of diffraction modes and accurately controlling each of them.

We will solve the problems in two steps. In Step 1, the problem of wave steering and mode conversion is simplified into controlling only the longitudinal wave without considering the shear wave. Here, we used an array of beam-type members to design metagratings that can control longitudinal waves successively. With these beam-type members, the elastic media and members are modeled theoretically. However, these beam-type members only consider longitudinal and flexural motion. Therefore, scatterers consisting of metagratings should have more degree of freedom on the motions and design parameters. In this point of view, we proposed two or three strip-type continuum members to control both the longitudinal and shear waves in Step 2. Because it is difficult to model the strip-type continuum members theoretically, we analyzed our proposed metagratings through the numerical method. As design examples, several anomalous mode-converting reflections are realized numerically and experimentally. In both of the steps, we physically interpreted each phenomenon

induced by metagrating structures.

The research objectives in the dissertation can be summarized as follows.

1. Elastic metagratings for longitudinal wave steering

In this step, we newly propose a novel elastic metagrating model to realize anomalous steering of longitudinal waves in an elastic continuum medium. Modeled by a periodic arrangement of a single or array of so-called beam-type elastic members, the present elastic metagratings resolve the difficulties in steering a specific scattered mode of elastic longitudinal waves by suppressing undesired modes in the scattered wave field. As the metagratings are attached to a boundary of the elastic continuum, both longitudinal and flexural motions in the beam-type members are so coupled with elasticity wave solutions in the elastic medium as to thoroughly manipulate the reflected longitudinal waves from the interface. A set of appropriate geometric parameters of the beam-type members are searched for direct control of the scattered modes quantitatively. As practical applications, the proposed elastic metagratings are applied to realize anomalous reflections and asymmetric splitting of longitudinal elastic waves. As well as experimental verifications, the performance of the designed elastic metagratings is physically interpreted from the perspective of phase modulation.

2. Elastic metagratings for anomalous mode-converting reflection

In this step, we propose a new way for converting a normally incident elastic longitudinal (or shear) wave mode to an obliquely reflected elastic shear (or longitudinal) one, using metagratings of elaborately designed and arranged strips. For a longitudinal (or shear) wave incidence upon the free end of an elastic plate, it is intrinsically difficult to realize full-power mode conversion and steer the converted mode without generating undesired reflected waves. We show that our elaborately designed and optimized multiple rectangular strip-type metagratings are effective in simultaneously fulfilling the mode conversion and anomalous steering of elastic waves. Unlike metasurfaces, the proposed metagratings operate via the diffraction theory and multiple rectangular strips permit sufficient design freedom to fulfill the two design objectives. Several numerical simulations in this work show that the proposed strip-type metagratings achieve near-perfect mode-conversion efficiencies reaching 96 %, and the performance is supported by experiments. Applications of the designed metagratings in nondestructive evaluation are also demonstrated.

1.4 Outline of thesis

The thesis is organized as follows.

In **Chapter 2**, the theoretical background of the waves in elastic media and diffraction grating theory are provided. The general wave theory in elastic media is first presented. In this section, the elastic wave equation as well as a reflection at the traction-free boundary is theoretically described. Since our problem is mainly focused on the reflection problem, such a description process is reasonable. In

addition, the description of diffraction grating theory is briefly introduced.

In **Chapter 3**, the study of elastic metagratings for longitudinal wave steering is presented. This chapter is the first step in solving the main goal of the thesis. Analytical modeling of the elastic wave motion is first provided with the description of the wave motion in an elastic plate and the beam-type members. Then, the design of the proposed beam-type elastic metagratings is introduced using our analytical modeling. Several design examples are presented next. Finally, the experimental verification as well as the physical interpretation is given.

In **Chapter 4**, the study of elastic metagratings for anomalous mode converting reflection is presented. Even though we designed metagratings with beam-type members, controlling all of the modes of elastic metagratings is not a simple task. Therefore, we applied the numerical method in the design of metagratings throughout the chapter. Mathematical descriptions of the wave motion are first provided. Then, the numerical method for analysis and optimization is given. Some of the design examples along with the analysis of the phenomenon are presented.

In the last chapter, the conclusions of the thesis are described.

CHAPTER 2.

Theoretical Background

2.1 Chapter overview

In this chapter, we will present the theoretical background of wave behavior in elastic media and the diffraction grating theory. Since our dissertation deals with the elastic metagratings which are the types of diffraction grating applied in the elastic wave field, it is worthy for reviewing both general wave theory in elastic media and discussing about the diffraction grating theory. In the following section, we first introduce the basic equations of elastic waves. From the solution of elastic wave equations, we solve the problem of reflection at the traction-free boundary. Our main problem is concentrated at the reflection problem, so the phenomena when the longitudinal or shear wave incidents to the traction-free boundary is reviewed in detail. Finally, the basic diffraction grating theory is reviewed. This concept will be used in following chapters, so it is essential to provide the background details in this chapter.

2.2 General wave theory in elastic media

2.2.1 Elasticity

Elastic waves are waves which propagate through elastic medium such as steel, aluminum, wood, etc. Due to complicated natures of elastic medium, the strain, stress, and stiffness should be expressed using second and fourth order tensor. Firstly, displacement vector using the Cartesian coordinate system can be expressed as:

$$\mathbf{u} = \sum_{i=1}^{3} u_i \mathbf{e}_i = u_i \mathbf{e}_i . \tag{2.1}$$

From Eq. (2.1), the strain in second order tensor can be expressed as:

$$\varepsilon_{ij} = \frac{1}{2}(u_{j,i} + u_{i,j}), \quad (i, j = x, y, z) \tag{2.2}$$

where ε_{ij} is the strain on *ij* plane and $u_{i,j}$ denots the derivative of the *i*-th component of displacement in terms of the *j*-th component of displacement.

Using linearized constitutive equation (or Hooke's law) in elastic media which is valid for small deformation, stress tensor can be expressed as:

$$\sigma_{ij} = C_{ijkl}\varepsilon_{kl} \quad (i, j, k, l = x, y, z), \tag{2.3}$$

where σ_{ij} is the stress on *ij* plane, C_{ijkl} is the component of the stiffness tensor (fourth order tensor) *C*. The stiffness tensor *C* can be expressed in 6 by 6 matrix and the components differ by the characteristics of the elastic medium. Some examples of characteristics of elastic media are isotropic, anisotropic, orthotropic, etc. In our case, we will mainly discuss the isotropic elastic media in a plane-stress condition.

Such constitutive relation can be written as follows:

$$\begin{bmatrix} \sigma_{xx} \\ \sigma_{yy} \\ \sigma_{zz} \\ \sigma_{yz} \\ \sigma_{zx} \\ \sigma_{xy} \end{bmatrix} = \frac{E}{1-\nu^2} \begin{bmatrix} 1 & \nu & \nu & 0 & 0 & 0 \\ \nu & 1 & \nu & 0 & 0 & 0 \\ \nu & \nu & 1 & 0 & 0 & 0 \\ 0 & 0 & 0 & 1-\nu & 0 & 0 \\ 0 & 0 & 0 & 0 & 1-\nu & 0 \\ 0 & 0 & 0 & 0 & 0 & 1-\nu \end{bmatrix} \begin{bmatrix} \varepsilon_{xx} \\ \varepsilon_{yy} \\ \varepsilon_{zz} \\ 0 \\ 0 \\ 2\varepsilon_{xy} \end{bmatrix}, \tag{2.4a}$$

or

$$\sigma_{ij} = \lambda \varepsilon_{kk} \delta_{ij} + 2\mu \varepsilon_{ij}, \tag{2.4b}$$

where E, ν each denote Young's modulus and Poisson's ratio in elastic media, respectively. And λ and μ denote for Lamé constants which are material-dependent quantities arise in strain-stress relationships. Here, in the condition of isotropic medium and plane-stress condition, $\lambda = \nu E / (1-\nu^2)$, $\mu = G$.

2.2.2 Elastic wave equation

By Newton's 2nd law, the equation of motion can be written using the stress and displacement as:

$$\sigma_{ji,j} + b_i = \rho \frac{\partial^2 u_i}{\partial t^2}, \tag{2.5}$$

where b_i and ρ each denote the body force acts on the entire elastic body and the density of the medium, respectively.

By substituting Eq. (2,2) and Eq. (2.4) into Eq. (2.5), we can get the governing equation in terms of displacement as:

$$(\lambda+\mu)u_{k,ik}+\mu u_{i,kk}=\rho\frac{\partial^2 u_i}{\partial t^2}. \tag{2.6}$$

By using Helmholtz decomposition of a displacement vector and vector identities, we can get:

$$\nabla\left[(\lambda+2\mu)\nabla^2\varphi-\rho\ddot{\varphi}\right]+\nabla\times\left[\mu\nabla^2\boldsymbol{\psi}-\rho\ddot{\boldsymbol{\psi}}\right]=0, \tag{2.7}$$

where φ and ψ denote scalar and vector potential function.

Since these potential are independent to each other, we can get two wave equations of elastic media as follows:

$$\nabla^2\varphi=\frac{1}{c_d^2}\ddot{\varphi}, \tag{2.8a}$$

$$\nabla^2\boldsymbol{\psi}=\frac{1}{c_s^2}\ddot{\boldsymbol{\psi}}. \tag{2.8b}$$

where $c_d\left(=\sqrt{(\lambda+2\mu)/\rho}\right)$, $c_s\left(=\sqrt{\mu/\rho}\right)$ each denote the dilatational wave speed, shear wave speed, respectively. Dilatational wave can be also called as longitudinal wave or P-wave. And shear wave can be also called as transverse wave or S-wave. In this dissertation, we will use the term “longitudinal wave” or “P-wave” and “shear wave” or “S-wave”. For the characteristics of each wave, the displacement field of longitudinal wave directed along the propagating direction. This means that the vibration direction of elastic medium is coincident with the propagating direction of the longitudinal wave. On the other hand, the particle

motion of the shear wave is normal to the propagating direction. This means that the vibration direction of elastic medium is normal to the propagating direction of the shear wave.

For the general solution of the elastic wave, there needs some assumptions. First, plane wave which means the infinite beam width should be assumed. Next, time-harmonic wave ($\sim e^{-j\omega t}$) is assumed. From such conditions, solutions for the longitudinal and shear wave can be written as (positive propagating direction only):

$$\varphi = P e^{i(\mathbf{k}_p \cdot \mathbf{x} - \omega t)}, \tag{2.9a}$$

$$\psi = S e^{i(\mathbf{k}_s \cdot \mathbf{x} - \omega t)} \tag{2.9b}$$

where P and S are the amplitudes of longitudinal and shear waves, ω is the angular frequency, and $\mathbf{k}_{p(s)}$ denotes the wave vector of longitudinal (shear) wave. In addition, $\mathbf{x}$ denote the position vector using the Cartesian coordinate system.

2.2.3 Reflection at the traction-free boundary

In this section, we will solve the problem of reflection at the traction-free boundary. We will assume the wave as plane, time-harmonic wave. In addition, elastic half-plane with plane strain condition is considered.

Under these assumptions, general case of incident and reflected longitudinal and shear wave (shear-vertical in detail) is shown in Fig. 2.1. In Fig. 2.1, Each of the longitudinal φ_i and shear wave ψ_i incidents to the traction-free boundary in the

angle of α_i and β_i, respectively. Then, the longitudinal and shear wave can be reflected with the angle of α_r and β_r from the traction-free boundary. So our concern is what happens to the reflected longitudinal and shear wave.

Total wave fields can be written as follows:

$$\varphi_{total} = P_i e^{i(\mathbf{k}_{ip}\cdot\mathbf{x}-\omega t)} + P_r e^{i(\mathbf{k}_{rp}\cdot\mathbf{x}-\omega t)}, \tag{2.10a}$$

$$\psi_{total} = S_i e^{i(\mathbf{k}_{is}\cdot\mathbf{x}-\omega t)} + S_r e^{i(\mathbf{k}_{rs}\cdot\mathbf{x}-\omega t)} \tag{2.10b}$$

where $P(S)_{i(r)}$ denotes the amplitude of the incident (reflected) longitudinal (shear) wave.

By using the traction-free boundary condition ($\sigma_{zz}\big|_{z=0} = 0,\ \sigma_{zx}\big|_{z=0} = 0$), we can get some interesting properties of reflection. The reflection phenomena for each longitudinal or shear wave incidence is shown in Fig. 2.2. In this section, we will only focus on the longitudinal wave incidence. In this way, we can concentrate on the reflection phenomena.

When the longitudinal wave incidents to the traction-free boundary, both longitudinal and shear wave reflected from the boundary. This phenomenon is interesting because such reflection doesn't happen on the acoustic wave reflection. The longitudinal wave is reflected in the same angle with the incident longitudinal wave. The shear wave is reflected in the different angle and this certain angle can be calculated from the Snell's law of reflection. This property stems from the difference between two types of elastic waves. These two properties can be written as:

$$\alpha_i = \alpha_r \,, \tag{2.11}$$

$$\frac{\sin\alpha_r}{\sin\beta_r} = \frac{k_s}{k_p} = \frac{c_p}{c_s} > 1 \,, \tag{2.12}$$

where $k_{p(s)}$ and $c_{p(s)}$ denote the wavenumber and speed of the longitudinal (shear) wave.

We can also get the amplitude ratio of incident and reflected waves as follows:

$$\frac{P_r}{P_i} = \frac{\sin(2\alpha)\sin(2\beta) - (c_p / c_s)^2 \cos^2(2\beta)}{\sin(2\alpha)\sin(2\beta) + (c_p / c_s)^2 \cos^2(2\beta)} \,, \tag{2.13a}$$

$$\frac{P_r}{P_i} = \frac{-2\sin(2\alpha)\cos(2\beta)}{\sin(2\alpha)\sin(2\beta) + (c_p / c_s)^2 \cos^2(2\beta)} \,. \tag{2.13b}$$

2.3 Diffraction grating theory

A diffraction grating comes from the optics. Devices such as spectrographs are using the diffraction grating structure to divide or disperse the light by a number of different wavelengths. Usually, these devices have periodic structures. By controlling the spacing of the grating or the wavelength of the light, the propagating direction of beam differs. Usually the spacing (or the periodicity) of the diffraction grating is larger than wavelength of the light. If it is not greater than the wavelength, diffraction pattern does not arise and only direct reflection or refraction of the light according to the Snell's law exists. In addition, either transmission or reflection type

diffraction grating is possible. In this section, we will derive the grating equation in 1D periodic geometry. Such grating equation which is derived with the light propagation can also be used in diffraction grating structures in any wave fields such as electromagnetic, acoustic, elastic wave, etc.

2.3.1 Grating equation in 1D periodic geometry

In optics, the simplest type of diffraction grating structure is the evenly spaced periodic slit structures in the *y*-direction as in Fig. 2.3. For the periodicity, the number of structure should be large. When the incident monochromatic light of certain wavelength λ enters the periodic slit structures, the light reflected or refracted from the structures in specific direction. We will derive the grating equation in terms of refractive problem as in Fig. 2.3. The reflection problem can also be derived in the same method.

When the monochromatic light normally incidents into the periodic slit structure, the waves in the adjacent slits diffract and interfere with each other. The path difference between these refractive waves in the adjacent slits can be calculated as:

$$d \sin \theta_r^n = n\lambda, \ \ (n = 0, \ \pm 1, \ \pm 2, ...) \tag{2.14}$$

where d is the periodicity or the spacing of the diffraction grating, λ is the wavelength of the incident monochromatic light, θ_r^n is the refractive angle of the *n*-th diffraction mode of the light, and n is the diffraction mode number, which is the integer number. The 0th diffraction mode ($n = 0$) is the ordinary refraction

direction, which, in this problem, is the normal direction ($\theta_r^0 = 0^\circ$). The equation written in Eq. (2.14) is known as the grating equation in 1D periodic geometry for the normal incident monochromatic wave according to the diffraction grating theory. We can generalize the Eq. (2.14) by introducing the incident angle θ_i . The grating equation in 1D periodic geometry for the oblique incident monochromatic wave can be written as follows:

$$d(\sin\theta_r^n - \sin\theta_i) = n\lambda, \quad (n = 0, \pm 1, \pm 2, ...) \tag{2.15a}$$

or

$$\sin\theta_r^n = \sin\theta_i + \frac{n\lambda}{d}. \quad (n = 0, \pm 1, \pm 2, ...) \tag{2.15b}$$

From Eq. (2.14) and Eq. (2.15), we can easily find all of the refractive angle of the diffraction modes.

The phenomenon of diffraction grating can be physically interpreted from the diffraction grating equations. In Eq. (2.14) or Eq. (2.15), the path difference between the adjacent slits are calculated from the left-hand side of the equation. When the path difference equals with the integer multiple of the wavelength, then the constructive interference occurs. Due to the periodicity which can be thought to be a infinite array of periodic structures, such constructive interferences strengthen and the diffraction modes appear strongly in the certain directions.

The grating equations in Eq. (2.14) and Eq. (2.15) are identical with the path difference equation in the double slits. In Young's double slit experiment, same explanation using the path difference of the diffracted waves takes place. However,

the performance of the dividing the wave separately differs. Since the diffraction gratings consist of periodic structures, constructive interferences in the direction of diffraction modes strengthen. Therefore, the diffraction mode is well distinguished in the diffraction gratings. We can see that the wave amplitudes are highly increased at the diffraction modes. But, in the angle which is slightly different from the diffraction mode, the wave amplitude decreased abruptly.

On the other hand, the double slits are less distinguished between the constructive and destructive interference position. We can see that the wave amplitudes are also highly increased at the certain positions because of the constructive interferences. However, wave amplitudes decreased gradually to the positions of the destructive interferences. In this reason, the spectrographs are widely using the diffraction gratings.

In our dissertation, such the grating equation (Eq. (2.14) and Eq. (2.15)) are utilized to design the structures. With these grating equations, we can easily calculate the reflection or refraction angle of the periodic structures. In addition, we can calculate the wave vector from these grating equations.

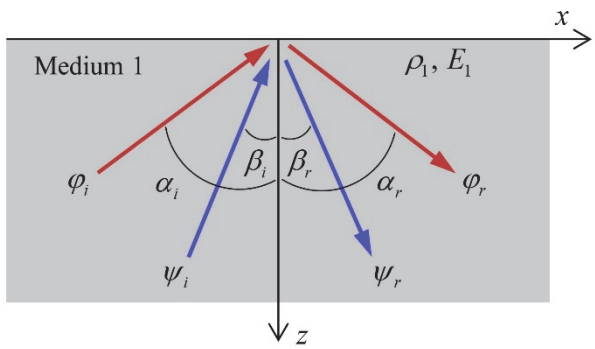

Fig. 2.1 General case of reflection problem in a traction-free boundary.

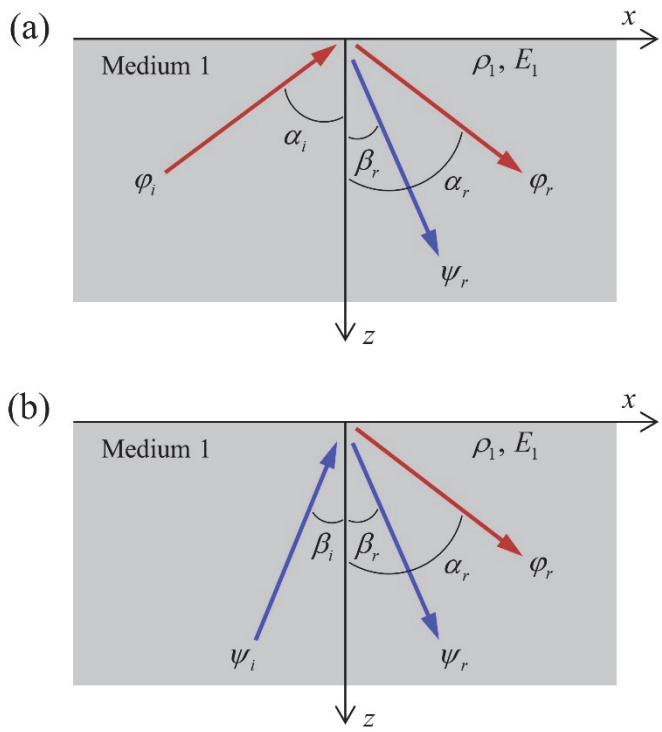

Fig. 2.2 Two incident case of reflection problem in a traction-free boundary. (a) Longitudinal wave incidence, (b) Shear vertical wave incidence.

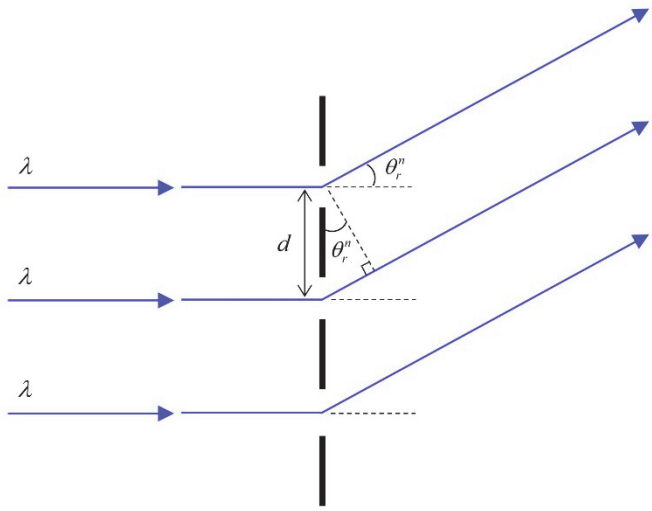

Fig. 2.3 The periodic slit structure operated as diffraction grating in 1D periodic geometry. The refration of the monochromatic wave in the normal incidence case is presented.

CHAPTER 3.

Elastic Metagratings for Longitudinal Wave Steering

The contents covered in this chapter were published through the journal paper [61].

3.1 Chapter overview

Recently, extraordinary wave manipulation based on the concept of metamaterials has become a very popular topic in wave-related research fields. Among them, metasurfaces that are artificially engineered, subwavelength-scaled structural layers have been extensively investigated to realize anomalous wave steering due to their spatial compactness and theoretical clarity [8-11,63,64]. It is interesting that the introduction of a phase shift along an interface between dissimilar media has been the key strategy in most of the existing studies on metasurfaces to realize various phenomena, such as reflection [65-67], refraction [26-29,68-75], retroreflection [76-79], beam focusing and self-accelerating [80-84], helical wave-front generators [85], asymmetric transmission [86-88], holograms [89,90], and cloaking [91-94]. Governed by the generalized law of wave reflection and refraction, i.e., the generalized Snell's law [25], the phase gradient over a unit cell required for

reflecting or refracting an incident wave at a specific target angle can be determined. However, it has been observed that the phase gradient-type metasurfaces may suffer from poor efficiency, especially due to undesignated wave propagations in spurious directions [30]. Basically, this phenomenon is due to the existence of multiple modes composing the scattered waves. In other words, the phase gradient-type metasurfaces enable to specify one propagating mode in a target direction but they cannot control other propagating modes.

Alternatively, the diffraction grating theory [31,32] has been employed to realize anomalous wave reflection/refraction in the fields of electromagnetic [30,33-36] and acoustic waves [37-57]. When the scatterers in the periodic gratings have specific properties, it is possible to cancel out some diffraction modes. Recently, the diffraction theory has been coupled with the concept of metamaterials. So-called metagratings consist of periodic gratings constructed with various kinds of scatterers, for example, printed circuit board scatterers [33,34,95], bianisotropic [30,44,46,96] and bipartite particles [97] for anomalous wavefront modulation. In metagratings, the main issue is how to find appropriate configurations of the scatterers effectively and systematically in the periodic gratings that acquire such a controllability for wave steering.

Recently, a few studies on metagratings reported that the diffraction modes are manageable by solving a kind of inverse problems that are formulated to search for appropriate geometric parameters of the scatterers in acoustic [37,40,41] and elastic wave fields [58]. Such handlings of the diffraction modes require that the amplitudes

of every scattered mode from the periodic gratings are specified. Once the amplitudes of targeting scattered modes are set to take specific values, inverse problems are solved to find the corresponding geometric parameters. It is noteworthy to mention that analytical approaches with simple configurations may be helpful to model scatterers suitable for metagratings because analytical descriptions would provide more stable and efficient calculation of the amplitudes for a large number of scattered modes. For example, quarter-wavelength resonators frequently used for sound absorption at a narrow band frequency were employed to model scatterers of acoustic metagratings for anomalous steering [37]. To eliminate undesignated diffraction modes in [37], inverse problems were solved to find appropriate geometrical parameters of the resonators, such as the length of individual resonators as well as the distance between neighboring ones. Quarter-wavelength resonators were also applied for acoustic wave cloak [40] and beam splitter [41] applications. In an elastic medium, point scatterers modelled by mass-spring resonators were used to control flexural waves [58]. However, no elastic metagratings realizing anomalous reflections of longitudinal elastic waves with the undesignated diffraction modes eliminated have been proposed.

In this chapter, the main problem of simultaneous wave steering and mode conversion is simplified into controlling only the longitudinal wave without considering the shear wave. We propose novel elastic metagratings composed of slender and straight beam-type members for anomalous reflections of longitudinal elastic waves. As far as the authors are aware, this work is the first contribution to

manipulate elastic longitudinal waves with metagratings. As shown in Fig. 3.1, the present elastic metagratings are constructed with a repeated attachment of unit cells, each of which consists of discrete, single or multiple beam-type members on a traction-free boundary of a thin elastic plate. The geometric parameters of the beam-type members as in Fig. 3.2 will be searched to realize the desired anomalous reflections and beam splittings for normally incident longitudinal waves on the metagratings. Here, the beam-type members are named as they have longitudinal and flexural motions as described in Fig. 3.3(a). This implies that the simply configured beam-type members can effectively control the longitudinal and shear waves along the members as well as in the elastic continuum plate, efficiently managing the diffraction modes. Note that the out-of-plane motions of the elastic continuum plate and the beam-type members are not considered in the present work.

To couple the wave field in the beam-type members with that in the elastic continuum plate, we establish analytical coupling conditions between them. The longitudinal and shear wave fields in the elastic plate are fully derived using the diffraction grating theory. On the other hand, the wave fields inside the beam-type scatterers are predicted by a combination of the bar theory and the Euler-Bernoulli beam theory. Then, the wave fields in the elastic plate and beam-type scatterers are coupled along their interfaces to satisfy the displacement continuities and force equilibrium. For grating scattered modes as designated, their wave potential amplitudes should be specified. The geometric parameters of the beam-type scatterers are found by solving inverse problems in which the wave potential amplitudes of the undesired scattered

modes are to be minimized. A gradient-based optimization algorithm is used for solving the inverse problem efficiently. As specific applications, the proposed metagratings are used to realize anomalous reflections and beam splitting for incident longitudinal waves. The physical significance of the designed metagratings is interpreted and some experiments were also performed to verify the designed metagratings.

The present elastic metagratings are expected to be applied for non-destructive structural health monitoring and medical imaging. As in recent works related to the elastic metamaterials [17,19,98], the present elastic metagratings can be used for elaborate elastic wave manipulation, such as the realization of reflection-wave controlled or nonreflective free boundaries of elastic plates.

3.2 Analytical modeling of the elastic wave motion

Fig. 3.1 briefly shows a schematic configuration of the present elastic metagratings with the illustration of in-plane incident and scattered longitudinal waves in an elastic plate. The unit cell of the elastic metagratings is defined in Ω_2 of Fig. 3.2 and composed of discrete beam-type members, which can carry longitudinal and flexural motions in the x-y plane. Incident longitudinal waves impinge on the plate in normal or oblique directions and scattered waves from the metagratings are composed of several modes as illustrated in Fig. 3.1. These scattered waves are composed of the main regularly reflected zeroth-order mode and irregularly reflected higher-order modes. According to the diffraction theory, the directions of the scattered longitudinal waves are determined when the length of the unit cell and the angle of the incident longitudinal wave is given. In this section, wave motions in an elastic plate and a discrete beam-type member are described using the diffraction theory and the bar-beam theory, respectively.

3.2.1 Wave motion in an elastic plate

In order to describe wave motion in a thin elastic continuum plate occupying Ω_1 in Fig. 3.2, we first introduce the grating equation of elastic waves using the diffraction theory [31,32,99]. Since there are two types of waves in the elastic medium, two grating equations, each of which belongs to longitudinal and shear waves, respectively, are considered as:

$$k_{py}^{n} = k_p \sin\theta_{p.ref}^{n} = k_p \sin\theta_{p.inc} + \frac{2\pi n}{a} \quad , \tag{3.1a}$$

$$k_{sy}^{n} = k_s \sin\theta_{s.ref}^{n} = k_s \sin\theta_{s.inc} + \frac{2\pi n}{a} \quad , \tag{3.1b}$$

where symbols k and θ denote the wave number and the angle of wave propagation. Subscripts p and s indicate the quantities of the longitudinal and shear waves, respectively. The number of the scattered modes is denoted by *n*. Therefore, $n = 0$ represents the zeroth mode. Additional subscripts y (or x) on k indicate the $y-$(or $x-$)directional component of the wave number, and additional subscripts inc and ref are used to indicate the angle of incident and reflected waves, respectively. The periodicity of unit cell is denoted by a, as illustrated in Fig. 3.2.

Grating equations in an elastic continuum medium can be simplified using the generalized Snell's law of the regularly reflected waves [4]:

$$k_p \sin\theta_{p.inc} = k_p \sin\theta_{p.ref}^{0} = k_s \sin\theta_{s.inc} = k_s \sin\theta_{s.ref}^{0} \quad , \tag{3.2}$$

$$k_{py}^{n} = k_{sy}^{n} \triangleq k_{y}^{n} \quad . \tag{3.3}$$

For a later use, the $x-$ components of the wave number k for the *n*th-order longitudinal and shear waves are given by the dispersion relation, respectively, as:

$$\left(k_{px}^{n}\right)^2 = k_p^2 - \left(k_{py}^{n}\right)^2 , \quad \left(k_{sx}^{n}\right)^2 = k_s^2 - \left(k_{sy}^{n}\right)^2 \quad , \tag{3.4a,b}$$

According to the classical theory on elastic waves [4], the wave equation of longitudinal and shear waves can be written in terms of the corresponding potential fields φ and ψ, respectively, in the elastic domain Ω_1 under plane-stress condition:

$$\nabla^2\varphi = \frac{1}{c_p^2}\frac{\partial^2\varphi}{\partial T^2} \quad , \quad \nabla^2\psi = \frac{1}{c_s^2}\frac{\partial^2\psi}{\partial T^2} \quad , \tag{3.5a,b}$$

where symbols c_p and c_s denote the propagation velocities of the longitudinal and shear waves, respectively, and T is time.

In writing solutions to Eqs. (3.5a) and (3.5b), Eqs. (3.3) and (3.4) are used:

$$\begin{aligned}\varphi^{Total} &= e^{-j(k_{px}^0 x + k_y^0 y)} + \sum_{n=-N}^{N}\left[\left(P_n e^{jk_{px}^n x}\right)e^{-jk_y^n y}\right] \\ &= \sum_{n=-N}^{N}\left[\left(\delta_{n0}e^{-jk_{px}^n x} + P_n e^{jk_{px}^n x}\right)e^{-jk_y^n y}\right]\end{aligned} \quad , \tag{3.6a}$$

$$\psi^{Total} = \sum_{n=-N}^{N}\left[\left(S_n e^{jk_{sx}^n x}\right)e^{-jk_y^n y}\right] \quad , \tag{3.6b}$$

where φ^{Total} and ψ^{Total} represent the spatial variations of the φ and ψ under the time-harmonic motion ($e^{j\omega T}$ with the angular frequency ω and $j=\sqrt{-1}$). In Eqs. (3.6a,b), coefficients P_n and S_n denote the amplitudes of the *n*th-order potentials of the longitudinal and shear waves, respectively, and N indicates the limit number of the used modes. The unit amplitude of the potential corresponding

to the incident longitudinal wave is denoted by the Kronecker delta δ_{n0}. Although the scattered modes have to be infinitely summed in Eq. (3.6a) and Eq. (3.6b), a total of 141 modes ($N = 70$) are used in this work as the selected N value appears to be sufficient to express the solution field in the present consideration. Among N modes, only a few modes represent propagating waves along the x axis and the remaining modes represent non-propagating waves.

Two-dimensional displacement (u_x, u_y) and stress components (σ_{ij}, $i, j = 1, 2$) of the elastic continuum plate in the domain Ω_1 shown in Fig. 3.2 can be written in terms of the scalar wave potentials as [4]:

$$u_x^{(1)} = \frac{\partial \varphi}{\partial x} + \frac{\partial \psi}{\partial y}, \quad u_y^{(1)} = \frac{\partial \varphi}{\partial y} - \frac{\partial \psi}{\partial x} \quad , \tag{3.7a,b}$$

$$\sigma_{ij}^{(1)} = \lambda e^{(1)} \delta_{ij} + 2\mu \varepsilon_{ij}^{(1)} \quad , \tag{3.8}$$

where superscript (1) denotes the quantities defined in Ω_1 and e and ε_{ij} stand for the dilatation ($\nabla \cdot \boldsymbol{u}$) and the strain components. Symbols λ and μ are the Lame constant and shear modulus in the elastic plate, respectively. As time-harmonic waves are assumed throughout this study, the explicit dependence of u_x, u_y and σ_{ij} on $e^{j\omega T}$ will be omitted in the subsequent discussion.

By substituting Eqs. (3.6a) and (3.6b) into Eqs. (3.7a), (3.7b) and (3.8), the explicit

expressions of the displacement and stress fields are obtained as:

$$u_x^{(1)}(x,y)=\sum_{n=-N}^{N}\left[-jk_{px}^{n}\left(\delta_{n0}e^{-jk_{px}^{n}x}-P_n e^{jk_{px}^{n}x}\right)-jk_y^n\left(S_n e^{jk_{sx}^{n}x}\right)\right]e^{-jk_y^n y}\ , \quad (3.9a)$$

$$u_y^{(1)}(x,y)=\sum_{n=-N}^{N}\left[-jk_{y}^{n}\left(\delta_{n0}e^{-jk_{px}^{n}x}+P_n e^{jk_{px}^{n}x}\right)-jk_{sx}^n\left(S_n e^{jk_{sx}^{n}x}\right)\right]e^{-jk_y^n y}\ , \quad (3.9b)$$

$$\begin{aligned}&\sigma_{xx}^{(1)}(x,y)\\&=\sum_{n=-N}^{N}\left[\left(-\lambda k_p^2-2\mu k_{px}^{n\,2}\right)\left(\delta_{n0}e^{-jk_{px}^{n}x}+P_n e^{jk_{px}^{n}x}\right)+2\mu k_y^n k_{sx}^n\left(S_n e^{jk_{sx}^{n}x}\right)\right]e^{-jk_y^n y}\ ,\end{aligned} \quad (3.10a)$$

$$\begin{aligned}&\sigma_{xy}^{(1)}(x,y)\\&=\sum_{n=-N}^{N}\left[-2\mu k_{px}^n k_y^n\left(\delta_{n0}e^{-jk_{px}^{n}x}-P_n e^{jk_{px}^{n}x}\right)+\left(-\mu k_s^2+2\mu k_{sx}^{n\,2}\right)\left(S_n e^{jk_{sx}^{n}x}\right)\right]e^{-jk_y^n y}\end{aligned}\ . \quad (3.10b)$$

The results given in Eqs. (3.9) and (3.10) will be used to establish the interface coupling of the wave fields with Ω_2.

3.2.2 Modeling of the beam-type member

As shown in Fig. 3.2, the present elastic metagratings are constructed with a periodic attachment of unit cells, each of which consists of slender and straight beam-type members in domain Ω_2. We will analyze wave phenomena of the beam-type members using the bar theory for their longitudinal motions and the Euler-Bernoulli beam theory for their flexural motions [100,101]. Using these theories, we can describe the displacement and slope fields of the *i* th beam-type member located by

b_i in the domain Ω_2 as follows:

$$u_y^{(2)}\left(x;\, b_i\right) = A_i e^{-jkx} + B_i e^{-kx} + C_i e^{jkx} + D_i e^{kx}\,, \tag{3.11a}$$

$$\Phi^{(2)}\left(x;\, b_i\right) = -jkA_i e^{-jkx} - kB_i e^{-kx} + jkC_i e^{jkx} + kD_i e^{kx}\,, \tag{3.11b}$$

$$u_x^{(2)}\left(x, y;\, b_i\right) \triangleq u_{x.bar}^{(2)} + u_{x.beam}^{(2)} = \left(F_i e^{-jk_b x} + G_i e^{jk_b x}\right) - \left(y - b_i\right)\Phi^{(2)}\left(x\right), \tag{3.11c}$$

where $u_y^{(2)}$ and $\Phi^{(2)}$ denote the *y*-directional displacement and the slope of the neutral axis of the beam-type member, respectively. The wave number k in Eqs. (3.11a,b) is related to $k = \left(\rho S / EI\right)^{1/4}\sqrt{\omega}$ for the Euler-Bernoulli beam theory where ρ, S, and EI denote the density, cross-sectional area, and bending rigidity of the beam-type member. On the other hand, $u_x^{(2)}$ is the *x*-directional displacement of the beam-type member, which is composed of the longitudinal displacements contributed by the bar theory and the Euler-Bernoulli beam theory together.

In Eq. (3.11c), symbol k_b stands for the wave number in the bar ($k_b = \omega\sqrt{\rho / E}$, with Young's modulus E). In Eqs. (3.11a-c), the amplitudes of propagating or evanescent flexural waves and propagating longitudinal waves are denoted as the coefficients A_i to G_i. Note that the coordinates x and y in Eqs. (3.11a-c) are measured from the corner of the unit cell as shown in Figs. 3.1, 3.2, and 3.3.

By imposing the traction-free condition at the free end of the beam-type member

(i.e., at $x = L_i$), one can derive the relations among $A_i \sim G_i$:

$$G_i = F_i e^{-2jk_b L_i} \quad , \tag{3.12}$$

$$C_i = -jA_i e^{-2jkL_i} + (1+j) B_i e^{-(1+j)kL_i} \quad , \tag{3.13a}$$

$$D_i = (1-j) A_i e^{-(1+j)kL_i} + jB_i e^{-2kL_i} \quad . \tag{3.13b}$$

Substituting Eqs. (3.12) and (3.13a-b) into Eqs. (3.11a-c) yields:

$$\begin{aligned} u_y^{(2)}(x;\, b_i) = {} & A_i \left[e^{-jkx} - je^{jkx-2jkL_i} + (1-j) e^{kx-(1+j)kL_i} \right] \\ & + B_i \left[e^{-kx} + (1+j) e^{jkx-(1+j)kL_i} + je^{kx-2kL_i} \right] , \end{aligned} \tag{3.14a}$$

$$\begin{aligned} \Phi^{(2)}(x;\, b_i) = {} & A_i \left[-jke^{-jkx} + ke^{jkx-2jkL_i} + (1-j) ke^{kx-(1+j)kL_i} \right] \\ & + B_i \left[-ke^{-kx} - (1-j) ke^{jkx-(1+j)kL_i} + jke^{kx-2kL_i} \right] , \end{aligned} \tag{3.14b}$$

$$\begin{aligned} & u_x^{(2)}(x, y;\, b_i) \\ & = -(y - b_i) \Big[A_i \left\{ -jke^{-jkx} + ke^{jkx-2jkL_i} + (1-j) ke^{kx-(1+j)kL_i} \right\} \\ & + B_i \left\{ -ke^{-kx} - (1-j) ke^{jkx-(1+j)kL_i} + jke^{kx-2kL_i} \right\} \Big] + F_i \left(e^{-jk_b x} + e^{jk_b x - 2jk_b L_i} \right) . \end{aligned} \tag{3.14c}$$

Using Eqs. (3.14a-c), the stress components in the beam-type member can be found as:

$$\begin{aligned} & \sigma_{xx}^{(2)}(x, y;\, b_i) \\ & = \sigma_{xx.beam}^{(2)} + \sigma_{xx.bar}^{(2)} \\ & = -E(y - b_i) \Big[A_i \left\{ -k^2 e^{-jkx} + jk^2 e^{jkx-2jkL_i} + (1-j) k^2 e^{kx-(1+j)kL_i} \right\} \\ & + B_i \left\{ k^2 e^{-kx} - (1+j) k^2 e^{jkx-(1+j)kL_i} + jk^2 e^{kx-2kL_i} \right\} \Big] - jEk_b F_i \left(e^{-jk_b x} - e^{jk_b x - 2jk_b L_i} \right) , \end{aligned} \tag{3.15a}$$

$$
\begin{aligned}
&\sigma_{xy}^{(2)}\left(x, y;\, b_i\right) \\
&= \frac{1}{t}\int_S \frac{\partial \sigma_{xx}^{(2)}}{\partial x} dS = \frac{V\left(x;\, b_i\right) Q\left(y;\, b_i\right)}{t\, I} \\
&= -\frac{E}{2}\left\{\left(\frac{w}{2}\right)^2 - (y-b_i)^2\right\}\left[A_i\left\{jk^3 e^{-jkx} - k^3 e^{jkx-2jkL_i} + (1-j)k^3 e^{kx-(1+j)kL_i}\right\}\right. \\
&\left. + B_i\left\{-k^3 e^{-kx} + (1-j)k^3 e^{jkx-(1+j)kL_i} + jk^3 e^{kx-2kL_i}\right\}\right],
\end{aligned}
\tag{3.15b}
$$

where t and w are the beam thickness and the beam width, respectively. The quantities $V\left(x;\, b_i\right)$ and $Q\left(y;\, b_i\right)$ denote the shear force and the first moment of the cross section S of the *i*th beam-type member, respectively.

3.2.3 Interface coupling conditions

To establish the interface coupling conditions between Ω_1 and Ω_2, we consider a simple case in which Ω_2 involves only one beam-type member, as shown in Fig. 3.3(b). As the first interface condition, we must consider continuity in the displacement field at $x=0$. Because the displacements in Ω_2 are fully characterized by the one-dimensional bar and beam theories, the displacements in Ω_1 are matched to the displacements in Ω_2 at the interface in an averaged sense as:

$$
\frac{1}{S}\int_S u_x^{(1)}\big|_{x=0}\, dS = u_x^{(2)}\left(x=0, y=b_i;\, b_i\right), \tag{3.16a}
$$

$$\frac{1}{S}\int_S u_y^{(1)}\big|_{x=0}\, dS = u_y^{(2)}\left(x=0;\, b_i\right). \tag{3.16b}$$

Likewise, the stress continuities at the interface shown in Fig. 3.3(b) are replaced by force and moment equilibrium conditions. Since the stresses in Ω_2 are only defined in the range of $b_i - w/2 < y < b_i + w/2$, it is required to express those stresses in a wider range $0 \le y \le a$ as:

for $b_i - w/2 < y < b_i + w/2$:

$$\begin{aligned}
&\sigma_{xx}^{(2)}\left(x, y;\, b_i\right) \\
&= -E\left(y - b_i\right)\Big[A_i \left\{ -k^2 e^{-jkx} + jk^2 e^{jkx - 2jkL_i} + \left(1-j\right)k^2 e^{kx-(1+j)kL_i} \right\} \\
&+ B_i \left\{ k^2 e^{-kx} - \left(1+j\right)k^2 e^{jkx-(1+j)kL_i} + jk^2 e^{kx-2kL_i} \right\} \Big] - jEk_b F_i \left(e^{-jk_b x} - e^{jk_b x - 2jk_b L_i} \right),
\end{aligned} \tag{3.17a}$$

$$\begin{aligned}
&\sigma_{xy}^{(2)}\left(x, y;\, b_i\right) \\
&= -\frac{E}{2}\left\{ \left(\frac{w}{2}\right)^2 - (y-b_i)^2 \right\} \Big[A_i \left\{ jk^3 e^{-jkx} - k^3 e^{jkx-2jkL_i} + (1-j)k^3 e^{kx-(1+j)kL_i} \right\} \\
&+ B_i \left\{ -k^3 e^{-kx} + (1-j)k^3 e^{jkx-(1+j)kL_i} + jk^3 e^{kx-2kL_i} \right\} \Big],
\end{aligned} \tag{3.17b}$$

for $0 \le y \le b_i - w/2$ or $b_i + w/2 \le y \le a$:

$$\sigma_{xx}^{(2)}\left(x=0, y;\, b_i\right) = 0, \tag{3.17c}$$

$$\sigma_{xy}^{(2)}\left(x=0, y;\, b_i\right) = 0. \tag{3.17d}$$

Imposing the stress continuity along the interface between Ω_1 and Ω_2, we can get the force equilibrium equations as:

$$\int_0^a (\sigma_{xx}^{(1)} - \sigma_{xx}^{(2)})\big|_{x=0}\, dy = 0, \tag{3.18a}$$

$$\int_0^a (\sigma_{xy}^{(1)} - \sigma_{xy}^{(2)})\big|_{x=0}\, dy = 0. \tag{3.18b}$$

In addition, the moment equilibrium in the range of $b_i - w/2 < y < b_i + w/2$ can be obtained as:

$$\int_S \sigma_{xx}^{(1)}\big|_{x=0} \left(y - b_i\right) dS - M_b^{(2)}\left(x=0;\, b_i\right) = 0, \tag{3.19}$$

where $M_b^{(2)}(x=0;\ b_i)$ is the bending moment of the beam-type member at the interface.

Using the results in sections 3.2.1 and 3.2.2, Eqs. (3.16a,b) and (3.19) can be expressed as follows, respectively:

$$\sum_{n=-N}^{N}\left[\left\{-jk_{px}^n\left(\delta_{n0} - P_n\right) - jk_y^n S_n\right\}\left(\frac{1}{S}\int_{b_i-\frac{w}{2}}^{b_i+\frac{w}{2}} e^{-jk_y^n y} dy\right)\right] = F_i\left(1 + e^{-2jk_b L_i}\right), \tag{3.20a}$$

$$\begin{aligned}&\sum_{n=-N}^{N}\left[\left\{-jk_y^n\left(\delta_{n0} + P_n\right) - jk_{sx}^n S_n\right\}\left(\frac{1}{S}\int_{b_i-\frac{w}{2}}^{b_i+\frac{w}{2}} e^{-jk_y^n y} dy\right)\right] \\ &= A_i\left\{1 - je^{-2jkL_i} + \left(1-j\right)e^{-(1+j)kL_i}\right\} + B_i\left\{1 + \left(1+j\right)e^{-(1+j)kL_i} + je^{-2kL_i}\right\},\end{aligned} \tag{3.20b}$$

$$\begin{aligned}&\sum_{n=-N}^{N}\left[\left\{\left(-\lambda k_p^2 - 2\mu k_{px}^{n\,2}\right)\left(\delta_{n0} + P_n\right) + 2\mu k_y^n k_{sx}^n S_n\right\}\left(\frac{1}{EI}\int_{b_i-\frac{w}{2}}^{b_i+\frac{w}{2}}\left(y - b_i\right)e^{-jk_y^n y} dy\right)\right] \\ &= A_i\left\{-k^2 + jk^2 e^{-2jkL_i} + \left(1-j\right)k^2 e^{-(1+j)kL_i}\right\} \\ &+ B_i\left\{k^2 - \left(1+j\right)k^2 e^{-(1+j)kL_i} + jk^2 e^{-2kL_i}\right\}.\end{aligned} \tag{3.20c}$$

If the total number of the beam-type members in each unit cell is set to be N_B, then

the total number of equations in Eqs. (3.20a-c) becomes $3N_B$.

Eqs. (3.18a) and (3.18b) can be individually separated into $(2N+1)$ equations using the property of orthogonality.

$$\begin{aligned}
&\left[\left(-\lambda k_p^2 - 2\mu k_{px}^{n\,2}\right)\left(\delta_{n0} + P_n\right) + 2\mu k_y^n k_{sx}^n S_n\right] a \\
&= \sum_{i=1}^{N_B}\Bigg[-E\Big\{A_i\left(-k^2 + jk^2 e^{-2jkL_i} + (1-j)k^2 e^{-(1+j)kL_i}\right) \\
&+B_i\left(k^2 - (1+j)k^2 e^{-(1+j)kL_i} + jk^2 e^{-2kL_i}\right)\Big\}\left(\int_{b_i-\frac{w}{2}}^{b_i+\frac{w}{2}} (y-b_i) e^{jk_y^n y} dy\right) \\
&-jEk_b F_i\left(1 - e^{-2jk_b L_i}\right)\left(\int_{b_i-\frac{w}{2}}^{b_i+\frac{w}{2}} e^{jk_y^n y} dy\right)\Bigg],
\end{aligned} \tag{3.21a}$$

$$\begin{aligned}
&\left[-2\mu k_{px}^n k_y^n\left(\delta_{n0} - P_n\right) - \left(\mu k_s^2 - 2\mu k_{sx}^{n\,2}\right) S_n\right] a \\
&= \sum_{i=1}^{N_B}\Bigg[-\frac{E}{2}\Big\{A_i\left(jk^3 - k^3 e^{-2jkL_i} + (1-j)k^3 e^{-(1+j)kL_i}\right) \\
&+B_i\left(-k^3 + (1-j)k^3 e^{-(1+j)kL_i} + jk^3 e^{-2kL_i}\right)\Big\}\left(\int_{b_i-\frac{w}{2}}^{b_i+\frac{w}{2}} \left(\left(\frac{w}{2}\right)^2 - (y-b_i)^2\right) e^{jk_y^n y} dy\right)\Bigg].
\end{aligned} \tag{3.21b}$$

From Eqs. (3.20) and (3.21), one can form a full matrix equation of linear system consisting of $(4N+3N_B+2)$ equations with respect to the same number of variables (P_n, S_n, A_i, B_i, F_i). Once we obtain scattered wave amplitudes (P_n, S_n), we can analyze the whole longitudinal wave scattered field created by the metagrating.

3.3 Design of beam-type elastic metagratings

In order to reflect the incident longitudinal wave at a specific angle, the lattice constant or periodicity of metagratings has to be determined using the generalized Snell's law of reflection. Among multiple scattered modes, the first-order mode is required to propagate at a designated angle while the other unwanted modes are to be suppressed by using an elastic metagrating. The grating equations for the 1st-order scattered mode for the longitudinal wave are obtained from Eq. (3.1a) by substituting $n=+1$ and $n=-1$, respectively:

for $n=+1$:
$$k_p \sin\theta_{p.ref}^{+1} = k_{py}^{+1} = k_p \sin\theta_{p.inc} + \frac{2\pi}{a}, \tag{3.22a}$$

for $n=-1$:
$$k_p \sin\theta_{p.ref}^{-1} = k_{py}^{-1} = k_p \sin\theta_{p.inc} - \frac{2\pi}{a}. \tag{3.22b}$$

From Eqs. (3.22a) and (3.22b), the unit cell length a to steer the incident longitudinal wave is calculated for each value of $n=\pm 1$, respectively, as:

$$a = \frac{2\pi}{k_p\left(\sin\theta_{p.ref}^{+1} - \sin\theta_{p.inc}\right)}, \tag{3.23a}$$

$$a = \frac{2\pi}{k_p\left(\sin\theta_{p.inc} - \sin\theta_{p.ref}^{-1}\right)}. \tag{3.23b}$$

The unit cell length for a normally incident longitudinal wave ($\theta_{p.inc}=0$) is determined from Eq. (3.23a), while Eq. (3.23b) is used for an obliquely incident longitudinal wave.

To realize anomalous steering of longitudinal waves, we begin with a metagrating consisting of only one or two beam-type members. After investigating how effective the metagrating is for anomalous wave steering, we will consider a metagrating consisting of up to six beam-type members. Numerical simulations will show that the problems considered in this work can be fully handled using a metagrating consisting of six beam-type members.

A 1 mm-thick aluminum alloy (A6061) plate is used to make the elastic continuum plate and the beam-type members. The target frequency is set to be 60 kHz for all metagratings in this work. The corresponding longitudinal wave number and wavelength are $k_p = 69.89\ \mathrm{m}^{-1}$ and $\lambda_p = 0.0899\ \mathrm{m}$, respectively. The length (L_i) of the ith beam-type member ($i = 1, \ldots, N_B$) is treated as a design variable of the present elastic metagratings. In the case when multiple beam-type members are used, the distance between two adjacent members can be also considered as a design variable. The appropriate lengths of the beam-type members are determined by inverse problems solved by a gradient-based optimization algorithm [102]. The phenomena of anomalous wave reflection using the designed metagratings were investigated using a finite-sized model and an infinitely periodic model using COMSOL Multiphysics®.

It should be noted that the displacements at the interfacial edges between the domains Ω_1 and Ω_2 tend to be much larger compared to those in other regions when the

beam-type members experience longitudinal vibrational resonances. To account for such local motions near the resonances, we introduce the effective width w' and length L' by adopting end-effect correction factors in the *x*- and *y*-direction of the beam-type members as follow [26]:

$$w' = \left(1+\beta_1\right) w, \quad L' = \left(1+\beta_2\right) L . \tag{3.24a,b}$$

The correction factors β_1 and β_2 should be adjusted empirically, because they would depend on problems in consideration. In this work, β_1 and β_2 are evaluated by comparing the values of the numerically calculated divergence field ($\nabla \cdot \boldsymbol{u}$) with the analytical ones. The actual values and more explanations can be found in following examples.

3.4 Design examples

As the first example, we consider a metagrating having only one beam-type member in order to realize retroreflection of an oblique incidence of the longitudinal wave. As illustrated in Fig. 3.4(a), the longitudinal wave impinges on the free boundary of the plate ($x = 0$) at an angle of $\theta_{p.inc} = 60^\circ$ and it is supposed to be reflected by a metagrating at a target angle of $\theta_{p.ref} = -60^\circ$. The width of the beam-type member is set to be $w = 3\,\text{mm}$ and the length of the unit cell is determined to be $a = 0.0519\,\text{m}$ by Eq. (3.23b). According to Eq. (3.22b), only two scattered modes ($n = 0$, $n = -1$) exist in this case. In Eqs. (3.24a,b), the correction factors of $\beta_1 = 0.285$ and $\beta_2 = 0.15$ were selected using polynomial interpolations for the effective width (w') and length (L') of the single beam-type scatterer.

The length of the beam-type member, suitable for realizing the retroreflection can be determined by comparing the amplitudes of two scattered modes with respect to the length variation. As shown in Fig. 3.4(b), when the length is $L = 0.013\,\text{m}$, the targeting $n = -1$ scattered mode has a peak amplitude while the amplitude of the $n = 0$ mode is very small. When the 0.013 m-long beam-type member composes the elastic metagrating, it is clearly seen in Figs. 3.4(c,d) that the longitudinal wave returns back along the incident direction (i.e., retroreflection) at the angle of $\theta_{p.ref} = -60^\circ$. Note that Fig. 3.4(c) shows the contour plots of the incident and reflected longitudinal waves when the elastic plate part containing a unit cell is

assumed to be infinitely arrayed with periodic boundary conditions along the y direction. On the other hand, Fig. 3.4(d) shows the field of $\nabla \cdot \boldsymbol{u}$ when the multiple unit cells are finitely arranged along the plate. The results shown in both of Fig. 3.4(c) and Fig. 3.4(d) represent the same conclusion that the retroreflection successfully occurs by the present metagrating that is composed of only one beam-type member. Secondly, we consider an elastic metagrating composed of two beam-type members for anomalous reflection. As illustrated in Fig. 3.5(a), the longitudinal wave impinges normally ($\theta_{p.inc} = 0^\circ$) on the elastic plate while the target reflection angle is set to be $\theta_{p.ref} = 60^\circ$. In this case, the lengths of the beam-type members and the gap between them are selected as design variables to configure the elastic metagrating. The width of two beam-type members is set to be $w = 1$ mm and the end-effect correction factors $\beta_1 = -0.12, \beta_2 = 0$ are used in Eqs. (3.24a,b). According to Eqs. (3.22a) and (3.23a), the length of a unit cell is determined to be $a = 0.1038$ m, and three scattered modes ($n = 0, \ \pm 1$) exist.

Since the targeting reflection angle corresponds to the $n = +1$ scattered mode, the appropriate lengths (L_1, L_2) of the two beam-type members and their gap ($b_2 - b_1$) should be searched to maximize the amplitude of the $n = +1$ scattered mode (i.e., P_{+1}). Fig. 3.5(b) shows a graphical method used in the searching process. Once many contour plots like Fig. 3.5(b) are obtained with respect to each allowable value of the gap between two beam-type members, then one can select a contour plot that

contains the maximum value of $|P_{+1}|$. In this case, Fig. 3.5(b) is plotted when the gap is $b_2 - b_1 = 0.04$ m, and the appropriate lengths of the beam-type members can be found to be $L_1 = 0.062$ m and $L_2 = 0.02$ m, respectively, to maximize the amplitude of the $n = +1$ scattered mode. Figs. 3.5(c) and 3.5(d) show that the normally incident longitudinal wave is reflected at the angle of 60° by the present elastic metagrating composed of two beam-type scatterers having different lengths. These examples show that elastic metagratings for anomalous reflections of longitudinal waves can be possibly built by one or two beam-type members. However, such a small number of beam-type members may not be sufficient to realize more general wave steering cases. Accordingly, we generalize the present elastic metagrating model including up to six beam- type members so as to have sufficient degrees of freedom in realizing wave steering. The number of the beam-type members is determined through various tests in the present metagrating design processes.

As a more general metagrating model, six beam-type members are aligned in the unit cell and their lengths are set to be design variables varying in the range of $0 \le L_i \le 0.07$ m ($i = 1, 2, \cdots, 6$) as illustrated in Figs. 3.6(a) and 3.6(d). The elastic metagrating, Case 1 shown in Fig. 3.6(a) is to be designed to reflect a normally incident longitudinal wave at the angle of $\theta_{p.ref} = 45^\circ$, while the metagrating, Case

2 in Fig. 3.6(d) is to return the obliquely incident longitudinal wave ($\theta_{p.inc} = 30^\circ$) to the same direction ($\theta_{p.ref} = -30^\circ$). According to Eqs. (3.22a,b), three modes ($n = 0, \pm 1$) can be scattered in Case 1, while two scattered modes ($n = 0, -1$) can propagate in Case 2. The length of the unit cell for each case is determined to be $a_{Case1} = 0.1271\,\mathrm{m}$ from Eq. (3.23a) for Case 1 and $a_{Case2} = 0.0899\,\mathrm{m}$ from Eq. (3.23b) for Case 2, respectively. The relative positions of the beam-type members from the origin of the unit cell are fixed in these cases as $b_1 = a - b_6 = a/12$ $(= 0.0105\,\mathrm{m})$ and $b_i - b_{i-1} = a/6$ $(= 0.021\,\mathrm{m})$ $(i = 2, \cdots, 6)$ (see Fig. 3.2), such that the beam-type members are distributed equally along the entire metagratings. The width of the beam-type members is fixed to be uniform with $w = 1\,\mathrm{mm}$, however the end-effect correction factors in Eqs. (3.24a,b) are set to be $\beta_1 = -0.06$, $\beta_2 = 0$ for Case 1, and $\beta_1 = 0.05$, $\beta_2 = \{0.1024,\ 0.1400, -0.0251,\ -0.0579,\ 0.0216,\ 0.0030\}$ for Case 2, respectively.

Since Cases 1 and 2 deal with multiple design variables, an employment of optimization algorithms may facilitate to find their optimal values. Using the method of moving asymptote [102], a gradient-based algorithm, we solve inverse problems formulated as minimization problems with six design variables $\{L_1, L_2, L_3, L_4, L_5, L_6\}$. The objective function for the minimization problem is $\min_{L_i} f_{Case1} = \min_{L_i} \left[|P_{-1}| + |P_0| - |P_{+1}| \right]$ for Case 1 and $\min_{L_i} f_{Case2} =$

$\min_{L_i}\left[|P_0|-|P_{-1}|\right]$ for Case 2. In other words, the amplitudes of targeting scattered modes (P_{+1} for Case 1 and P_{-1} for Case 2) are maximized, while those of the other modes are suppressed as illustrated in Figs. 3.6(a) and 3.6(d).

As shown in Figs. 3.6(b,c) and Figs. 3.6(e,f), respectively, the designed elastic metagratings for Cases 1 and 2 realize anomalous reflections successfully. In Case 1, the normally incident longitudinal wave is reflected from the designed metagrating at the target reflection angle $\theta_{p.ref} = 45^\circ$ in Figs. 3.6(b,c). And the metagrating designed for Case 2 returns the obliquely incident longitudinal wave in the same direction ($\theta_{p.ref} = -30^\circ$) in Figs. 3.6(e,f). In Case 1, the lengths of the beam-type members are found to be $\{L_1, L_2, L_3, L_4, L_5, L_6\}_{Case1} = \{0.02007, 0.02105, 0.05967, 0.06132, 0.06180, 0.06206\}$ m. The ratios of the power flows among the three scattered modes are calculated as $I_{-1} : I_0 : I_{+1} = 0.6357 : 0 : 0$. This means that more than 60 % of incident power of the longitudinal wave is reflected along the target direction. The remaining power of the incident longitudinal wave is transferred into a shear wave, which is not the field of main interest in this study. For Case 2, the lengths of the beam-type members are found to be $\{L_1, L_2, L_3, L_4, L_5, L_6\}_{Case2} = \{0.01666, 0.016, 0.02231, 0.0238, 0.0193, 0.02009\}$ m. The power flow ratio between the $n = -1$ and $n = 0$ modes is $I_{-1} : I_0 = 0.4552 : 0.0180$. This result indicates that although approximately 2 % of the incident longitudinal wave

power is scattered into an unwanted mode ($n = 0$), the power of the desired retroreflected longitudinal wave ($n = -1$) is 25 times larger than that of the mode.

As next examples, elastic metagratings are designed to split a normally incident longitudinal wave into two reflected longitudinal waves. The first elastic metagrating is to split the incident longitudinal wave into two reflected waves at different angles, while the second one is to control the relative amplitudes in the splitting directions. The generalized metagrating model composed of six beam-type members is used to design both beam splitters.

In the design of metagratings for the beam splitter, it is noted that one can determine only one reflection angle while the other reflection angle is automatically decided among the scattered modes by the corresponding length of the unit cell. This means that it is useful to select one reflection angle, which provides a more number of scattered modes. When the target reflection angle $\theta_{p.ref1} = -25^\circ$ is selected, five scattered modes ($n = 0, \pm 1, \pm 2$) are expected by Eq. (3.22a) as illustrated in Fig. 3.7(a). The corresponding unit cell has a length of $a = 0.2127$ m according to Eq. (3.23a). In Fig. 3.7(a), the beam-type members are positioned equally from each other within the unit cell, such that the gaps between neighboring beam-type members are set to be $b_1 = b_i - b_{i-1} = a - b_6 (= a/7 = 0.03\,\text{m})$ $(i = 2, \cdots, 6)$ in the unit cell (see Fig. 3.2). Such equally separated members within the unit cell (not in the metagrating) are for a better convergence during solving the minimization

problem involving five scattered modes. Note that a search for an optimized gap between scatterers is an important issue as discussed in the acoustic metagratings work [37]. The width of the beam-type members is set to be $w = 1\ \text{mm}$ and the end-effect correction factors in Eqs. (3.24a,b) are selected to be $\beta_1 = 0.04$ and $\beta_2 = 0$.

As illustrated in Fig. 3.7(a), we intend to split the normally incident longitudinal wave into the angles of $\theta_{p.ref1} = -25^\circ$ and $\theta_{p.ref2} = 57.7^\circ$, corresponding to the $n = -1$ and $n = 2$ scattered modes, respectively. The appropriate lengths of the six beam-type members are searched by minimizing an objective function $\min_{L_i} f = \min_{L_i} \left[|P_{-2}| - |P_{-1}| + |P_0| + |P_{+1}| - |P_{+2}| \right]$ using the optimization algorithm. As a result, the lengths of six beam-type members are found as $\{L_1, L_2, L_3, L_4, L_5, L_6\} = \{0.06128,\ 0.06163,\ 0.01988,\ 0.06064,\ 0.06145,\ 0.02155\}$ m. As clearly seen in Fig. 3.7(c), the elastic metagrating built by those lengths split the normally incident wave into two longitudinal waves along the designated directions. The complicated scattered field shown in Fig. 3.7(b) is due to the overlap of the two differently scattered waves. When the power flows are calculated in terms of the scattered modes, the ratio of power flow reaches $I_{-2} : I_{-1} : I_0 : I_{+1} : I_{+2} = 0 : 0.2368 : 0 : 0 : 0.2578$. Except for the power transformed into the reflected shear waves, the reflected longitudinal waves are directed as designated.

As the last example, an equiangular beam splitter is to be realized by the present generalized metagrating model. For the normally incident longitudinal wave, the target reflection angles are set to be $\theta_{p.ref1} = -60^\circ$ and $\theta_{p.ref2} = 60^\circ$. In addition, the ratio of the amplitudes of the target scattered modes is prescribed to be $|P_{-1}| : |P_{+1}| = 1 : 0.85$ in this beam splitter. The length of the unit cell is determined to be $a = 0.1038\ \mathrm{m}$ and three scattered modes are in consideration as illustrated in Fig. 3.8(a). Except for the end-effect correction factors $\beta_1 = -0.12$ and $\beta_2 = 0$, the remaining geometric conditions are identical with the previous anomalous reflection examples shown in Fig. 3.6.

By minimizing the objective function $\min_{L_i} f = \min_{L_i} \left[|P_0|^2 + \left| |P_{+1}| / |P_{-1}| - 0.85 \right|^2 \right]$, the lengths of the beam-type members for the metagrating realizing the equiangular beam splitter are found to be $\{L_1, L_2, L_3, L_4, L_5, L_6\} = \{0.01970,\ 0.06509,\ 0.06109,\ 0.04680,\ 0.03658,\ 0.02075\}$ m as shown in Fig. 3.8(a). The power flows into the three scattered directions are $I_{-1} : I_0 : I_{+1} = 0.2862 : 0.0278 : 0.1992$. Then, as shown in Fig. 3.8(c), the most of the reflected longitudinal wave are separated into the target angles of $\theta_{p.ref1} = -60^\circ$ and $\theta_{p.ref2} = 60^\circ$, corresponding to $n = -1$ and $n = 1$, respectively. By integrating the values of $\nabla \cdot \boldsymbol{u}$ along the wavefront, at locations 10 wavelengths from the center of the domain, the amplitude ratio of the two anomalously reflected longitudinal waves

reaches $\mathrm{Amp}_{-1} : \mathrm{Amp}_{+1} = 1 : 0.8781$. Thereby, the relative ratio between the amplitudes realized by the present elastic metagrating agrees quite well with the prescribed values ($1 : 0.85$) within around 3 % difference. Note that it would be very difficult for gradient-type metamaterials to realize the functionality of the present beam splitter that is capable to achieve relative amplitude control.

3.5 Analysis of the phenomenon

Examining the configurations of the elastic metagratings shown in Figs. 3.4-3.8 alone, it is difficult to predict how the target wave steering can be realized by a single or a set of simply configured beam-type members. In this section, the significance of searched lengths of the beam-type members is physically investigated and some of the resulting metagratings are experimentally verified.

3.5.1 Experimental verification

As experimental verification of the present elastic metagratings for anomalous longitudinal wave steering, two metagratings designed for an anomalous reflection at the angle of 45° (in Figs. 3.6(a-c)) and beam splitting with the angles of -25°, 57.7° (in Figs. 3.7(a-c)) are actually manufactured. Fig. 3.9(a) shows the experimental setup in which the metagrating array is fabricated in the 1mm-thick aluminum alloy plate for the anomalous reflection at an angle of 45°. The array ($1030\,\text{mm} \times 75\,\text{mm} \times 1\,\text{mm}$) consists of five unit cells whose geometrical dimensions are the same with those in Section 3.4 and is protected by an outer frame in a width of $25\,\text{mm}$ (Note that the metagrating array for the beam splitter consists of four unit cells.). Since we consider in-plane longitudinal waves only, the lowest symmetric Lamb wave (S_0) is excited in the aluminum alloy plate, which makes good correspondence to the longitudinal wave in bulk media [103].

As shown in Fig. 3.9(a), the magnetostrictive patch transducer (MPT) was used to actuate in-plane longitudinal waves in the plate at 60 kHz [104]. A nickel patch with the dimensions of $400\,\text{mm} \times 41\,\text{mm} \times 0.1\,\text{mm}$ was used as the magnetostrictive element in the MPT. The MPT was installed $300\,\text{mm}$ away from the metagrating array. The line source signal (30 cycles of a sinusoidal wave) was generated in a function generator (Agilent 33220A) and amplified through a power amplifier (AG 1017L). The scattered in-plane longitudinal waves were measured using an electromagnetic acoustic transducer (EMAT) along the circle of a radius 500 mm. In order to obtain the radiation pattern, 23 measurement points ($-80^\circ \sim 80^\circ$ (10° interval), -45°, 37.5°, 42.5°, 45°, 47.5°, 52.5°) were used for the anomalously reflecting experiment, while 19 points ($-80^\circ \sim 80^\circ$ (10° interval), -25°, 57.7°) were used for the beam splitting. Measured signals were amplified (SR 560) and stored in an oscilloscope (Waverunner 620Zi). For every measurement location, four measurements were averaged. Since the MPT is installed inside the measurement points, the effect of MPT to a reflection signal should be considered. However, when analyzing the experimental data on traction-free surface, the signal for normal incident and reflective wave doesn't have much difference. Therefore, the effect of MPT on the reflective wave is thought be small.

Figs. 3.9(b) and 3.9(c) compare the experimental results with the numerical predictions for the anomalous reflection (described in Fig. 3.6(a-c)) and the beam splitter (described in Fig. 3.7(a-c)), respectively. In both cases, the experimental

radiation patterns exhibit consistent results with the numerical predictions. Fig. 3.9(b) shows that the in-plane longitudinal wave is successfully steered at the target reflection angle of 45°. Fig. 3.9(c) also shows successful splitting of the incident wave into two beams at the target reflection angles of -25° and 57.7°. Some differences between the experimental and numerical results appear to be caused in the fabrication procedure of the metagratings, for example, slight distortions due to extreme heat from laser precision cutting. The fabrication error by laser precision cutting is within the range of ± 0.05 mm. However, when numerically simulated the metagrating structure with length/width difference of ± 0.05 mm, high performance of longitudinal wave steering is still observed. Therefore, we can conclude that our experimental result is consistent with this fabrication error.

3.5.2 Physical interpretation

To physically interpret the length variations of the beam-type members in the designed metagratings, we consider the unit cell of the present metagratings as a super cell consisting of multiple subcells. In other words, we separate the designed unit cell into the six subcells, each of which is composed of a narrow elastic plate part and an attached beam-type member. Then, as shown in Figs. 3.10(a) and 3.10(b), we compare the reflected longitudinal wave fields ($\nabla \cdot \boldsymbol{u}$) in the subcells when the same longitudinal wave impinges on each of them.

The six subcells in Fig. 3.10(a) is divided from the metagrating unit cell shown in Fig. 3.6(a), which is for anomalous reflection of $\theta_{p.ref} = 45^{\circ}$ for a normal incidence. As observable in Fig. 3.10(a) (and also in Fig. 3.6(a)), the lengths of the left two beam-type members are very close to each other ($\{L_1, L_2\} = \{0.02007\ \text{m}, 0.02105\ \text{m}\}$), while the other four members have the similar lengths together ($\{L_3, L_4, L_5, L_6\} = \{0.05967\ \text{m},\ 0.06132\ \text{m},\ 0.06180\ \text{m},\ 0.06206\ \text{m}\}$). When we assume that the two representative lengths are $0.02\ \text{m}$ and $0.06\ \text{m}$ for simplicity, they correspond to the longitudinal vibrational resonances of the beam-type member at the exciting frequency (60 kHz), specifically, the quarter-wavelength and three-quarter-wavelength resonances, respectively. When the beam-type members have the similar lengths around the resonating dimensions, they produce a significant phase shift at the resonating frequency. This is the reason why the lengths of the six beam-type members are determined to be around the resonating dimensions in the present metagrating. The plot in Fig. 3.10(a) confirms that the accumulated phase shifts produced by the six subcells cover a 2π span over the unit cell of the metagrating.

Similarly, Fig. 3.10(b) shows the reflected longitudinal waves when the identical longitudinal wave is incident on each of subcells, which construct the unit cell of the metagrating shown in Fig. 3.7(a) for realizing the beam splitter. Note that the beam-type members are positioned equally within the unit cell in this example. Accordingly,

the unit cell is divided into 7 subcells including one with free surface as shown in Fig. 3.10(b). Note that in Fig. 3.10(b) (also in Fig. 3.7(a)), the lengths of the beam-type members are around either 0.02 m or 0.06 m, which are the representative dimensions for resonance at the exciting frequency. (Recall $\{L_1, L_2, L_3, L_4, L_5, L_6\} = \{0.06128, 0.06163, 0.01988, 0.06064, 0.06145, 0.02155\}$ m.) As indicated and replotted in Fig. 3.10(b), the selective phase shifts among the subcells successfully produce two kinds of 2π span over the unit cell of the beam-splitting metagrating. More precisely, the plot in Fig. 3.10(b) shows that the phase gradients of the $n=-1$ and $n=+2$ modes (corresponding to $\theta_{p.ref1} = -25^\circ$ and $\theta_{p.ref2} = 57.7^\circ$) are $\left|\left(\Delta\phi/\Delta x\right)_{n=-1}\right| = 2\pi / a$ and $\left|\left(\Delta\phi/\Delta x\right)_{n=+2}\right| = 2\pi / (a/2)$, respectively.

The physical interpretation of the relation between the length variations of the generalized beam-type metagrating members and the target wave steering, which was obtained from Fig. 3.10, is also applicable in case of the metagratings using small numbers of beam-type members in Figs. 3.4 and 3.5. More detailed explanations on the phase modulation in these elastic metagratings are provided. The metagrating unit cell consisting of single beam-type member in Fig. 3.4(a) is divided into two subcells, while that using two beam-type members in Fig. 3.5(a) is partitioned into three subcells in order to predict the phase profile by comparing the reflected longitudinal waves in each of the subcells.

To explain the phase modulation in the elastic metagratings using one or two beam-type members (i.e., Fig. 3.4(a) and Fig. 3.5(a), respectively), the unit cell of the single-membered metagrating (Fig. 3.4) is divided into two subcells and that of the two-membered metagrating (Fig. 3.5) is partitioned into three subcells; see, Fig. 3.11(a) and Fig. 3.11(b), respectively. The contour plots in Figs. 3.11(a,b) show the reflected longitudinal wave fields ($\nabla \cdot \boldsymbol{u}$) in the subcells for normally incident, identical longitudinal waves.

In Fig. 3.11(a), the two subcells exhibit both longitudinal and flexural motions, because a longitudinal wave impinges on them obliquely ($\theta_{p.inc} = 60^{\circ}$). The beam-type member in the subcell produces an abrupt phase change in the scattered field, because the length (0.013m) of the member is designed to be around the length generating the three-quarter-wavelength flexural resonance at the exciting frequency (60 kHz). The accumulated phase shift produced by the two subcells becomes 2π over the unit cell of the metagrating as demonstrated in Fig. 3.11(a). Similarly, the three subcells in Fig. 3.11(b) include two beam-type members and one free surface. The lengths of the designed beam-type members are around 0.06 m and 0.02 m, respectively, which are the representative dimensions for longitudinal resonances at the exciting frequency as discussed in Fig. 3.10. As indicated and replotted in Fig. 3.11(b), the accumulated phase shift by the three subcells covers a 2π span over the unit cell of the metagrating.

These concept of phase modulation is widely used to design phase-gradient

metasurface. Since phase-gradient term in generalized Snell's law and diffraction mode term of 1st mode in diffraction grating theory is identical, such phase modulation method can be used to explain the periodic structures such as metagratings.

3.6 Concluding remarks

To resolve inefficiency in wave steering with widely used metasurfaces, we investigated and designed metagratings and successfully suppressed the undesired modes in scattered waves. Specifically, a novel elastic metagrating model was proposed in this work for efficient anomalous reflections of elastic longitudinal waves. The present elastic metagratings consisted of a periodic arrangement of a single or array of beam-type elastic members that were attached to the boundary of the elastic continuum medium. The slender and straight beam-type members were modeled to have both longitudinal and flexural motions to thoroughly manage elastic wave propagation. The interface coupling conditions were analytically established between the elastic plate and beam-type members. To suppress undesired higher modes in the scattered waves, a set of appropriate geometric parameters of the beam-type members were determined by solving inverse problems formulated as minimization problems. Through several case studies, the proposed elastic beam-type metagratings were found to be useful to realize anomalous reflections and asymmetric splittings of longitudinal elastic waves. Some of the designed elastic metagratings were actually manufactured and their steering performances were experimentally verified. It is expected that the proposed elastic metagratings can pave the way for practical applications, such as non-destructive structural health monitoring and medical imaging.

Throughout the chapter, we solved the simplified version of the main problem. Even though the present study is limited to longitudinal waves, the analysis and design of

the present metagratings can be extended to manipulate both longitudinal and shear waves. In the following chapter, work on manipulating all of the diffraction modes of longitudinal and shear waves will be introduced. By these studies on elastic metagratings, we are managed to solve the problem of simultaneous mode conversion and wave steering.

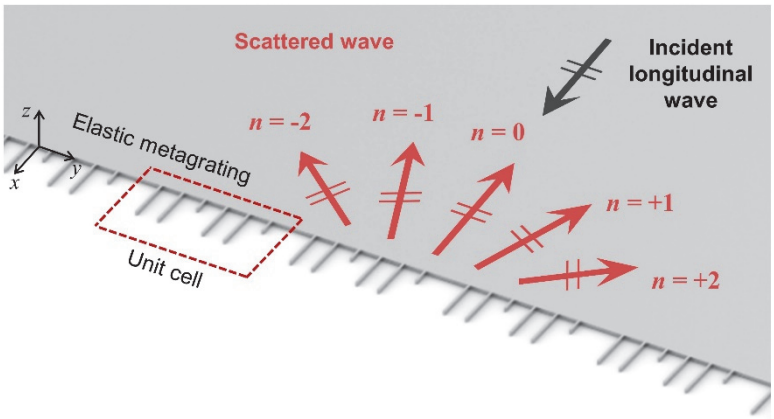

Fig. 3.1 A schematic illustration of the elastic metagratings constructed with a periodic array of beam-type members. A unit cell composed of multiple beam-type members is attached to the elastic continuum plate where the longitudinal waves are scattered.

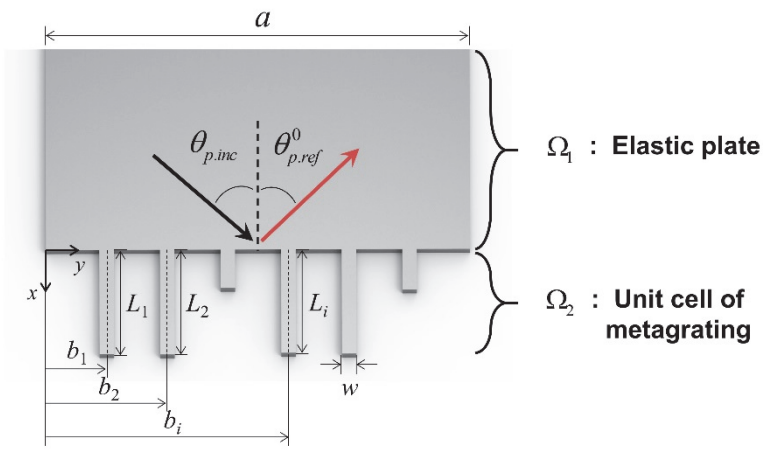

Fig. 3.2 The unit cell of the elastic grating with geometric parameters.

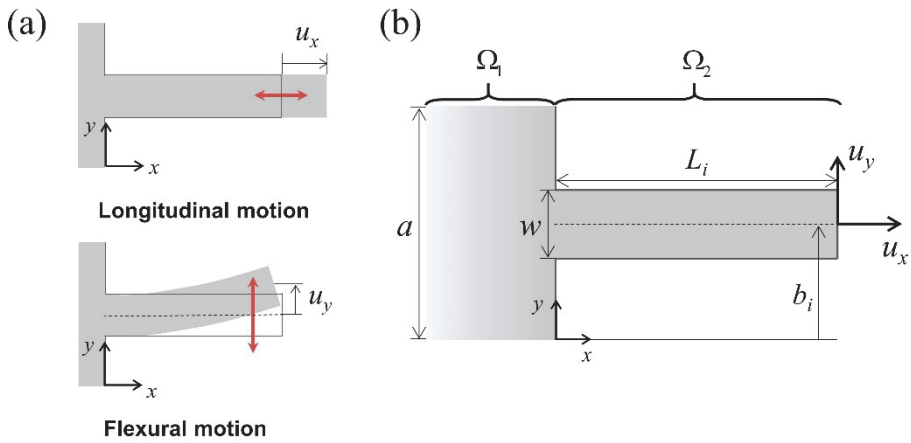

Fig. 3.3 (a) Illustrations of the longitudinal and flexural motions of a beam-type member. (b) The interface between elastic continuum plate Ω_1 and a beam-type member in Ω_2.

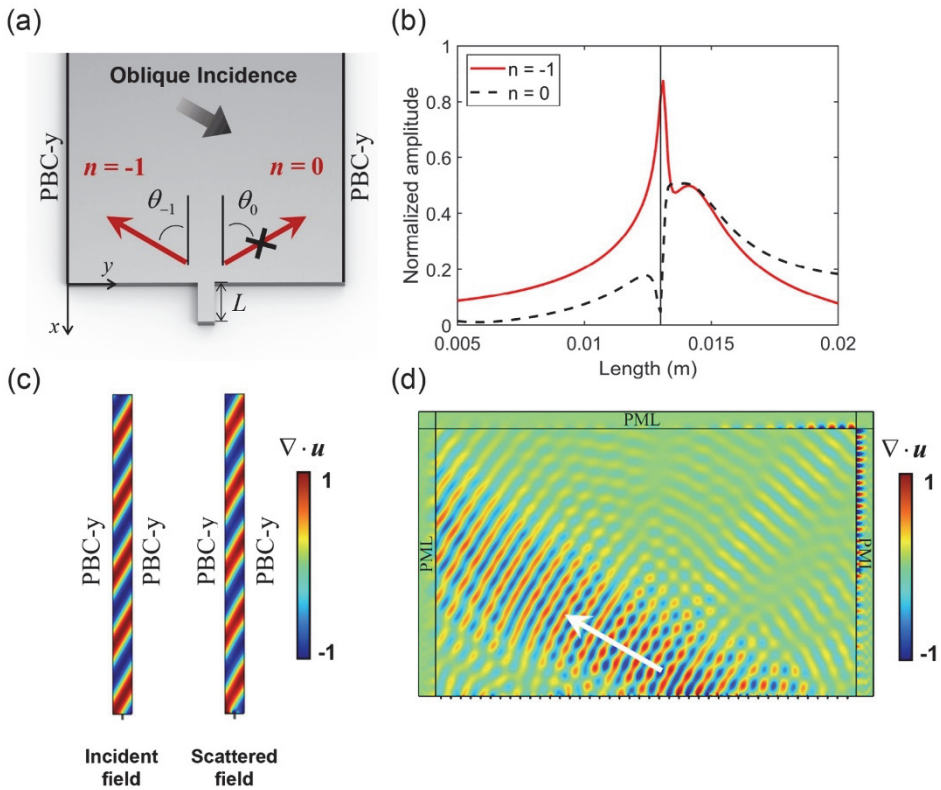

Fig. 3.4 The elastic metagrating using a single beam-type member for retroreflection at oblique incidence. (a) The problem definition ($\theta_0 = 60^\circ, \theta_{-1} = -60^\circ$), (b) the amplitudes of the normalized modes for the varying length of the beam-type member, (c) numerical simulations of the incident (left) and scattered (right) longitudinal fields, (d) a 2D simulation of the retroreflection from the elastic metagrating array.

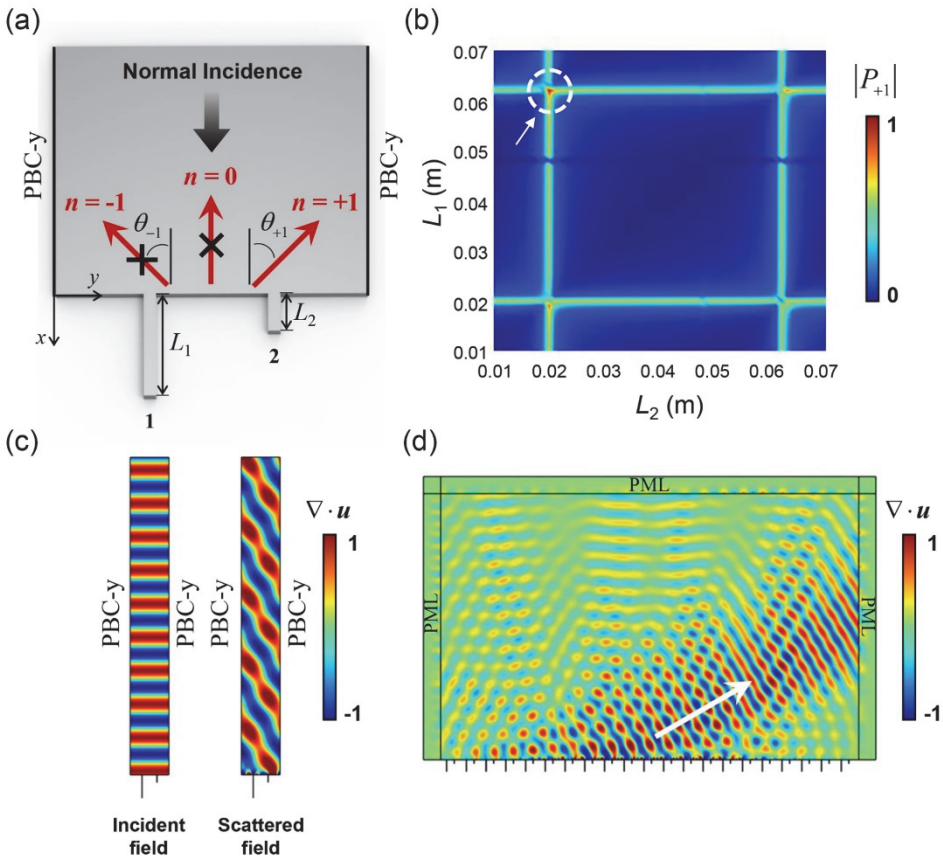

Fig. 3.5 The elastic metagratings using two beam-type members for anomalous reflection at normal incidence. (a) The problem definition ($\theta_{\pm 1} = \pm 60^{\circ}$), (b) the amplitudes of the normalized mode amplitudes for the varying length of two beam-type members at the gap distance of 0.04 m, (c) numerical simulations of the incident (left) and scattered (right) longitudinal fields, (d) the 2D simulation of the anomalous reflection at the angle of 60° from the elastic metagrating array.

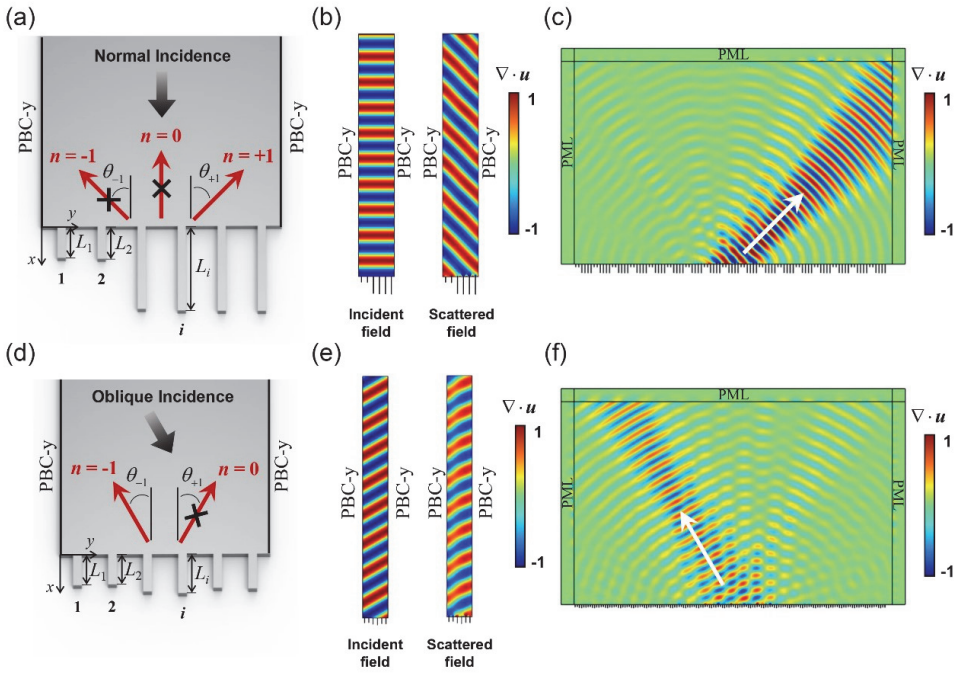

Fig. 3.6 The anomalous reflection at normal incidence using the designed beam-type metagrating ($\theta_{\pm1} = \pm45^\circ$, $[L_1, \cdots, L_6]$ = [0.02007, 0.02105, 0.05967, 0.06132, 0.06180, 0.06206] m). (b,c) The corresponding wave fields in the periodic unit cell and the 2D simulation results of anomalous reflection, respectively, for the problem defined in (a). (d) The retroreflection using the designed beam-type metagrating ($\theta_0 = 30^\circ, \theta_{-1} = -30^\circ$, $[L_1, \cdots, L_6]$ = [0.01666, 0.016, 0.02231, 0.0238, 0.0193, 0.02009] m). (e,f) The corresponding wave fields in the periodic unit cell and the 2D simulation results of retroreflection, respectively, for the problem defined in (d).

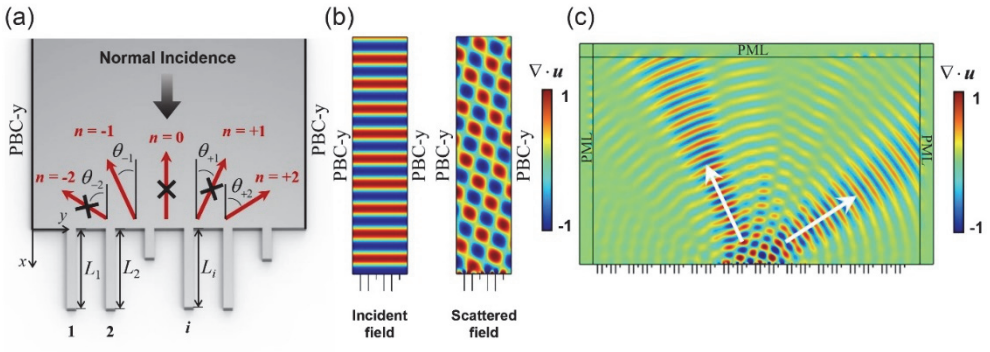

Fig. 3.7 Beam splitting using the designed metagrating. (a) The problem definition and the designed lengths of the beam-type members ($\theta_{\pm 1} = \pm 25^{\circ}$, $\theta_{\pm 2} \approx \pm 57.7^{\circ}$, [$L_1, \cdots, L_6$] = [0.06128, 0.06163, 0.01988, 0.06064, 0.06145, 0.02155] m.), (b) the wave fields in the periodic unit cell, (c) the 2D numerical simulation of beam splitting at two different angles.

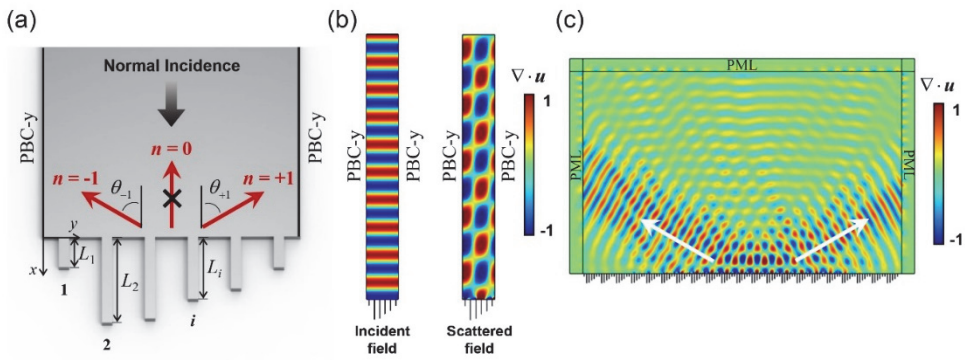

Fig. 3.8 Equiangular beam splitting using the design metagrating. (a) The problem definition and the resulted lengths of the beam-type members ($\theta_{\pm 1} = \pm 60^{\circ}$, $\mathrm{Amp}_{-1} : \mathrm{Amp}_{+1} = 1 : 0.85$, $[L_1, \cdots, L_6]$ = [0.01970, 0.06509, 0.06109, 0.04680, 0.03658, 0.02075] m.), (b) the wave fields in the periodic unit cell, (c) the 2D numerical simulation of equiangular beam splitting.

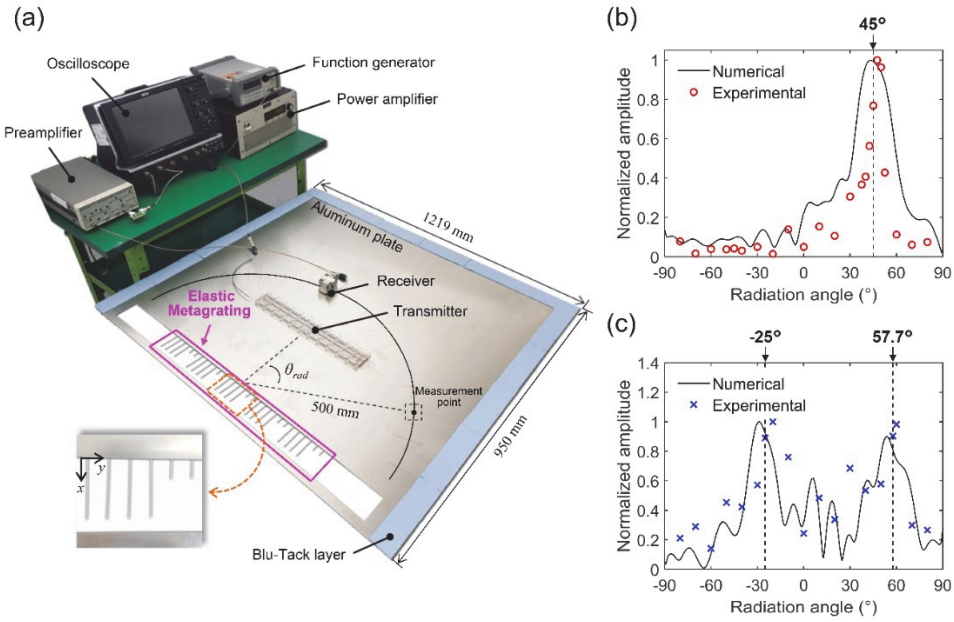

Fig. 3.9 The experimental setup and result data for verification. (a) The experimental setup with an illustration of the designed elastic metagrating array manufactured in the aluminum alloy plate. (b) The variation of the normalized amplitudes of the reflected longitudinal wave for the anomalous reflection considered in Fig. 3.6(a). (c) The variation of the normalized amplitudes of the reflected longitudinal wave for the beam splitting considered in Fig. 3.7(a).

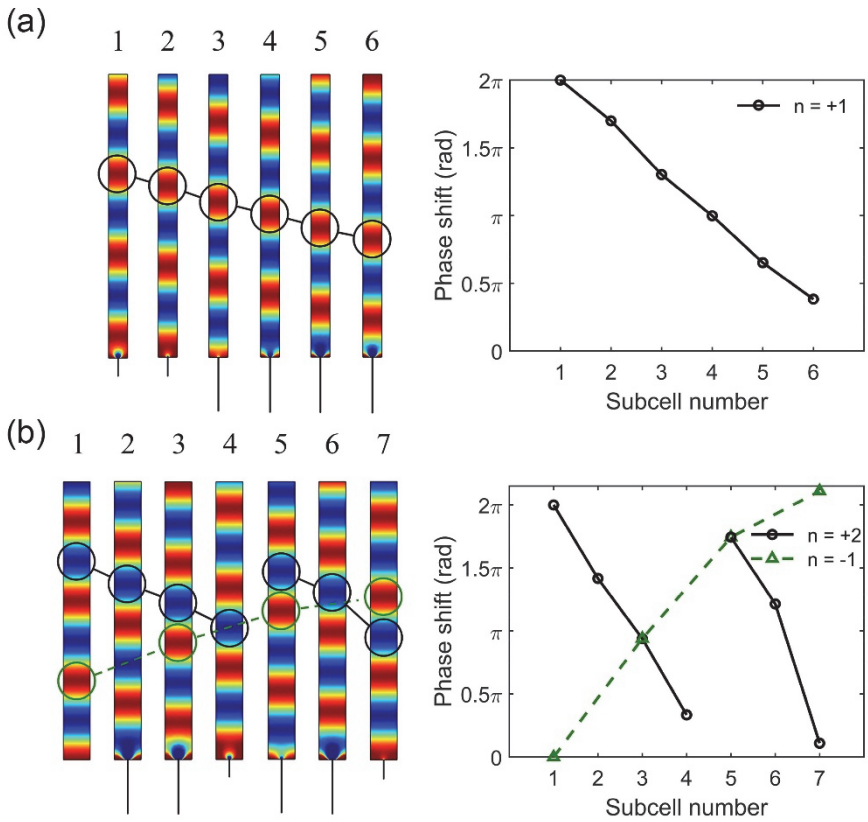

Fig. 3.10 The reflected longitudinal wave fields and the phase profiles over the subcells. (a) The phase profiles in subcells of the metagrating for the abnormal reflection considered in Fig. 3.6(a) and the plot of the phase shift in the scattered longitudinal waves. (b) The phase profiles in subcells of the metagrating for the beam splitting considered in Fig. 3.7(a) and the plot of the phase shift in the scattered longitudinal waves.

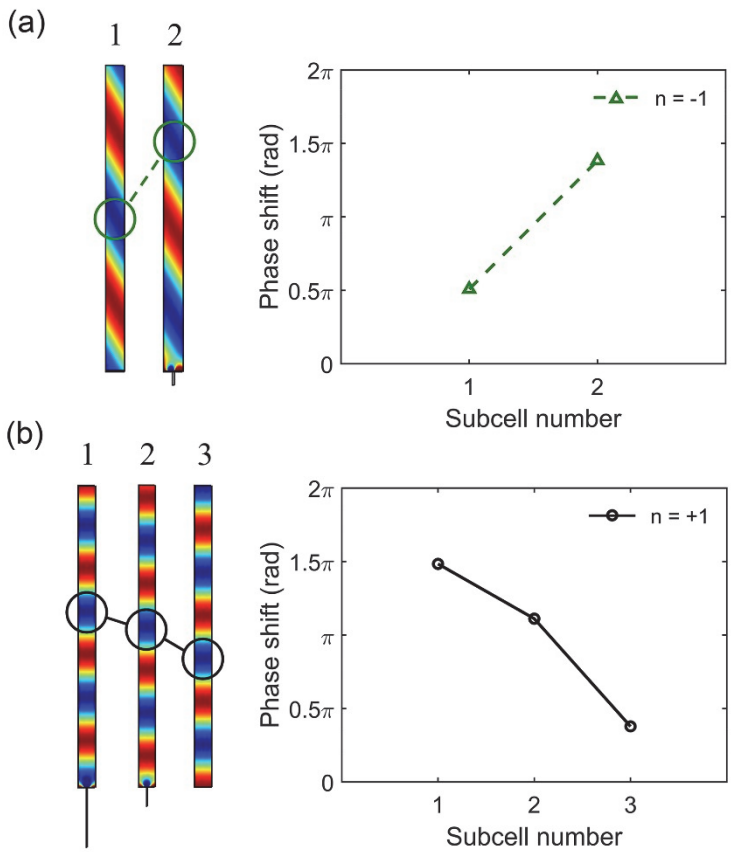

Fig. 3.11 The reflected longitudinal wave fields and the phase profiles over the subcells. The phase profiles in the subcells of the metagrating considered in (a) Fig. 3.4(a) and (b) Fig. 3.5(a). The phase shifts in the scattered longitudinal waves are plotted.

CHAPTER 4.

Elastic Metagratings for Anomalous Mode Converting Reflection

The contents covered in this chapter were published through the journal paper [113].

4.1 Chapter overview

Elastic waves have been applied to detect small invisible defects inside solid elastic media, such as for structural health monitoring [1] and ultrasonic nondestructive testing [2]. For the high performance in such applications, the resulted propagating diffraction modes and directions in the scattered wave field should be manipulated carefully. However, the efficient control of mode conversion and/or wave steering of elastic waves is hard to realize, owing to the properties of the polarization and dispersion of elastic wave motions. Such difficulty occurs even under the incidence of a single-mode elastic wave. In this case, various diffraction modes are scattered in different directions from boundaries or inhomogeneous interfaces [3,4]. Also, additional wave signals are disturbance in the sense of signal processing. Conventionally, taper-shaped wedges are used for mode conversion of elastic waves to manipulate the reflected waves. These taper-shaped wedges are designed using

the critical angle, and for the critical incidence, only one elastic mode propagate, while other elastic modes become evanescent [2,3]. However, these conventional taper-shaped wedges which employ critical angles depend on the working conditions. And this leads to poor efficiency of mode conversion and wave steering. Hence, efficient manipulation of both mode conversion and/or wave steering are still required in elastic wave applications.

An artificially engineered structural materials, so-called metamaterials, have recently appeared and widely researched, because of their potential for tailoring extreme characteristics in wave propagation [5-12]. There have been various forms of metamaterials which have been proposed for mode conversion or filtering of elastic waves by using anisotropic properties [13-15], negative mass and stiffness [16-18], Fabry–Pérot resonance [19-21], and bimodal impedance matching [22,23]. Especially, in [19-21], using the Fabry–Pérot resonance, an incident longitudinal (shear) wave was entirely converted via an anisotropic metamaterial layer into a shear (longitudinal) wave. Such anisotropic metamaterial layer which can apply in the obliquely incidence of elastic waves has also been researched [24]. While these various metamaterials facilitated highly efficient mode conversion in the refraction and transmission of elastic waves, anomalous wave steering in the reflective wave field was not investigated.

Metasurfaces, which are planar versions of metamaterials with small thickness compared to wavelength have been studied for realizing the anomalous steering of elastic waves. Almost all of metasurface researches, the generalized Snell's law [25]

has been employed to realize the anomalous steering of reflected and/or refracted waves by forming various types of phase gradients. For example, linear phase gradient along the boundary can steer the wavefront of reflected wave with anomalous angle. Among them, aligned gaps were set in an elastic plate to produce phase gradients for steering longitudinal or flexural waves [26,27]. An effective model of special form of mass-stiffness substructures was proposed to refract longitudinal waves in an elastic plate [28]. The disordered pillar resonators were installed on an elastic plate for anomalous deflection and focusing of flexural waves [29]. However, these metasurfaces are based on the design of phase gradients on the boundary. And these phase-gradient metasurfaces inevitably generate undesired multiple diffraction modes, because multi-dimensional non-local effects are not fully considered in wave scattering phenomena [30]. That is, the generalized Snell's law has no mechanism for controlling the scattered modes from the boundaries and inhomogeneous interfaces of wave propagating media. From this result, the efficiency of wave manipulation using phase gradient-based metasurfaces is inherently low. In addition, the mode conversion functionality is fundamentally limited, because the mechanism of generalized Snell's law only works for the wave steering.

To manipulate every high-order diffraction modes of scattered waves, researchers have newly proposed and investigated the metagratings that are governed by the diffraction grating theory [31,32] for electromagnetic [30,33-36] and acoustic wave fields in fluids [37-57] and, very recently for elastic wave field in solids [58-62]. In

the metagrating for manipulating flexural waves, several group of point scatterers based on a mass-spring model were arranged to control wavefronts of flexural waves [58,59], and phased grating elements were added to a superstrate of the elastic plate to manipulate guided waves [60]. For anomalous steering of in-plane elastic waves, metagratings with beam-type members were proposed and realized anomalous reflection of longitudinal waves [61].

As discussed above, most of the previous metamaterial designs have primarily focused on the mode conversion or anomalous steering of scattered waves; the simultaneous manipulation of the reflected wave mode and the direction of the scattered elastic waves remains challenging. As illustrated in Fig. 4.1(a), a normally incident longitudinal (or shear) wave propagating towards the free end of a thin elastic plate is scattered as both the longitudinal and shear waves with multiple reflection angles. Multiply scattered diffraction modes should be carefully manipulated for mode conversion along the designated angle of reflection with undesired waves suppressed.

The work in this chapter proposes a new strip-type elastic metagrating to realize the highly efficient mode conversion and wave steering of a desired mode in a scattered reflection field. The design of the metagratings is based on the diffraction grating theory. We formulate the design problem as an optimization problem and identify the optimal elastic metagrating configuration that fulfills our goal. We demonstrate that when the proposed metagratings are installed along the traction-free boundary of a thin elastic plate, a normally incident plane longitudinal (or shear) wave can be

precisely converted into a shear (or longitudinal) wave at a designated angle of reflection. As illustrated in Figs. 4.1(a,b), the designed metagratings consist of periodically repeated unit cells constructed with multiple rectangular strips. The elastic plate and rectangular strips in the metagratings are modeled as two-dimensional continuum media. This model fully describes the coupled in-plane motions of longitudinal and shear waves. The amplitudes of multiply scattered diffraction modes from the boundary are numerically evaluated using the spatial fast Fourier transform of the wave field, as simulated using the finite element method. Design optimization is performed to determine the unit cell configurations of the metagratings, which can suppress undesired scattered diffraction modes and achieve a nearly total mode-conversion reflection. The optimal geometric dimensions of the strip-type unit cells are determined by solving optimization problems in which a gradient-based algorithm is used to update the design variables. The validity of the proposed metagratings is confirmed by numerical and experimental results.

4.2 Mathematical descriptions of the wave motion

When a longitudinal or shear wave is normally incident upon a periodically structured boundary of an elastic plate, it is scattered via both longitudinal and shear modes in multiple directions. According to the diffraction grating theory, the number of scattered modes and their directions are determined by the wave mode, incident angle, and periodicity of the unit cell forming the boundary. The coupled motions and multiple diffractions of scattered elastic waves required to simultaneously accomplish precise and efficient mode conversion and wave steering are described in this section.

4.2.1 Full wave motion in an elastic plate

The following two individual wave equations can describe wave propagation in two-dimensional thin elastic continuum media for longitudinal and shear waves, respectively, under the plane stress condition as [3,4]:

$$\nabla^2\varphi = \frac{1}{c_p^2}\frac{\partial^2\varphi}{\partial t^2}, \qquad \nabla^2\psi = \frac{1}{c_s^2}\frac{\partial^2\psi}{\partial t^2}, \tag{4.1a,b}$$

where φ and ψ are scalar potential functions for describing the longitudinal and shear wave motions, respectively, and c_p and c_s are the corresponding phase velocities with time t.

As analytical solutions for the wave equations in Eqs. (4.1a) and (4.1b), the total

potential functions φ^{total} and ψ^{total} can be expressed by superposing the incident (φ^{inc}, ψ^{inc}) and scattered (φ^{scat}, ψ^{scat}) wave potentials, each of which is written in terms of the diffraction modes:

$$\varphi^{total} = \varphi^{inc} + \varphi^{scat} = \sum_{n=-N}^{N} \left[\left(\delta_{n0} e^{-jk_{px}^{n} x} + P_n e^{jk_{px}^{n} x} \right) e^{-jk_{py}^{n} y} \right], \tag{4.2a}$$

$$\psi^{total} = \psi^{inc} + \psi^{scat} = \sum_{m=-M}^{M} \left[\left(\delta_{m0} e^{-jk_{sx}^{m} x} + S_m e^{jk_{sx}^{m} x} \right) e^{-jk_{sy}^{m} y} \right], \tag{4.2b}$$

where the time-harmonic wave motion varies with $e^{j\omega t}$ (ω: angular frequency; $j = \sqrt{-1}$). In Eq. (4.2), k denotes the wavenumber of the propagating wave. The subscripts p and s denote longitudinal and shear waves, respectively, and the subscripts x and y denote the spatial directions of wave propagation. The superscripts n and m of the wave number k denote indices of the scattered longitudinal and shear diffraction wave modes, respectively; N and M denote the total numbers of modes used in the analysis, respectively. The Kronecker deltas δ_{n0} and δ_{m0} denote the unit amplitudes of the incident longitudinal and shear wave potentials, respectively, whose corresponding amplitudes of the *n*th- and *m*th-order potentials for the scattered waves are denoted by P_n and S_m, respectively. When a longitudinal (or shear) wave is incident upon a periodically structured boundary at an angle of θ_{inc}, the longitudinal and shear waves are multiply scattered at reflection angles of $\theta_{p,ref}^{n}$ and $\theta_{s,ref}^{m}$. According to the diffraction grating theory

[31,32,99], the following two grating equations relate the scattered diffraction modes of longitudinal and shear waves to an incident wave mode, respectively:

$$k_{py}^{n} = k_p \sin\theta_{p,ref}^{n} = k_{inc} \sin\theta_{inc} + \frac{2\pi n}{a}, \tag{4.3a}$$

$$k_{sy}^{m} = k_s \sin\theta_{s,ref}^{m} = k_{inc} \sin\theta_{inc} + \frac{2\pi m}{a}, \tag{4.3b}$$

where a denotes the periodicity of unit cells along the boundary. The x-components of the wavenumbers of the scattered longitudinal and shear wave modes are given by the dispersion relation as

$$(k_{px}^{n})^2 = k_p^2 - (k_{py}^{n})^2, \qquad (k_{sx}^{m})^2 = k_s^2 - (k_{sy}^{m})^2. \tag{4.4a,b}$$

Using Eqs. (4.3a) and (4.3b), the number of propagating diffraction modes from the boundary can be predicted from amongst the theoretically infinite scattered diffraction modes. The reflection angles of the propagating diffraction modes are ranged as $-90° < \theta_{p,ref}^{n}, \theta_{s,ref}^{m} < 90°$, not to be evanescent in the elastic plate in consideration. Fig. 4.2 shows the theoretical number of propagating diffraction modes in the scattered field when a longitudinal or shear wave is incident at an angle of θ_{inc} upon a periodically structured boundary. The number of propagating modes increases for a larger periodicity, which is normalized by the respective wavelength of the incident wave type. This normalization is meaningful because the total number of modes in the present mode-converting anomalous reflection depends primarily upon the dimensions of the unit cell. As discussed in the next subsection, the

periodicity of the unit cell is determined by the target reflection angle when the incident angle is given for the prescribed excitation frequency.

4.2.2 Selection of scattered modes

To efficiently convert an incident longitudinal or shear wave into other type of waves with an anomalous reflection angle, the target scattered mode should be specified from among multiple ones. Although the number of scattered diffraction modes from a periodically structured boundary can theoretically be infinite, most of the higher modes in the scattered field are evanescent. Because the scattered angles in those higher modes exceed $90°$, they do not contribute to the scattered reflection wave field in the considered elastic plate. Therefore, the scattered diffraction modes of $n,m=0$, ±1, and ±2 can be the primary concerns in the present investigation. Among them, the modes of $n,m=\pm1$ are specified as the target diffraction modes for the present mode-converting and wave-steering elastic metagratings.

For the present metagratings, the incident longitudinal wave should be efficiently converted into a shear wave, and vice versa. Because the diffraction modes of $n=\pm1$ are specified as the target scattered modes, the scattered shear wave for longitudinal wave incidence can be obtained from Eq. (4.3b) as:

$$k_s \sin\theta_{s,ref}^{\pm1} = k_{sy}^{\pm1} = k_p \sin\theta_{p,inc} + \frac{2\pi(\pm1)}{a}. \tag{4.5a}$$

Conversely, the scattered longitudinal wave for shear wave incidence is

characterized from Eq. (4.3a) with $m = \pm 1$ as:

$$k_p \sin\theta_{p,ref}^{\pm 1} = k_{py}^{\pm 1} = k_s \sin\theta_{s,inc} + \frac{2\pi(\pm 1)}{a}. \tag{4.5b}$$

Using either Eq. (4.5a) or Eq. (4.5b), the periodicity a (i.e., length) of the unit cell for converting an incident elastic wave into other type of waves with the designated reflection angle can be determined. Because the case of $n = -1$ ($m = -1$) is identical to that of $n = +1$ ($m = +1$) owing to symmetry, the periodicity a of the unit cell for converting the longitudinal-to-shear wave mode and opposite shear-to-longitudinal wave mode are respectively determined as

$$a = \frac{2\pi}{k_s \sin\theta_{s,ref}^{+1} - k_p \sin\theta_{p,inc}}, \tag{4.6a}$$

$$a = \frac{2\pi}{k_p \sin\theta_{p,ref}^{+1} - k_s \sin\theta_{s,inc}}. \tag{4.6b}$$

Note that Eqs. (4.6a) and (4.6b) are invalid when the scattered diffraction modes of $n = 0$ and $m = 0$ are considered as the target mode. In these cases, a dummy mode can be employed to calculate an upper bound of the unit cell periodicity. The actual implementation of this technique is demonstrated by the design of Case 1 in Section 4.4. The periodicity obtained from Eqs. (4.6a) and (4.6b) is a basic requirement for the manipulation of the scattered diffraction modes from the unit cell according to the diffraction grating theory. To achieve a mode-converting elastic wave reflection, the unit cell configuration should be deliberately modeled and designed to represent the coupled motions of elastic waves.

4.2.3 Strip-type continuum members

In earlier studies, pillared resonating beams [29], mass-spring models [58,59], and narrow superstrates [60] were used to construct unit cells for manipulating flexural elastic waves. For in-plane wave motions in the elastic plate, beam-type members based on both the beam and bar theories were modeled to construct a unit cell of metagratings for anomalous steering of longitudinal waves [61]. Compared with previous works, the unit cell in this work is modeled as an elastic continuum medium to allow more diversity when representing the coupled wave motions of in-plane longitudinal and shear waves in detail.

As shown in Fig. 4.3(a), the unit cell is constructed with multiple rectangular strip members attached along the traction-free boundary of the elastic plate. The dimensions of the *i*th strip-type member ($i = 1, 2, \cdots, N_s$, where N_s denotes the total number of strip-type members) is defined by the length L_i and width w_i. The position of each strip along the surface is located by the parameter b_i in the unit cell. The total number of strip-type members N_s in the unit cell determines the degrees of freedom in the design of the metagrating unit cell. Basically, the degrees of freedom should exceed the number of diffraction modes considered in the scattered wave field. Through numerous numerical tests, it was found that two or three strip-type members are sufficient to successfully model the unit cell for the present mode-converting and wave-steering metagratings.

Note that the use of strip-shaped structural members was employed in some previous

works to control elastic waves for transmitting flexural waves [29], controlling guided waves [60], and investigating the analytical identification of scattering features of Rayleigh surface waves [105]. Compared with previous works, this study investigates the coupled motions of longitudinal and shear waves in elastic continuum media, where the precise mode conversion and anomalous wave steering are simultaneously targeted by proposing a new type of metagrating structure based on the strip-type elastic members.

4.3 Numerical method for analysis and optimization

With the proposition of the new strip-type metagrating model, the coupled motions of the longitudinal and shear waves and consequent scattered diffraction modes should be accurately analyzed and evaluated. Furthermore, the aim of mode-converting anomalous reflections should be effectively realized by a systematic process for designing the metagrating configuration. To achieve the present objective, the wave motions and multiply scattered diffraction modes are numerically analyzed using the finite element method, and an optimization design problem suitable for the selective manipulation of diffraction modes is investigated.

4.3.1 Numerical analysis and evaluation

Because the elastic plate and strip-type members in the unit cell of the present metagratings are modeled as continuum media, analytical approaches are not effective for analyzing the coupled wave motions of the longitudinal and shear waves. Therefore, in this work, the wave motions in the considered elastic media (aluminum plate with a thickness of 1 mm, $\rho = 2{,}700\ \mathrm{kg/m^3}$, $E = 70\ \mathrm{GPa}$, $\nu = 0.33$) is numerically analyzed using the finite element-based commercial software COMSOL Multiphysics®. The solid mechanics module is employed to model and analyze the in-plane wave propagation in a thin elastic plate under plane stress condition. Because of the periodicity of the unit cell in the metagratings, a section of the elastic plate attached to one unit cell is primarily considered in the analysis, using the

Floquet periodic boundary conditions (PBC-*y*) as indicated in Fig. 4.3(a). The considered frequency is set to 120 kHz, for which the wavelengths of the longitudinal and shear waves in the 1 mm-thick aluminum plate are 0.045 m and 0.026 m ($c_p = 5,394$ m/s , $c_s = 3,122$ m/s), respectively. To generate a longitudinal or shear wave in the elastic plate, a time-harmonic unit force is excited along the line positioned $H_{force} = 0.135$ m from the boundary of the elastic plate as shown in Fig. 4.3(b). The aluminum plate and strip-type members were sufficiently discretized using six-node quadratic triangular finite elements to represent the coupled motions of the longitudinal and shear waves in detail. The discretization was carried out the element size to be smaller than one-sixth of the wavelength of the shear wave in consideration. In the aspect of the convergence in finite element analyses, we set the relative tolerance to be 0.1 % error. In addition to the infinitely periodic unit cell, the scattered wave field from an array of finite unit cells is fully simulated to evaluate the performance of the designed metagratings.

To deal with the diffraction phenomenon, the amplitudes of the considered diffraction modes in the scattered wave field should be quantitatively evaluated. In this work, the fast Fourier transform (FFT) [106] is applied using the nodal displacement fields obtained from the finite element analyses; this is performed spatially in the infinitely periodic elastic plate as shown in Fig. 4.3(b). With an array of nodal displacement vectors $\mathbf{u}^{(q)}$ extracted from the line AA' ($H_{fft} = 0.3$ m away from the boundary), the amplitudes P_n and S_m of the scattered

longitudinal and shear modes are obtained through the spatial FFT as:

$$P_n = -\frac{1}{k_p^2}\sum_{q=0}^{N_q-1}\left\{\left(\nabla\cdot\mathbf{u}^{(q)}\right)e^{-j2\pi nq/N_q}\right\}, \qquad \left(n = -\frac{N_q}{2}+1, \cdots, \frac{N_q}{2}\right), \quad (4.7a)$$

$$S_m = \frac{1}{k_s^2}\sum_{q=0}^{N_q-1}\left\{\left(\nabla\times\mathbf{u}^{(q)}\right)_z e^{-j2\pi mq/N_q}\right\}, \qquad \left(m = -\frac{N_q}{2}+1, \cdots, \frac{N_q}{2}\right), \quad (4.7b)$$

where q denotes the number of equally spaced nodes used to extract the displacements for a total number of sampling points of $N_q = 1000$. In Eq. (4.7b), $(\nabla\times\mathbf{u}^{(q)})_z$ denotes the z-component of the curl field of the displacement vector. For the distances to the lines for the force excitation (H_{force}) and FFT data extraction (H_{fft}) from the boundary, they are determined much longer than the wavelengths of the considered elastic waves. Compared to H_{force}, H_{fft} should be determined more carefully to guarantee the full development of far-field reflection from the boundary, i.e., $H_{fft} \gg \lambda_{p(s)}$.

4.3.2 Design optimization method

To realize the present mode-converting and wave-steering metagratings, undesired modes from a periodically structured boundary should be suppressed such that the target mode propagates only in a designated direction. In this work, such selective manipulation of the scattered diffraction modes is accomplished by solving an optimization design problem to determine the appropriate geometric dimensions of

the strip-type members in the unit cell. The geometrical dimensions shown in Fig. 4.3(a) are set as the design variable vector $\mathbf{v}$, as $\mathbf{v} = \{r_{ij}, L_j, w_j\}^T$ ($i, j = 1, 2, \cdots, N_s;\ i < j$), where r_{ij} denotes the relative position value between two adjacent strip-type members ($r_{ij} = b_j - b_i$). The relative positions of the members are meaningful parameters because of the periodicity of the unit cell. The ranges of the design variables are set to be $0 \le r_{ij} \le 0.02$, $0 \le L_j \le 0.035$, and $0 \le w_j \le 0.015$ in meters for all of the design problems in this work. In addition, the members are not allowed to overlap with each other. The initial values of the design variables are set to be random values within the upper and lower bounds.

By suppressing the amplitudes of the undesired diffraction modes, a minimization problem can be formulated for the optimization design of the metagrating unit cell as:

$$\min_{\mathbf{v}} C(\mathbf{v}) = \min_{\mathbf{v}} \left[\sum_{\substack{n=-N \\ (n \neq n_t)}}^{N} \left| P_n(\mathbf{v}) \right| + \sum_{\substack{m=-M \\ (m \neq m_t)}}^{M} \left| S_m(\mathbf{v}) \right| \right], \tag{4.8}$$

subject to several constraint equations that account for the upper and lower bounds of the design variables. In Eq. (4.8), the amplitudes of the longitudinal and shear waves except for the target mode-converting reflection mode (indicated by n_t and m_t) are minimized.

The basic form of the optimization formulation in Eq. (4.8) can be used to solve the

design problems when one or two undesired diffraction modes are to be suppressed. However, considering the multiple scattered diffraction modes, the convergence performance of Eq. (4.8) decreases because the obtained minimum value of the objective function C does not guarantee the minimum amplitude of each undesired mode. This implies that the amplitude of each undesired mode should be selectively managed in the optimization formulation.

Alternatively, the present optimization design problem suitable for the selective suppression of multiple scattered diffraction modes is formulated as:

$$\min C(\mathbf{v}) = \min[1], \tag{4.9}$$

subject to

$$h_n(\mathbf{v}) = \Pi_{P_n} < \varepsilon, \qquad (n = -N \sim N;\ n \neq n_t), \tag{4.10a}$$

$$g_m(\mathbf{v}) = \Pi_{S_m} < \varepsilon, \qquad (m = -M \sim M;\ m \neq m_t), \tag{4.10b}$$

where h_n and g_m are the constraint equations defined as the powers Π_{P_n} and Π_{S_m} of the undesired scattered diffraction modes for the longitudinal and shear waves, respectively. It was observed that the power consideration in the constraint equations rather than the amplitude was more helpful for fast and stable convergence during the optimization design process. Since the wave amplitudes vary between the maximum and minimum values depending on the modes and propagation directions, the power representing energy is more suitable to represent the state of wave mode-converting phenomenon during optimization process.

In Eqs. (4.10a) and (4.10b), the symbol ε is a very small and positive value close to zero. Through various numerical tests, ε is set as 0.001 for the present optimization designs. Together with Eqs. (4.10a) and (4.10b), several constraint equations specifying the upper and lower bounds of the design variables are added to the optimization formulation. The details of the geometrical bounds are discussed with design examples in the next section. Note that the target converting mode n_t or m_t is not directly considered in the formulation in Eqs. (4.8), (4.9), and (4.10). By suppressing all undesired modes, the remaining target mode propagates predominantly because there is no energy dissipation mechanism in the considered elastic media.

Notably, the objective function $C(\mathbf{v})$ in Eq. (4.9) is mathematically empty with a constant value of 1. This implies that it does not behave as a general objective function. Instead, the aim of the present optimization design (i.e., the suppression of undesired scattered modes) is expressed in the multiple constraint equations in Eqs. (4.10a) and (4.10b), which effectively forces the power of undesired modes to zero. This formulation scheme can be found in topology optimization designs that dealt with multiple target modes and frequencies in vibration and wave problems [107-109]. To solve optimization problems with a gradient-based optimizer, it is necessary to compute the sensitivity information of the objective function and constraint equations with respect to the design variables. The method of moving asymptotes [102] was applied in this work as a gradient-based optimizer. Considering the small

number of design variables assigned to the unit cell, the finite difference method [110] is employed to calculate the gradients of the objective function and constraint equations with respect to the design variables.

In the perspective of the sensitivity analysis, the finite difference method was adopted to calculate the gradients of the objective function and constraints equations with respect to the design variables. In the case which use Eq. (4.8) as a minimization problem, the gradients of the objective function are calculated as:

$$\frac{\partial C(\mathbf{v})}{\partial \mathrm{v}_{\mathrm{e}}} = \frac{C(\mathbf{v}+\Delta\mathbf{v}_e) - C(\mathbf{v})}{\hat{\varepsilon}}, \tag{4.11}$$

where symbol v_{e} denotes the element of the design variable vector $\mathbf{v}$ that are the geometrical parameters of the metagratings. The increment $\Delta\mathbf{v}_e$ is defined as a vector which has small increment in each of the design variables. For example, $\Delta\mathbf{v}_e$ of r_{12} is set to $\{\hat{\varepsilon}, 0, 0, 0, 0, 0, 0, 0\}^T$ in case of eight design variables. Symbol $\hat{\varepsilon}$ is a very small and positive value, which was set to 10^{-6}.

In the case which use Eqs. (4.9) and (4.10) as a minimization problem, the gradients of the objective function and the constraints equations are calculated as:

$$\frac{\partial C(\mathbf{v})}{\partial \mathrm{v}_{\mathrm{e}}} = \frac{C(\mathbf{v}+\Delta\mathbf{v}_e) - C(\mathbf{v})}{\hat{\varepsilon}} = 0, \tag{4.12a}$$

$$\frac{\partial \widehat{h}_n(\mathbf{v})}{\partial \mathrm{v}_{\mathrm{e}}} = \frac{\widehat{h}_n(\mathbf{v}+\Delta\mathbf{v}_e) - \widehat{h}_n(\mathbf{v})}{\hat{\varepsilon}}, \tag{4.12b}$$

$$\frac{\partial \widehat{g_m}(\mathbf{v})}{\partial \mathrm{v_e}} = \frac{\widehat{g_m}(\mathbf{v} + \Delta \mathbf{v}_e) - \widehat{g_m}(\mathbf{v})}{\hat{\varepsilon}}, \tag{4.12c}$$

where $\widehat{h_n}(= h_n - \varepsilon)$ and $\widehat{g_m}(= g_m - \varepsilon)$ denote the different form of the constraint equations given in Eqs. (4.10a,b).

4.4 Design examples

Through the analysis, evaluation, and optimization processes described in the previous section, various designs for mode-converting and wave-steering metagratings were carried out. As mentioned above, normally incident plane elastic waves were considered in this work to represent the functions of mode conversion and anomalous steering apparently. However, the mathematical descriptions and numerical processes described in this work can be implemented identically for any oblique incident case.

The strip-type metagrating designs in this work were categorized into three groups according to the level of difficulty of mode-converting reflections. In the first group (Case 1), the unit cell of the strip-type metagratings was designed to convert an incident longitudinal wave into a shear wave with a specular reflection angle. Specular reflection implies that the reflected wave propagates at the same angle as the incident wave from the metagratings. The second group (Cases 2 and 3) contained the metagrating designs for mode conversion with anomalous reflection angles: an incident longitudinal(shear) wave was converted into the other type of wave with a designated reflection angle. In the third group (Cases 4 and 5), the unit cells of the metagratings were designed to split a normally incident longitudinal or shear wave into both the longitudinal and shear waves at the respective reflection angles. In addition to the three groups of metagrating designs, an industrial application of strip-type metagratings is demonstrated in the last part.

For each case in the categorized groups, the number of scattered diffraction modes considered when designing the unit cell differ, as listed in Table 4.1. These numbers were determined by the target mode and angle of the reflecting wave, as stated in Eqs. (4.3) and (4.5). The number of required strip-type members N_s in the unit cell is important for defining the feasible region in which to realize mode-converting anomalous reflections. Numerous members may provide more degrees of freedom in the design; however, this does not guarantee fast and stable convergence in the optimization process. As discussed in Section 4.2, two or three members were used to construct the unit cell in the design results.

For the first group of elastic metagrating designs (Case 1), the mode conversion in the specular reflection angle was considered. As illustrated in Fig. 4.4(a), a plane longitudinal wave was incident at an angle of $\theta_{p,inc} = 0°$ to the boundary occupied by the unit cell. Part of the elastic plate attached to one unit cell was considered under periodic boundary conditions. The existing scattered modes were predicted using the grating equations in Eqs. (4.3a) and (4.3b), by inserting $n, m = 0$ for specular reflection. Both the scattered 0th-longitudinal and shear modes can propagate with identical angles of $\theta^0_{p,ref} = \theta^0_{s,ref} = 0°$ in the scattered field. For the longitudinal-to-shear wave mode conversion, the periodicity of the unit cell was set as $a_{Case1} = 22.5$ mm. Note that Eq. (4.6a) is not valid for specular reflection, because

the term $2\pi n/a$ in Eq. (4.3a) vanishes when $n = 0$. As previously mentioned, a technique was employed to set a physically meaningful periodicity for the unit cell. We first calculated the value of the periodicity as $a = 26.0$ mm by inserting $\theta_{p,inc} = 0°$ with $\theta_{s,ref}^{+1} = 90°$ in Eq. (4.6a) as the dummy mode. Then, the dummy mode was made to be evanescent by setting the actual periodicity lower than the calculated value, such that only the 0th-order diffraction mode propagated in the scattered field.

As shown in Fig. 4.4(a), two strip-type members were considered to design the metagrating unit cell, and the design variable vector was set as $\mathbf{v} = \{r_{12}, L_1, L_2, w_1, w_2\}^T$. To realize longitudinal-to-shear wave mode conversion with specular reflection, the amplitude of the 0th-order scattered longitudinal mode $|P_0|$ was suppressed in Eq. (4.8). The initial values of the design variables at the start of the optimization were set to be random values as listed in Table 4.2. As a result of the optimization, the obtained design variables were $\mathbf{v} = \{r_{12}, L_1, L_2, w_1, w_2\}^T = \{14.14, 7.03, 9.25, 5.05, 5.10\}^T$ mm as listed in Table 4.2. Note that the unit cells shown in Fig. 4.4(a) were already configured with the obtained geometrical dimensions for visually convenient presentation. Fig. 4.4(b) shows the propagating modes in the present specular reflection and Fig. 4.4(c) shows the variation of the objective function with respect to iterations during the optimization process. While some fluctuation was observed in the objective function

history at the early stage, it reduced after several dozens of iterations; finally, the optimization converged smoothly at the 280th iteration. Figs. 4.4(d) and 4.4(e) compare the amplitudes of the scattered diffraction modes of the longitudinal ($\nabla \cdot \mathbf{u}$) and shear ($(\nabla \times \mathbf{u})_z$) waves from the unit cell in the initial state and at the end of the optimization, respectively. While the 0th-order longitudinal wave mode had a large amplitude in the initial state, this mode was totally suppressed at the end of the optimization. In contrast, the 0th-order shear wave mode whose amplitude was very small became the unique one as a result of the optimization.

The longitudinal-to-shear wave mode conversion performance of the designed unit cell in Case 1 is shown in Figs. 4.4(f) and 4.4(g). In Fig. 4.4(f), the scattered wave fields from the designed unit cell are compared to those from the initial unit cell. For a longitudinal wave incidence upon the initial unit cell, the longitudinal wave ($\nabla \cdot \mathbf{u}$) is specularly reflected, while the shear wave ($(\nabla \times \mathbf{u})_z$) does not actively propagate in the scattered field. However, the scattered wave fields from the designed metagrating unit cell showed the opposite phenomena. Without the longitudinal wave ($\nabla \cdot \mathbf{u}$) propagation, the shear wave ($(\nabla \times \mathbf{u})_z$) was only reflected from the designed metagrating unit cell at the specular angle. In Fig. 4.4(f), the scattered longitudinal potential field ($\nabla \cdot \mathbf{u}$) was contoured with repeated positive and negative values along the interface with the designed unit cell, such that the longitudinal wave could not propagate in the elastic plate. However, the scattered shear potential field ($(\nabla \times \mathbf{u})_z$) showed a strong interaction between the strip-type

members and elastic plate along the interface. The two strip-type members exhibited transverse vibrating motions in different phases. Because the designed lengths of the two members were similar, the phase difference in the shear potential field produced by the members diminished near the interface to form a specular reflection in the elastic plate, as shown in Fig. 4.4(f). From the scattered shear potential field shown in Fig. 4.4(f), it was calculated that 99 % of the incident power of the longitudinal wave was converted to the shear wave. When a finite number of unit cells were installed along the traction-free boundary of the elastic plate, longitudinal-to-shear wave-mode conversion was clearly realized as shown in Fig. 4.4(g). In addition, when the metagrating unit cell is designed for longitudinal-to-shear wave mode conversion, the opposite case (i.e., shear-to-longitudinal mode conversion) is automatically accomplished with the same unit cell configuration, owing to the reciprocity of the elastic wave propagation.

In the second design category for the present metagratings, mode conversion and anomalous reflection were considered simultaneously. Case 2 depicts the design for realizing longitudinal-to-shear wave mode conversion with a reflection angle of $\theta_{s,ref}^{+1}$, and Case 3 presents shear-to-longitudinal mode conversion with $\theta_{p,ref}^{+1}$. By inserting the target reflection angles specified as the +1st-order scattered modes ($m=+1$ and $n=+1$, respectively) in Eqs. (4.6a) and (4.6b), the required periodicity of the unit cell was determined for each case. Subsequently, the number

of propagating diffraction modes in each design case was predicted using Eqs. (4.3a) and (4.3b). Compared with the previous design in Case 1 for mode-converting specular reflection, one more strip-type member was added in the unit cells of Cases 2 and 3 to tackle the increased number of scattered diffraction modes. Then, the design variable vector was set as $\mathbf{v} = \{r_{12}, r_{23}, L_1, L_2, L_3, w_1, w_2, w_3\}^T$ for the three strip-type members.

Fig. 4.5(a) illustrates the design problem of Case 2 for realizing longitudinal-to-shear wave mode conversion with a target reflection angle of $\theta_{s,ref}^{+1} = 45°$. By inserting the reflection angle in Eq. (4.6a) with the wave propagation properties ($\lambda_p = 0.045$ m and $\lambda_s = 0.026$ m at the considered 120 kHz and $\theta_{p,inc} = 0°$), the required periodicity of the unit cell in Case 2 was calculated as $a_{Case2} = 36.79$ mm. The propagating diffraction modes from the unit cell of the calculated periodicity were predicted to be one longitudinal wave mode ($n = 0$) and three shear wave modes ($m = -1,\ 0,\ +1$) from Eqs. (4.3a) and (4.3b) as plotted in Fig. 4.5(b). Among these modes, the scattered shear mode of $m = +1$ was specified as the anomalously reflecting target mode, while the scattered longitudinal ($n = 0$) and remaining shear modes ($m = -1,\ 0$) were suppressed, as indicated by the colored arrows in Fig. 4.5(a). The alternative form of the optimization formulation with Eq. (4.9) and Eq. (4.10) was employed for Cases 2 and 3, and for the rest of the cases as well. The constraint equations in Eq. (4.10) were stated as the power of the three undesired modes, as

$h_0(\mathbf{v}) = \Pi_{P_0}$, $g_{-1}(\mathbf{v}) = \Pi_{S_{-1}}$, and $g_0(\mathbf{v}) = \Pi_{S_0}$.

Fig. 4.5(c) shows that the three constraints converge soon in the optimization process. Table 4.2 lists the obtained values of the design variables at the end of the optimization together with randomly generated initial values. As in the previous case study, the unit cells shown in Fig. 4.5(a) were already configured with the obtained geometrical dimensions. As a result of the optimization in Case 2, the undesired propagating diffraction modes appearing at the initial stage were precisely suppressed, while the amplitude of the target reflecting shear wave mode ($m = +1$) was present only at the end of the optimization as shown in Figs. 4.5(d) and 4.5(e). As shown in Fig. 4.5(f), the scattered wave fields from the designed metagrating unit cell were distinct from those obtained from the initially configured unit cell. From the initial unit cell, the 0th-order longitudinal wave was reflected by the specular reflection, and the ± 1st-order shear wave modes interfered constructively in the scattered field. On the other hand, the propagation of shear waves ($(\nabla \times \mathbf{u})_z$) from the designed metagrating unit cell was clearly observed, while the longitudinal wave ($\nabla \cdot \mathbf{u}$) could no longer propagate in the scattered field. Calculated in the scattered field shown in Fig. 4.5(f), 99 % of the incident longitudinal wave power was converted to the $45°$-angle reflected shear wave from the designed metagrating unit cell. As shown in Fig. 4.4(f) for Case 1, Fig. 4.5(f) indicates that the scattered longitudinal potential field ($\nabla \cdot \mathbf{u}$) is not developed because the strip-type members do not interact with the elastic plate along the interface. The strip-type members

produce a transversely vibrating shear potential field ($(\nabla \times \mathbf{u})_z$), in which the shear wave propagates in the oblique direction as designated. When the designed unit cells were multiply arranged along the traction-free boundary of the plate, the longitudinal-to-shear wave mode conversion was clearly achieved with a target reflection angle of $\theta_{s,ref}^{+1} = 45°$ as shown in Fig. 4.5(g).

Case 3 aims at the opposite mode-converting phenomenon to Case 2. For an incident shear wave, the scattered wave field is manipulated to allow longitudinal wave reflection only at a target reflection angle of $\theta_{p,ref}^{+1} = 62°$, as depicted in Fig. 4.6(a). Using Eq. (4.6b) with the considered wave propagation properties, the periodicity of the unit cell was determined as $a_{Case3} = 50.91$ mm. Then, as shown in Fig. 4.6(b), six propagating diffraction modes (three longitudinal wave modes in the order of $n = 0,\ \pm 1$ and three shear waves in the order of $m = 0,\ \pm 1$) were predicted by Eqs. (4.3a) and (4.3b). With the same set of design variables as in Case 2, the five undesired scattered modes were suppressed by imposing them in the constraint equations of Eq. (4.10) as follows: $h_{-1}(\mathbf{v}) = \Pi_{P_{-1}}$, $h_0(\mathbf{v}) = \Pi_{P_0}$, $g_{-1}(\mathbf{v}) = \Pi_{S_{-1}}$, $g_0(\mathbf{v}) = \Pi_{S_0}$, and $g_{+1}(\mathbf{v}) = \Pi_{S_{+1}}$. The randomly generated initial values of the design variables are listed in Table 4.2 alongside the values obtained at the end of the optimization.

Figs. 4.6(c-e) shows the convergence history during optimization and the manipulated amplitudes of the six scattered modes in Case 3. As shown in the figures,

the amplitude of the target longitudinal wave mode ($\nabla \cdot \mathbf{u}$) for $n = +1$ became predominant, whereas those of the five other modes were reduced at the end of the optimization. The shear-to-longitudinal wave mode conversion from the unit cell was clearly observed in Fig. 4.6(f), with a mode-conversion efficiency of 96 %. In Fig. 4.6(f), the scattered shear wave field ($\left(\nabla \times \mathbf{u}\right)_z$) was slightly observable, because the undesired shear wave modes were not perfectly suppressed as shown in Fig. 4.6(e). This slight reduction in the mode-conversion efficiency in Case 3 was attributable to the large number of propagating diffraction modes. Nevertheless, converting 96 % of the incident power into the different type of reflected wave represents a remarkable performance for the proposed strip-type metagratings. The reflected longitudinal wave propagated in the target direction distinctively from the array of the designed unit cells, as shown in Fig. 4.6(g).

In the third design category (consisting of Cases 4 and 5), the proposed strip-type metagratings were designed to split a normally incident wave into two directions in different wave modes. As illustrated in Fig. 4.7(a), Case 4 was for designing the metagrating unit cell to split a normally incident longitudinal wave into both longitudinal and shear waves, each of which exhibits anomalous reflection angles of $\theta_{p,ref}^{+1} = 70°$ and $\theta_{s,ref}^{-1} = -33°$, respectively. On the other hand, in Case 5, the beam-splitting metagrating unit cell was designed under a normal shear wave incidence as shown in Fig. 4.8(a). The split beams in Case 5 propagated in the target directions of

$\theta^{0}_{p,ref} = 0°$ and $\theta^{+1}_{s,ref} = 50°$ as longitudinal and shear wave modes, respectively. Note that one target angle among the beam splitting angles could be selected arbitrarily, while the other angle depended on the selected angle. Because an identical unit cell with the same periodicity was considered, it was impossible to set two beam splitting angles independently according to the diffraction grating theory.

In the first beam-splitting metagrating design (Case 4), the periodicity of the unit cell was calculated as $a_{Case4} = 47.83$ mm by inserting $\theta^{+1}_{s,ref} = 33°$ into Eq. (4.6a). Owing to the symmetry between diffraction modes, the periodicity of the unit cell for $\theta^{+1}_{s,ref} = 33°$ matched that for the target angle of $\theta^{-1}_{s,ref} = -33°$ as discussed. Then, the reflection angle of the longitudinal wave mode is dependently decided as $\theta^{+1}_{p,ref} = 70°$ in Eq. (4.3a). The propagating diffraction modes in the scattered wave field were predicted using Eqs. (4.3a) and (4.3b) in three longitudinal wave ($n = 0,\ \pm 1$) and three shear wave ($m = 0,\ \pm 1$) modes as listed in Table 4.1. To split an incident longitudinal wave into 1st-order longitudinal ($n = +1$) and -1st-order shear ($m = -1$) wave modes as illustrated in Fig. 4.7(a), the remaining four modes were suppressed in the optimization.

In Case 5, for splitting an incident shear wave into both longitudinal wave reflection at the specular angle $\theta^{0}_{p,ref} = 0°$ and shear wave reflection at the target angle $\theta^{+1}_{s,ref} = 50°$, the periodicity of the unit cell was determined as $a_{Case5} = 33.96$ mm

with $\theta_{s,ref}^{+1} = 50°$. Because four diffraction modes (one longitudinal wave mode ($n = 0$) and three shear wave modes ($m = 0,\ \pm 1$)) can propagate in the scattered wave field, the two shear modes of $m = -1,\ 0$ were suppressed by considering them as the constraint equations in the optimization, to thereby enrich the 0th-order longitudinal and +1st-order shear wave modes as illustrated in Fig. 4.8(a).

The obtained values of the design variables for Cases 4 and 5 are presented in Table 4.2. First, it is notable in Figs. 4.7(a) and 4.8(a) that the configurations of the designed unit cells in Cases 4 and 5 were dissimilar to each other. Figs. 4.7(b) and 4.7(c) and Figs. 4.8(b) and 4.8(c) show the amplitudes of the scattered diffraction modes at the end of each optimization in Cases 4 and 5, respectively. In both cases, the multiple diffraction modes appearing at the initial stages were effectively suppressed such that the target modes became predominant at the end of the optimization. As shown in Figs. 4.7(d) and 4.8(d), respectively, normally incident longitudinal and shear waves were successfully split into both longitudinal and shear wave modes with target reflection angles. By evaluating the scattered wave fields shown in Fig. 4.7(d) for Case 4, it was found that 95 % of the incident longitudinal wave power was reflected in the two target modes: 24 % in the +1st-order longitudinal wave mode and 71 % in the -1st-order shear wave mode. In Case 5 shown in Fig. 4.8(b), the designed metagrating unit cell split 96.6 % of the incident shear wave power into the designated modes: 29.8 % and 66.8 % of the 0th-order longitudinal and +1st-order shear wave modes, respectively. As shown in Figs. 4.7(e)

and 4.7(f) and Figs. 4.8(e) and 4.8(f), respectively, the scattered longitudinal and shear waves from the multiply arranged metagrating unit cells propagate apparently in the target directions with $\theta_{p,ref}^{+1} = 70°$ and $\theta_{s,ref}^{-1} = -33°$ in Case 4, and $\theta_{p,ref}^{0} = 0°$ and $\theta_{s,ref}^{+1} = 50°$ in Case 5. It is observable that small quantities of wave power were spatially distributed across various directions in the scattered wave fields. These results arose from multiple constructive and/or destructive interactions of the undesired scattered modes; these corresponded to a small percentage of incident wave power that was not converted by the designed metagratings.

Alongside the three categories of metagrating designs, we produced an additional design for the metagrating unit cell (Case 6) to make it practically applicable for nondestructive evaluation (more specifically, non-invasive flow speed measurement; see e.g., [111]). Conventional wedges typically feature tapered shapes, whose sloped reflecting planes are flat and traction-free surfaces that ensure total internal reflection using critical angles. However, tapering is no longer required for mode conversion when using the present metagratings. Instead, the designed mode-converting strip-type metagratings are installed along the reflecting plane such that the incident longitudinal wave is precisely and efficiently converted into a shear wave at a target reflection angle. The resulting device is shown in Fig. 4.9(a) and referred to as a reflection-type mode converter.

Rectangular blocks with a metagrating plane were attached to the upper and lower

surfaces of a thick aluminum plate. When a longitudinal wave excited by the transducer (PZT) impinged on the metagrating plane of the rectangular block on the upper surface of the plate, the incident longitudinal wave was converted into an inclined shear wave, as illustrated in Fig. 4.9(a). The propagating shear wave through the aluminum plate (indicated by the blue arrows) was obliquely incident to another rectangular block on the lower surface of the plate. The obliquely incident shear wave was then reconverted into a longitudinal wave, which reached the measuring transducer in the normal direction. The reciprocity characteristics of the elastic wave propagation meant that identical metagrating planes were implemented in the rectangular blocks on the upper and lower surfaces of the plate.

Considering the practical working conditions of the conventional wedges used in nondestructive testing [111], the wave propagating frequency was set to 440 kHz ($c_p = 6{,}198$ m/s , $c_s = 3{,}122$ m/s , and $\lambda_p = 0.014$ m , $\lambda_s = 0.007$ m), and the target reflection angle was selected as $\theta_{s,ref}^{+1} = 55°$. The required periodicity of the metagrating unit cell was calculated as $a_{Case6} = 8.70$ mm in Eq. (4.6a). As listed in Table 4.1 (Case 6), four propagating diffraction modes were predicted in the scattered wave field using Eqs. (4.3a) and (4.3b). By solving the optimization problem in Eq. (4.9) and Eq. (4.10), the metagrating unit cell was designed to allow 1st-order shear wave propagation only in the target reflection angle.

Figure 4.9(b) shows the configuration of the designed unit cell for the metagrating plane. The initial and optimized values of the design variables are listed in Table 4.2.

Based on the scattered field obtained from the periodic unit cell, the longitudinal-to-shear wave-mode conversion efficiency was found to reach 99 %. To verify the validity of the present reflection-type mode-converter design, the conceptual environment in Fig. 4.9(a) was numerically modeled with plane strain condition. In Figs. 4.9(c) and 4.9(d), the reflection-type mode converter made of aluminum was modeled with dimensions of $80\ \mathrm{mm} \times 100\ \mathrm{mm}$ (width $\times$ height) and a thickness of $80\ \mathrm{mm}$. In each mode converter, 12 designed metagrating unit cells were installed on a reflecting plane as shown in the figures. The transducers were modeled as 70 mm-wide, 4.5 mm-thick piezoelectric ones made of a PTZ-4 (Lead-Zirconate-Titanate) compound. As shown in Figs. 4.9(c) and 4.9(d), the reflection-type mode converters exhibited excellent performances in the practical environment. The incident longitudinal wave from the exciting transducer and the longitudinal wave reflected to the measuring transducer are clearly shown in Fig. 4.9(c), whereas no longitudinal wave mode was observable in the aluminum plate. In contrast, the mode-converted shear wave from the upper mode converter obliquely propagated through the aluminum plate and reached the lower mode converter, as shown in Fig. 4.9(d). The designed reflection-type mode converters were directly applicable for nondestructive testing, achieving remarkably high efficiencies in mode conversion and anomalous steering simultaneously.

4.5 Analysis of the phenomenon

4.5.1 Experimental verification

Among the present mode-converting and wave-steering metagrating designs, the beam-splitting metagrating structure in Case 4 was manufactured for an experimental performance evaluation. The designed metagratings shown in Fig. 4.7 split a normally incident longitudinal wave into both longitudinal and shear waves with anomalous reflection angles of $\theta_{p,ref}^{+1} = 70°$ and $\theta_{s,ref}^{-1} = -33°$, respectively. Fig. 4.10(a) shows the experimental setup; here, the beam-splitting metagrating array was fabricated along the boundary of a 1 mm-thick aluminum alloy plate (A5052) by laser precision cutting. The metagrating array in the plate consisted of 12 unit cells whose geometrical dimensions matched those designed in Case 4; these cells were protected by an outer frame with a width of $50\ \mathrm{mm}$. The other boundaries of the plate were attached to Blu Tack layers to reduce the effect of reflected waves.

As shown in Fig. 4.10(a), a magnetostrictive patch transducer (MPT) [104] was employed as a line transmitter to actuate the lowest symmetric Lamb wave (S_0), which can be considered as an in-plane longitudinal wave in the plate, with a frequency of 120 kHz. The line source signal (30 cycles of a sinusoidal wave) was generated in a function generator (Agilent 33220A) and amplified using a power amplifier (AG 1017L) before application to the MPT. A 0.1 mm-thick nickel patch ($400\ \mathrm{mm} \times 22.5\ \mathrm{mm}$) was used as the magnetostrictive element in the MPT that was installed 300 mm away from the metagrating array, as shown in Fig. 4.10(a).

The scattered longitudinal and shear waves from the metagrating array were measured using an electromagnetic acoustic transducer (EMAT) and other MPT, respectively, along a semicircle of radius 500 mm. The scattered longitudinal waves were measured at 21 points on the semicircle ($10°$ intervals in the range $-80° \sim 50°$ and $5°$ intervals in the range $55° \sim 85°$), while the measurements of the scattered shear waves were conducted at 24 points ($-80°$, $-70°$, $5°$ intervals in the range $-65° \sim -10°, -33°$, and $10°$ intervals in the range $0° \sim 80°$). At every measurement point, the signals were averaged over four-times measurements.

As the result of experiments, Figs. 4.10(b) and 4.10(c) show the normalized power amplitudes of the scattered longitudinal and shear waves obtained from the beam-splitting metagrating array, respectively. It is clearly observed that the scattered longitudinal and shear waves propagate predominantly in the directions of the target reflection angles, $\theta_{p,ref}^{+1} = 70°$ and $\theta_{s,ref}^{-1} = -33°$. Furthermore, the experimental results agree well with the numerical results, which were calculated from a model that duplicated the experimental configuration. Although small differences between the experimental and numerical results were observable, these may be caused by the fabrication procedure of the metagrating array. The present experimental results validate the performance of the proposed strip-type metagratings for mode conversion and wave steering. For further experimental verification of the performance of the elastic metagrating, the beam-split powers to the longitudinal and shear waves in Figs. 4.10(b,c) are compared with powers of reflected waves from a

traction-free boundary (i.e., without elastic metagrating treatment) in Fig. 4.11.

Fig. 4.11 compares the split power amplitudes of the longitudinal and shear waves from the beam-splitting metagrating shown in Fig. 4.10 with the powers of reflected both waves from a traction-free boundary (i.e., without the metagrating). In Fig. 4.11(a), the scattered longitudinal wave powers are normalized by the maximum value of the longitudinal wave power reflected from a traction-free boundary case. On the other hand, the scattered shear wave powers in Fig. 4.11(b) are normalized by the maximum value of the shear wave power from the present metagrating shown in Fig. 4.10. As shown in Fig. 4.11(a), the power of scattered longitudinal wave is concentrated in the middle which is straight from the source line at the traction-free boundary, while reflected power of the longitudinal wave is measured in the direction of the target reflection angle $\theta_{p,ref}^{+1} = 70°$. By neglecting any kind of dissipation and loss of wave power, the longitudinal wave power from the traction-free boundary case can be assumed to be the same with the total incident longitudinal power. This assumption is reasonable because the normally incident longitudinal wave to the traction-free boundary reflects almost all of the power in normal direction. Then, by integrating the area of the power graphs in Fig. 4.11(a), we can estimate the power conversion ratio indirectly. The power of the scattered longitudinal wave is calculated to be 25.18 %, and it is consistent with the result in the simulation of 24 %. In a similar manner, Fig. 4.11(b) results in nearly 75 % of the incident wave power (which is calculated from Fig. 4.11(a)) is converted to the shear wave from the metagrating.

4.5.2 Physical interpretation

In this part, we physically analyzed the phenomenon of mode-converting reflection using the surface impedance concept. In former research, it is thought to be difficult to fully understand the entire physics inside the elastic metagratings. The cause of such hardness stems from the unique characteristics of the scatterers. Each scatterer inside the unit cell of metagratings interact with each other and coupling of scatterers form complex phenomena. In earlier researches on metagratings, the physics of metagratings are usually explained in verbal form using the diffraction grating theory. Many of the works used the explanation as follows: the diffraction modes are controlled by the metagratings and modes except the target modes cancel out by the destructive interferences of waves. In the perspective of the diffraction grating theory, this explanation is true, but it is hard to analyze how the scatterers in metagratings actually cancel out undesignated modes. It is also difficult to apply the phase-modulation method as in **Chapter 3**, because it can only explain the wave steering phenomena, not the mode-conversion. In addition, when the wave field of metagratings are observed, the diverse coupling phenomena can be found between these members. In this circumstances, we will use the concept of surface impedance. The surface impedance is originally used in the electromagnetic [112] or acoustic wave [77] to explain the wave phenomena in the certain line or the boundary. With using this concept, we can easily interpret the entire metagrating unit cell at once. It means that the coupling effect of structures can be take into account.

To begin with, we should define the surface impedance in the elastic medium. As an

analogy to the surface impedance of acoustic waves, we can consider the straight line A-A' which is normally depart from the metagrating structures as in Fig. 4.12(a) and Fig. 4.13(a). In acoustics, the pressure and velocity along the line are defined as function of position. However, the stresses extracted from certain line has two components including normal and shear stresses. Therefore, we should define the surface impedance in the form of matrix as:

$$\begin{Bmatrix} \sigma_{xx} \\ \sigma_{xy} \end{Bmatrix} = \begin{bmatrix} Z_{11} & Z_{12} \\ Z_{21} & Z_{22} \end{bmatrix} \begin{Bmatrix} v_x \\ v_y \end{Bmatrix}, \tag{4.13}$$

where σ_{xx}, σ_{xy} denote the normal and shear stress along the line A-A', Z_{ij} $(i, j = 1, 2)$ denotes the components of the surface impedance matrix at the line A-A', and v_x, v_y denote the x, y component of the velocity vector. Since we are analyzing the passive and lossless system, each component of the surface impedance matrix is calculated to be imaginary.

Our approach using the surface impedance matrix is that for any wave steering phenomena there should be a certain wave field that can realize such phenomena. It means that if we design the structures that enable to realize certain wave field, then we can also realize any wave steering phenomena. For explanation, we revisit the mode-converting specular and anomalous reflection.

Firstly, the mode-converting specular reflection in Fig. 4.4 is analyzed through surface impedance approach. For realizing the mode-converting specular reflection, the potential functions should be defined as follows:

$$\varphi^{inc} = A_0 e^{-jk_p x}, \quad \psi^{scat} = B_0 e^{jk_s x}, \tag{4.14a,b}$$

where A_0, B_0 denote the amplitude of longitudinal and shear wave potential function, respectively. If longitudinal wave is fully converted to shear wave, the ratio of the wave amplitude can be calculated using the power conservation law as:

$$\left|\frac{B_0}{A_0}\right| = \sqrt{\frac{c_s}{c_p}}. \tag{4.15}$$

In Eq. (4.15), the ratio of the wave amplitude is calculated to be 0.76 in aluminum medium. Using this value, we can easily calculate the displacement, velocity, and stress field. And utilize the condition that the surface impedance matrix is imaginary, we can calculate the surface impedance matrix at line A-A' which is at the position of $x = h$ as in Fig. 4.12. Since the value of h can be arbitrarily chosen, we used the value of $h = -0.06$ m. It should be noted that the h value should be larger than the wavelength of longitudinal or shear wave, since we only consider the far-field diffraction mode of elastic waves.

We compare the results of surface impedance matrix between the theoretical and numerical values from Fig. 4.12(b) to Fig. 4.12(e). In each graphs, the imaginary part of the surface impedance matrix component is compared. For the numerical values, we extracted the stress and velocity field in the line A-A' and calculate the surface impedance components. The result shows that theoretical and numerical values are in excellent coincidence. Therefore, we can conclude that proposed metagrating forms the wave field which can realize the mode-converting specular reflection.

Secondly, the mode-converting anomalous reflection in Fig. 4.5 is analyzed through same approach. For realizing the mode-converting anomalous reflection, the potential functions should be defined as follows:

$$\varphi^{inc} = A_0 e^{-jk_p x}, \quad \psi^{scat} = B_0 e^{j(k_{sx}x - k_{sy}y)}. \tag{4.16a,b}$$

If longitudinal wave is fully converted to shear wave with the target angle, the ratio of the wave amplitude can be calculated using the power conservation law as:

$$\left|\frac{B_0}{A_0}\right| = \sqrt{\frac{c_s}{c_p \cos\theta_{s,ref}}}. \tag{4.17}$$

In Eq. (4.17), the ratio of the wave amplitude is calculated to be 0.90 in aluminum medium. For the arbitrary position *h*, we used the value of $h = -0.06$ m as in Fig. 4.13.

We compare the results of surface impedance matrix between the theoretical and numerical values from Fig. 4.13(b) to Fig. 4.13(e). In each graphs, the imaginary part of the surface impedance matrix component is compared. For the numerical values, we extracted the stress and velocity field in the line A-A' and calculate the surface impedance components. The result shows that theoretical and numerical values are in excellent coincidence. Therefore, we can conclude that proposed metagrating forms the wave field which can realize the mode-converting specular reflection.

The surface impedance method can interpret the whole unit cell at once. However, it has a limitation. That is, the surface impedance doesn't explain the wave controlling

phenomena by the metagratings with respect to the structure. For further studies, we need to evaluate the coupling effects induced by the interaction between nearby scatterers. But, our attempt to adopt the idea of analyzing entire unit cell at once is important and it is expected the additional physical interpretation on the metagratings using the coupling effects will be studied in the near future.

For qualitative description of mode-converting reflection, some observation can be useful. In Appendix B in this dissertation, transient analysis and simulation result is presented. When 30 cycles of longitudinal waves normally incident to the metagrating structure, the mode-converting reflection phenomenon needs additional time to be realized. It means that after additional time, the phenomenon becomes a steady-state and condition becomes similar to the harmonic analysis. In the respect of structure, the surface wave is formed in the edge of the structure after the additional time. During the formation of surface wave, longitudinal and shear wave in the elastic medium are coupled due to the complex motions of metagrating structures. Inside the scatterers (or strip-type members) show complex motion including longitudinal, shear, and flexural motion and these complex motions seem to create coupling of elastic waves.

Such metagratings can also be explained using the concept of reciprocal lattice. One-dimensional lattice space which is a metagrating structure space with a periodicity can be transformed to the reciprocal space (or *k*-space) by the Fourier transform in spatial domain. Such relation between the wavenumber and reciprocal lattice is actually a diffraction grating equation. In definition, reciprocal lattice is identical to

diffraction term. We can also explain that complex motion of strip-type members coupled the elastic waves and affects wave amplitudes determined in reciprocal lattice. However, it still needs quantitative approach and we hope such additional interpretation can be possible.

4.6 Concluding remarks

We showed that near-perfect mode conversion and wave steering can be simultaneously achieved if elaborately designed metagratings are attached to the free boundary of an elastic plate. In contrast to common metasurfaces based on phase gradients, the designed metagratings can satisfy the two objectives simultaneously because the wave phenomena realized with metagratings are governed by the diffraction grating theory and our metagratings have sufficient design degrees of freedom to accommodate the desired wave manipulations. Specifically, a normally incident longitudinal wave upon the traction-free boundary of an elastic plate was converted by the designed metagratings into a reflected shear wave at the specified oblique angle with other higher-order modes nearly suppressed; in terms of energy, the mode-conversion reflection efficiency was nearly perfect, reaching 96 %. Similar near-perfect wave mode conversions were accomplished in all other cases of wave manipulation (e.g., beam splitting) in this work. The numerical results were supported by the experimental results. We demonstrated a practically useful application of the proposed metagratings via the new type of perfect mode-converting device as well. The reflection-type mode converter equipped with the designed metagratings was found to represent a new method to achieve full mode conversion and wave steering. Although this work focused upon a single harmonic wave, the extension of this work to tackle pulses is expected to pave the way towards improving the practicality of the proposed metagrating-based elastic wave manipulation.

Table 4.1 Number of diffraction modes considered in the metagrating designs.

	Mode	Case 1	Case 2	Case 3	Case 4	Case 5	Case 6
Number of diffraction modes	Longitudinal wave mode	1	1	3	3	1	1
	Shear wave mode	1	3	3	3	3	3

Table 4.2 Initial and optimized values of the design variables in the design optimization. (Initial values were randomly generated)

Case	Design variables	State	Values (mm)
1	$\{r_{12}, L_1, L_2, w_1, w_2\}^T$	Initial	$\{12.36, 5.95, 13.31, 5.46, 5.97\}^T$
		Optimized	$\{14.14, 7.03, 9.25, 5.05, 5.10\}^T$
2	$\{r_{12}, r_{23}, L_1, L_2, L_3, w_1, w_2, w_3\}^T$	Initial	$\{5.94, 16.20, 15.67, 31.96, 7.18, 4.69, 3.04, 2.90\}^T$
		Optimized	$\{7.10, 19.52, 10.50, 31.76, 6.13, 3.06, 2.93, 6.17\}^T$
3	$\{r_{12}, r_{23}, L_1, L_2, L_3, w_1, w_2, w_3\}^T$	Initial	$\{18.15, 18.95, 17.69, 17.63, 12.48, 13.60, 6.17, 2.56\}^T$
		Optimized	$\{12.16, 19.21, 12.34, 8.62, 12.61, 14.96, 1.00, 1.76\}^T$
4	$\{r_{12}, r_{23}, L_1, L_2, L_3, w_1, w_2, w_3\}^T$	Initial	$\{22.53, 14.58, 31.97, 23.78, 9.14, 8.27, 7.73, 5.63\}^T$
		Optimized	$\{17.84, 21.92, 27.97, 22.98, 7.68, 5.01, 6.79, 6.12\}^T$
5	$\{r_{12}, r_{23}, L_1, L_2, L_3, w_1, w_2, w_3\}^T$	Initial	$\{11.75, 9.59, 13.86, 24.20, 31.55, 7.10, 9.80, 6.13\}^T$
		Optimized	$\{15.29, 9.63, 9.42, 22.20, 33.38, 5.07, 9.02, 5.02\}^T$
6	$\{r_{12}, r_{23}, L_1, L_2, L_3, w_1, w_2, w_3\}^T$	Initial	$\{3.10, 3.16, 5.76, 8.05, 5.13, 1.40, 1.38, 1.82\}^T$
		Optimized	$\{2.40, 3.60, 5.98, 7.85, 3.10, 1.51, 1.49, 1.44\}^T$

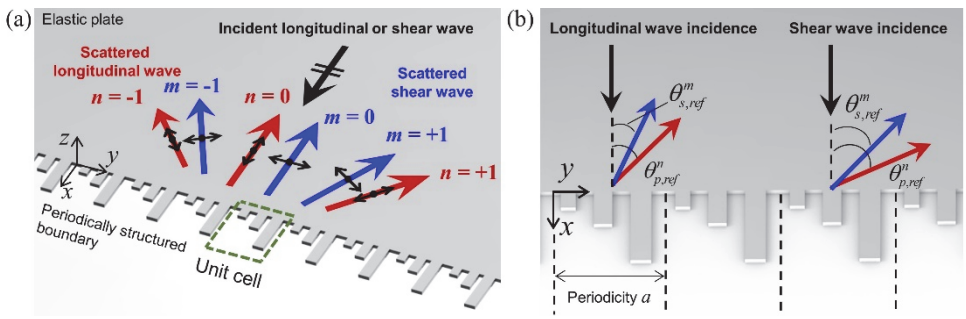

Fig. 4.1 Conceptual illustrations of the multiply scattered diffraction modes and targeting mode-converting phenomena in this chapter. (a) Multiply scattered longitudinal and shear wave modes from a periodically structured boundary. (b) mode conversion and wave steering realized by the metagratings.

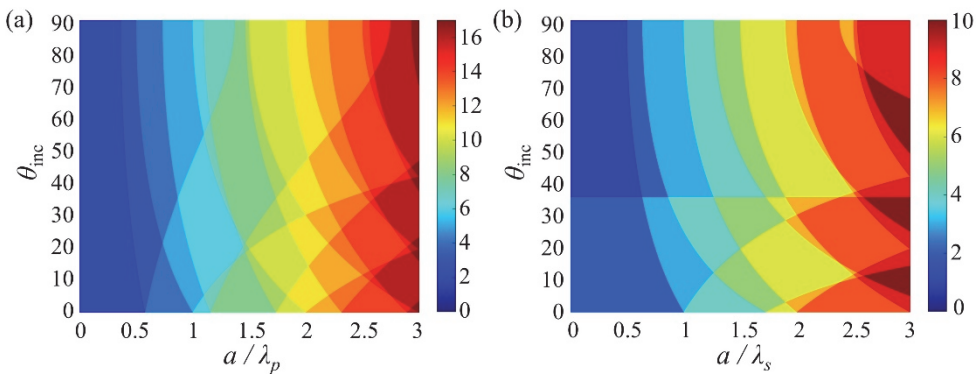

Fig. 4.2 Theoretical number of propagating diffraction modes in the scattered wave field with respect to the normalized periodicity of the unit cell and the incident angle. (a) Longitudinal wave incidence, (b) shear wave incidence.

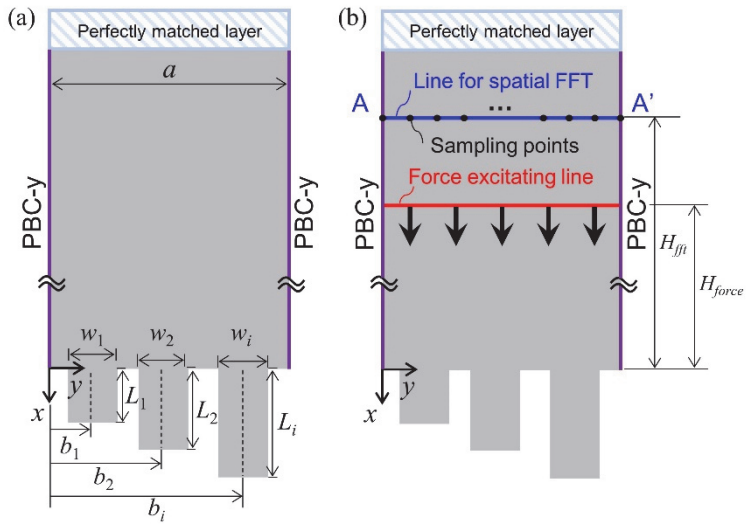

Fig. 4.3 Configuration of the periodic unit cell of the proposed strip-type metagratings with boundary conditions for numerical analysis and evaluation. (a) Geometrical dimensions of rectangular strip members in the infinitely periodic unit cell, (b) boundary conditions together with the lines for force exitation and spatial FFT.

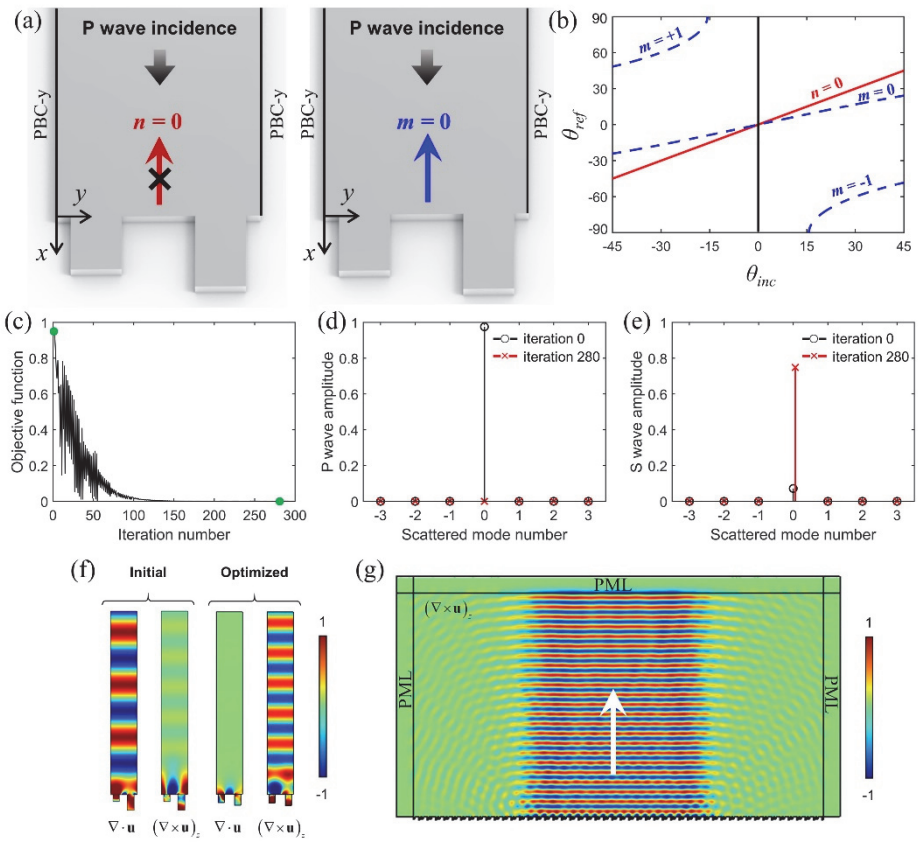

Fig. 4.4 Problem definition and results of Case 1 for longitudinal-to-shear wave mode conversion with a specular angle of $\theta^0_{s,ref} = 0°$. (a) Illustration of the reflected and suppressed diffraction modes, (b) number of propagating diffraction modes, (c) convergence history during optimization, (d,e) comparison of the scattered diffraction modes of longitudinal and shear waves, respectively, before and after optimization, (f) comparison of the scattered wave fields from the initial and designed unit cells, (g) scattered shear wave field from the multiply arranged unit cells.

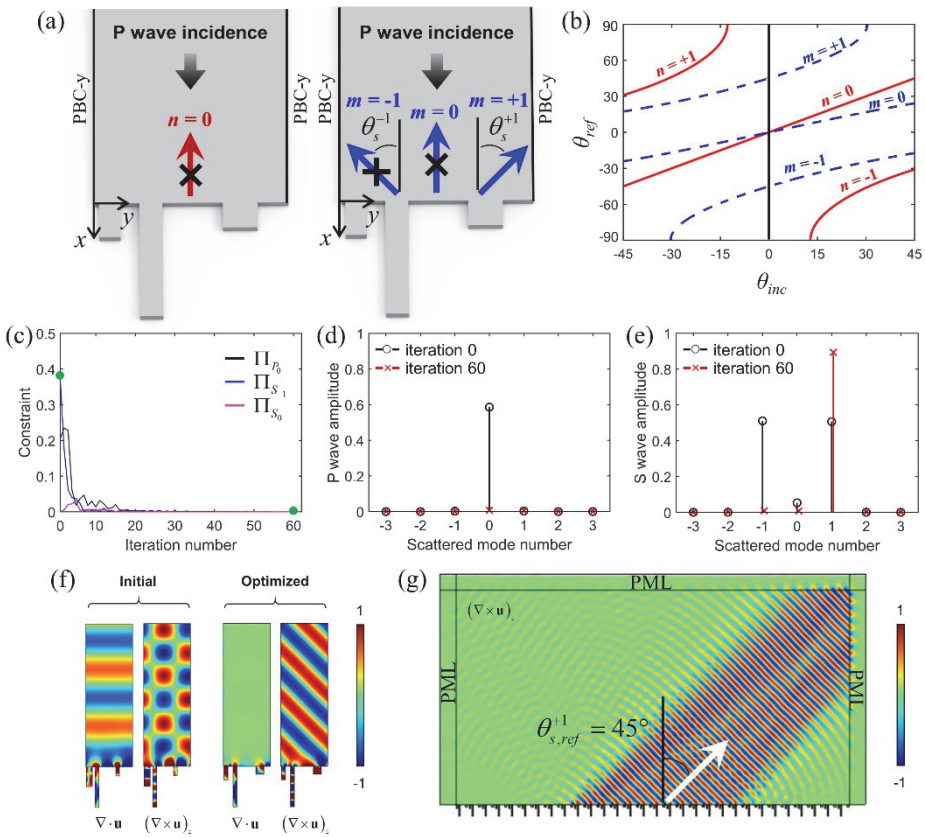

Fig. 4.5 Problem definition and results of Case 2 for longitudinal-to-shear wave mode conversion with a target reflection angle of $\theta_{s,ref}^{+1} = 45°$. (a) Illustration of the reflected and suppressed diffraction modes, (b) number of propagating diffraction modes, (c) convergence history during optimization, (d,e) comparison of the scattered diffraction modes of longitudinal and shear waves, respectively, before and after optimization, (f) comparison of the scattered wave fields from the initial and designed unit cells, (g) scattered shear wave field from the multiply arranged unit cells.

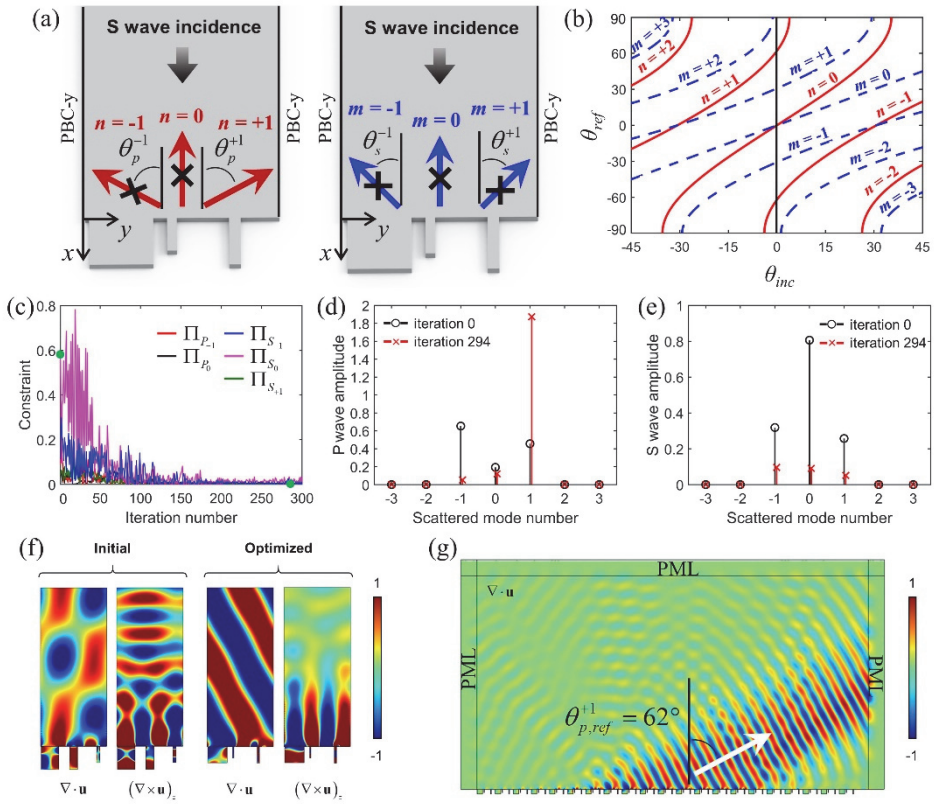

Fig. 4.6 Problem definition and results of Case 3 for shear-to-longitudinal wave mode conversion with a target reflection angle of $\theta_{p,ref}^{+1} = 62°$. Note that the unit cells were already configured with the designed geometrical dimensions. (a) Illustrations of the reflected and suppressed diffraction modes, (b) number of propagating diffraction modes, (c) convergence history during optimization, (d,e) comparison of the scattered diffraction modes of longitudinal and shear waves, respectively, before and after optimization, (f) comparison of the scattered wave fields from the initial and designed unit cells, (g) scattered longitudinal wave field from the multiply arranged unit cells.

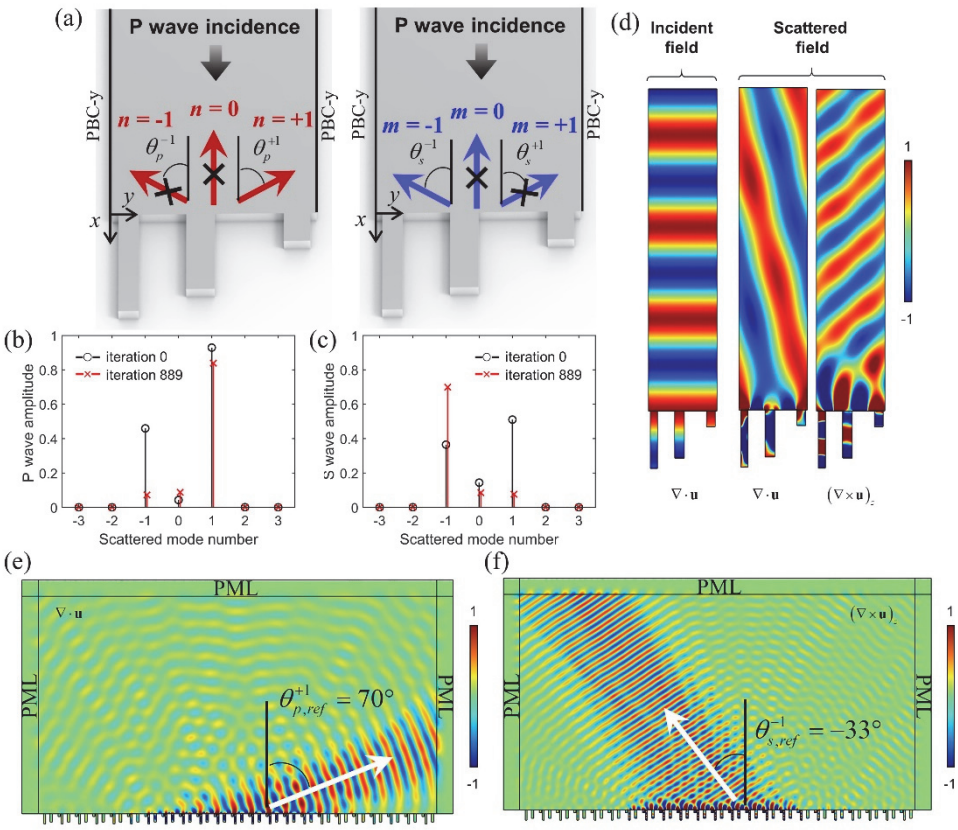

Fig. 4.7 Problem definition and results of Case 4 for splitting an incident longitudinal wave into both longitudinal and shear waves with reflection angles of $\theta_{p,ref}^{+1} = 70°$ and $\theta_{s,ref}^{-1} = -33°$, respectively. (a) Illustration of the reflected and suppressed diffraction modes, (b,c) comparison of the scattered diffraction modes of longitudinal and shear waves, respectively, before and after optimization, (d) comparison of the incident and scattered wave field from the designed beam-splitting metagrating unit cell, (e,f) scattered longitudinal and shear wave fields from the multiply arranged beam-splitting metagrating unit cells, respectively.

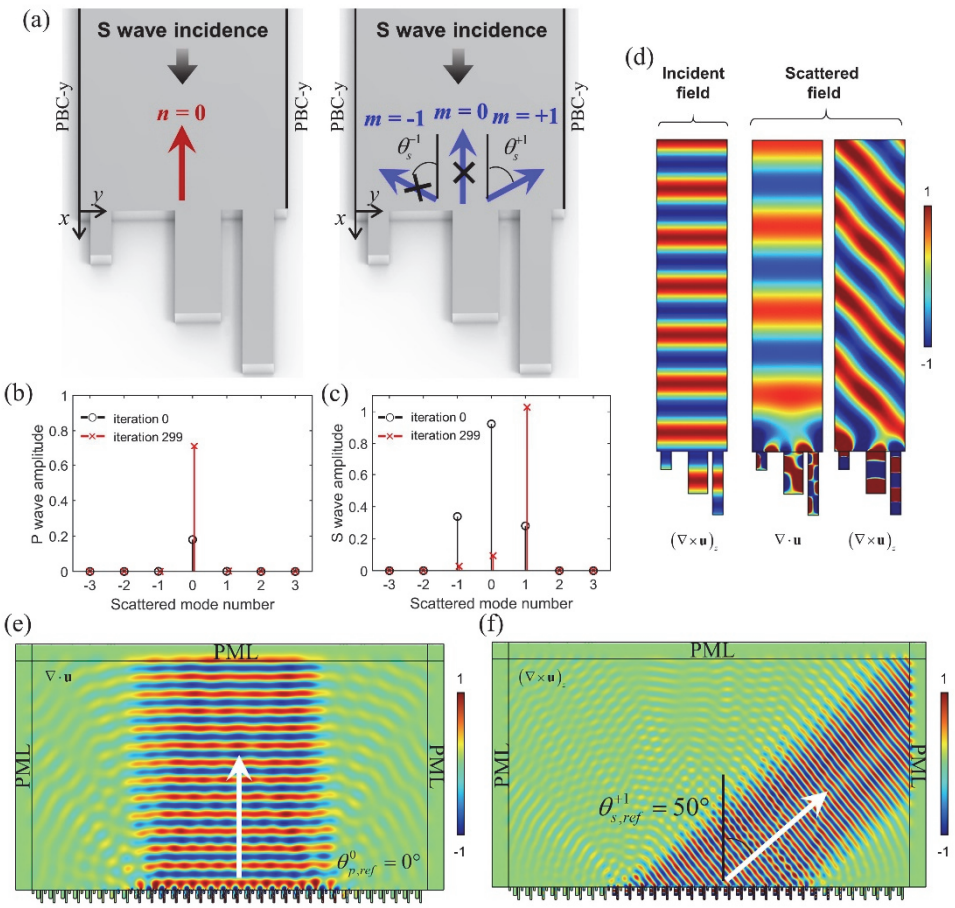

Fig. 4.8 Problem definition and results of Case 5 for splitting an incident shear wave into both longitudinal and shear waves with reflection angles of $\theta^{0}_{p,ref} = 0°$ and $\theta^{+1}_{s,ref} = 50°$, respectively. Note that the unit cells were already configured with the designed geometrical dimensions. (a) Illustration of the reflected and suppressed diffraction modes, (b,c) comparison of the scattered diffraction modes of longitudinal and shear waves, respectively, before and after optimization, (d) comparison of the incident and scattered wave fields from the designed beam-splitting metagrating unit cell, (e,f) scattered longitudinal and shear wave fields from the multiply arranged beam-splitting metagrating unit cells, respectively.

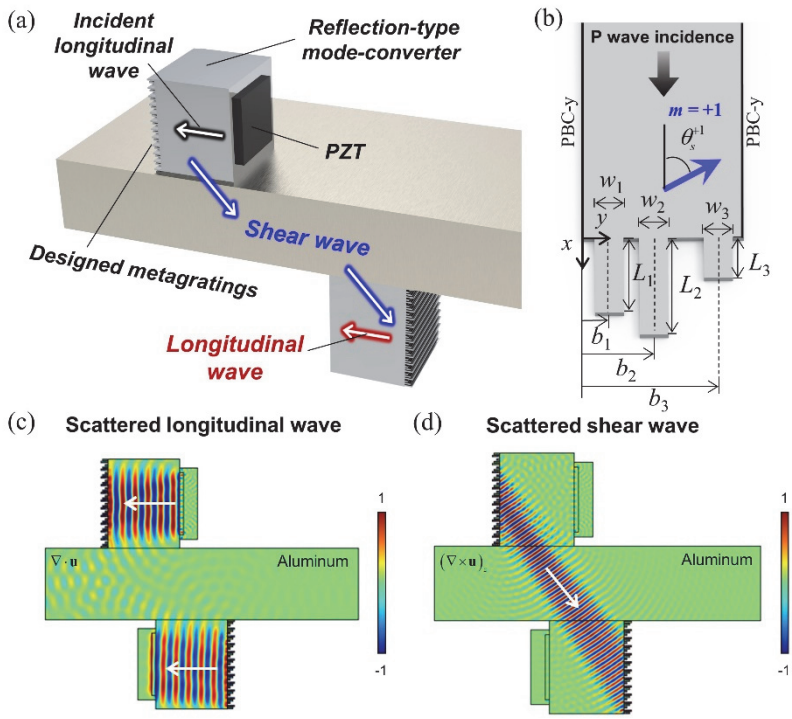

Fig. 4.9 Application of the proposed metagratings (Case 6): reflection-type mode converter for nondestructive evaluation. (a) Problem definition with two rectangular blocks on which the metagrating plane is attached, (b) Illustration of the targeting diffraction shear mode, (c) incident longitudinal wave field to and scattered longitudinal wave field from the designed metagrating plane, (d) scattered shear wave propagation through the thick aluminum plate.

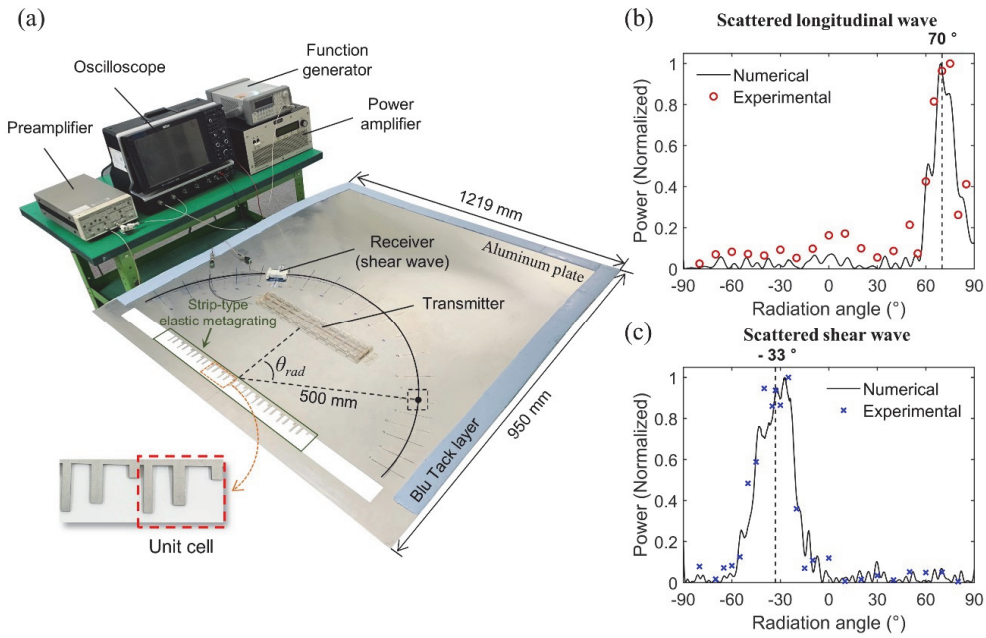

Fig. 4.10 Experimental setup and measurement data for verifying the beam-splitting metagratings designed in Case 4 (as shown in Fig. 4.7). (a) Experimental setup with the manufactured beam-splitting metagrating array in the 1-mm thick aluminum alloy plate, (b,c) comparison of the experimental and numerical results for beam splitting to (b) longitudinal wave reflection with a target angle of $\theta_{p,ref}^{+1} = 70°$, (c) shear wave reflection with a target angle of $\theta_{s,ref}^{-1} = -33°$.

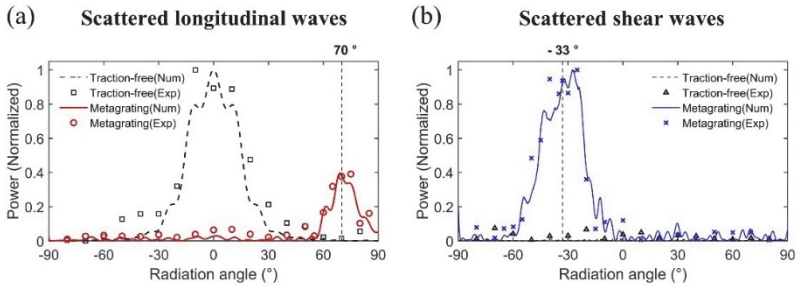

Fig. 4.11 Experimental measurements and numerical simulations for the beam-splitting metagratings including comparison of the traction-free boundary and metagrating. (a) The power of scattered longitudinal and (b) shear wave fields.

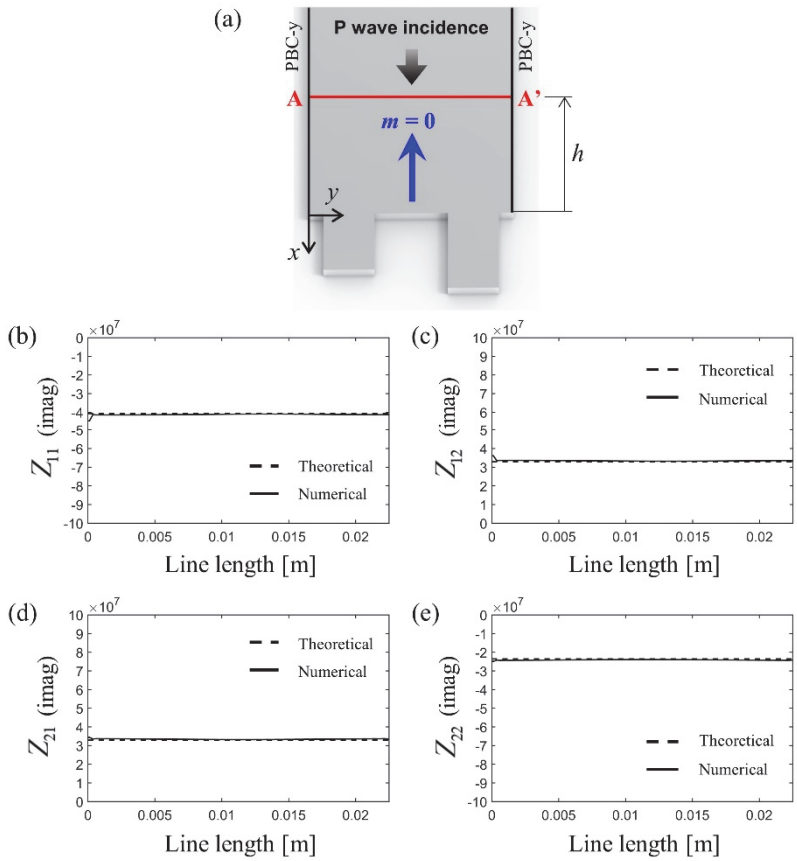

Fig. 4.12 The surface impedance analysis for the mode-converting specular reflection. (a) The line A-A' where the stress and velocity data for surface impedance calculation are extracted, (b-e) the components of surface impedance with respect to the unit cell line length.

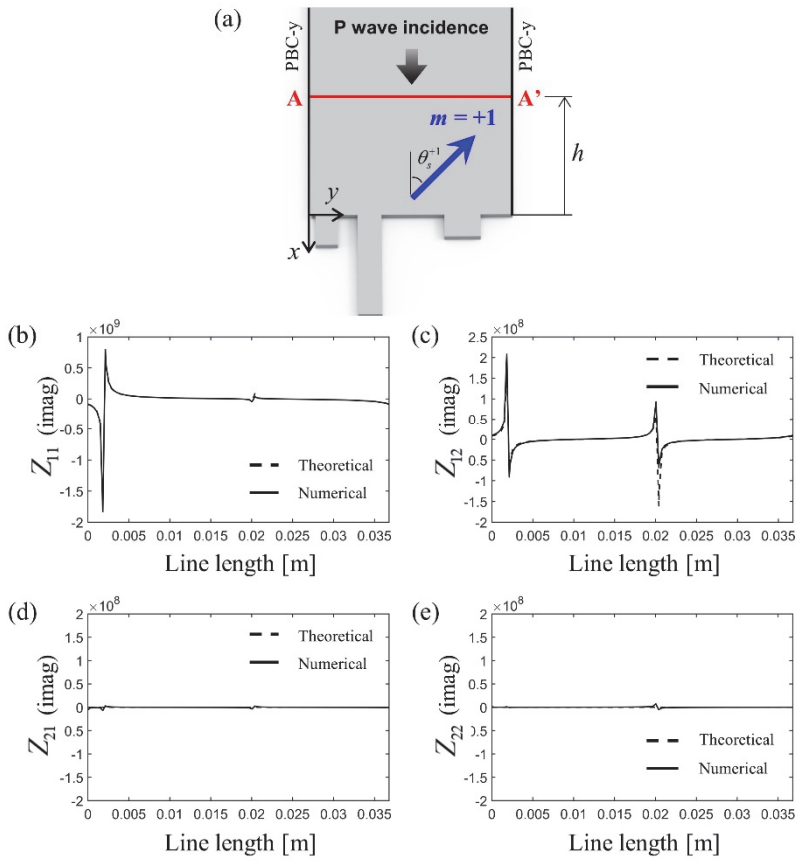

Fig. 4.13 The surface impedance analysis for the mode-converting anomalous reflection. (a) The line A-A' where the stress and velocity data for surface impedance calculation are extracted, (b-e) the components of surface impedance with respect to the unit cell line length.

CHAPTER 5.
Conclusions

In this dissertation, the reflective metagratings which can steer and/or convert the modes of the elastic waves were newly presented. For our research on metagratings, systematic studies followed by theoretical analysis based on the diffraction grating theory, numerical simulation using the finite element method, and experimental verification were implemented. The objective of the dissertation was challenging, because of the complex polarization and dispersive properties of the elastic waves. However, using the concept of metamaterials and the diffraction grating theory, newly presented metagratings can solve such difficult problems. In the thesis, we first control only the longitudinal wave using the beam-type metagratings. Then, the mode conversion between longitudinal and shear waves along with the wave steering is solved using the strip-type metagratings. We used either analytical or numerical methods for problem-solving. We will present the detailed investigation and conclusions of this dissertation as follows.

First, systematic research on metagratings for in-plane elastic waves with two steps was implemented carefully. Since there are few research works in the field of elastic metagratings, the way for approaching the problem was crucial. As a golden rule, we

first simplify the problems which can only control the longitudinal waves. And simple structures (beam-type members) were selected as scatterers that can be analytically modeled. With simplified problems and simple structures, it was easier to solve the problem and find the physics inside the metagratings. However, due to less degree of freedom in the design process, beam-type members were not enough for realizing more complex phenomena. Therefore, strip-type continuum members which are the general version of such scatterers were introduced. Finally, several mode-converting reflection phenomena are realized and verified. In short, this thesis first presented and organized the concept of reflective metagratings for the in-plane elastic waves. In addition, systematic methods of designing efficient metagratings for anomalous mode-converting reflection are studied deeply.

Next, the physics inside the wave phenomena is analyzed using the concept of phase modulation and surface impedance. The physics of metagratings is usually explained using the diffraction grating theory in various metagrating studies. In these works, the usual explanation is as follows: the diffraction modes are controlled by the metagratings and modes except the target modes cancel out by the destructive interferences of waves. Such an explanation in verbal form is not enough for understanding the inherent physics of metagratings. Therefore, we tried to explain physics using two different concepts. Using the phase modulation concept, we can conclude that metagratings can be interpreted as the phase-gradient metasurface. It is surprising that even though we never adopt the phase modulation concept for the design process, the metagratings were optimized with this concept and the

mechanism is thought to be identical to the phase-gradient metasurfaces in other research. However, when interpreting phenomena other than wave steerings such as mode-converting reflections, the situation becomes more complex. It is difficult to interpret using the phase-modulation concept because it can only explain the steering of each longitudinal or shear wave. In addition, when observing the wave field of these metagratings, we can see the diverse coupling phenomena between members. Therefore, the concept of interpreting the whole unit cell should be used and one of these concepts is the surface impedance method. Since there are few methods for analytical interpretation of the coupling of structures, the method for analyzing the entire unit cell at once is important in metagratings. This method tells us that when realizing high-efficiency wave phenomena such as the mode-converting reflection, certain wave fields including stress and velocity field should be formed. Such surface impedance method has a limitation. That is, the surface impedance doesn't explain the wave-controlling performance of metagrating with respect to the structure. However, the attempt to adopt the concept of analyzing an entire unit cell at once is important and we hope that additional physics on the metagratings will be found in the near future.

Finally, we presented the applications using the reflective elastic metagratings. Such applications can be applied in the field of structural health monitoring and ultrasonic nondestructive testing. In particular, we verified that the mode-converter with a metagrating array in the side wall can actually convert the longitudinal into the shear wave (or the shear wave into the longitudinal wave) and steer the wave into the

designated direction. It is expected that the proposed methods of designing elastic metagratings and such output structures can pave the way in the field of metagratings. Metagratings in an elastic medium still has a variety of problems using other types of elastic waves such as flexural wave, guided waves, torsional waves, etc. Also, we hope that our approach can be applied in practical applications in the industrial fields. Such application examples are non-destructive structural health monitoring, flow speed measurement, and medical ultrasonic applications (i.e., medical imaging, HIFU, etc.). Recently, active metamaterials are drawn attention for their possibility of controlling the material properties with an electrical signal [114]. Therefore, metagratings with active components can also be applied in the industrial field.

APPENDIX A.
Different optimized solutions for mode-converting reflection

Since the gradient-based optimizer employed in this work is searching for local optima during the optimization process, different optimized solutions with high performances can be found. Fig. A1 shows the scattered wave fields from the designed unit cells which have same performance as in Cases 1 and 2 of chapter 4. Compared with the unit cells shown in Figs. 4.4-4.5, those shown in Fig. A1 are designed to be dissimilar configurations due to the different initial values at the start of the optimization. Nevertheless, the designed unit cells shown in Fig. A1 realize the target mode conversion and wave steering successfully with the same levels of the mode conversion efficiency in each of the cases: 99% for Cases 1 and 2. This implies that the proposed optimization formulation in this work is effective to search for appropriate geometrical dimensions in the strip-type metagratings to realize the mode conversion and anomalous wave steering of elastic waves in the scattered reflection field.

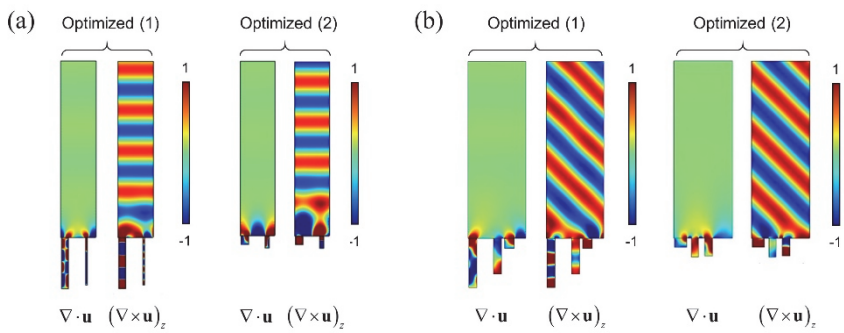

Fig. A.1 The scattered wave fields from the designed metagrating unit cells with different optimized values in Cases 1 and 2 in chapter 4. (a) Case 1: the longitudinal-to-shear wave mode conversion with the specular reflection, (b) Case 2: the longitudinal-to-shear wave mode conversion with the reflection angle of $\theta_{s,ref}^{+1} = 45°$.

APPENDIX B.
Transient simulation result and performance

Proposed mode-converting metagratings are also verified using the transient analysis done by the numerical simulation. In this thesis, we will present the result of mode-converting anomalous reflection with the reflection angle of $\theta_{s,ref}^{+1} = 45°$ in chapter 4 (Case 2). Compared to harmonic simulation, we used 30 cycles of sinusoidal longitudinal wave as a normally incident wave which can checked in Fig. B1. In Fig. B1(a), a normally incident longitudinal wave is impinged to the surface of metagrating boundary at the early part of the transient simulation ($86\,\mu s$). In the reflected field, however, both longitudinal and shear wave is reflected from the metagratings. Since not enough longitudinal wave is incident to the surface, additional time for performing the phenomenon is necessary for the metagrating structure. That is, additional time is essential for the structure to be in steady-state condition which is assumed in the harmonic analysis. After about $178\,\mu s$ later, a longitudinal wave is converted to the shear wave and almost no reflective longitudinal wave is observed in Fig. B1(b). For check the performance, we numerically calculated the total energy for a cycle in the incident longitudinal and reflected shear wave field. The power ratio of reflected shear wave to the incident longitudinal wave is calculated to be 0.975 which is slightly lower than the result of harmonic analysis which is 0.99. The cause of such gap between the results stems

from the difference between harmonic and transient analysis. Harmonic analysis assumes infinite cycle of incident wave, while transient analysis assumes a certain number of cycle of incident wave. Therefore, if numerous incident wave along with large analyzing time is used for the transient analysis, the efficiency can be overcome. Nevertheless, the proposed metagratings still show high performance compared to earlier works.

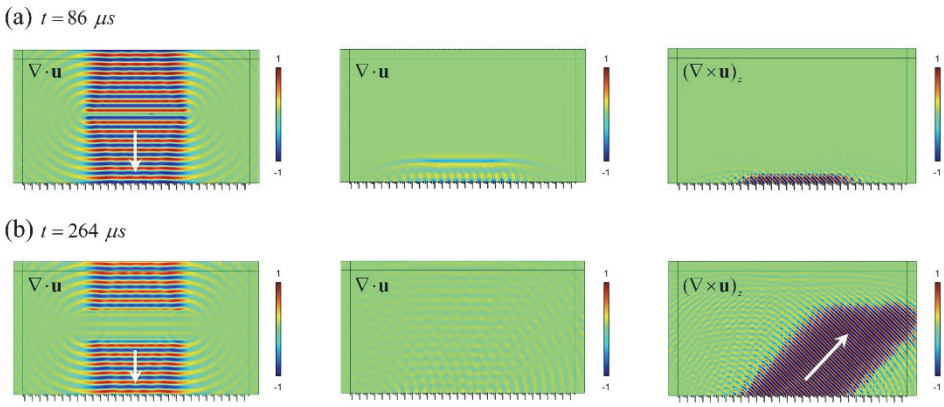

Fig. B.1 The transient analysis of mode-converting anomalous reflection. The transient simulation result at (a) $t = 86\ \mu s$, (b) $t = 264\ \mu s$.

APPENDIX C.

Effect of the number of beam-type members

Beam-type metagratings in chapter 3 are designed to manipulate high-order diffraction modes of longitudinal waves. And six beam-type members are used as general metagrating model. In this appendix, the effect of the number of beam-type members related with the performance of beam-type metagratings will be shown. In addition, the reason of choosing six beam-type members will also be discussed. As an example, the problem of anomalous longitudinal wave steering in Fig. 3.5 is solved. In this problem, normally incident longitudinal wave is reflected at the angle of 60°. In Fig. C1, such problem is solved using two, four, and six beam-type members. Beam-type members are equally distributed inside the unit cell length. For the performance, we adopted FFT in spatial domain to numerically analyzed the amplitudes of each diffraction mode. Performance of each set is compared using the -1st and 0th diffraction modes of longitudinal waves. We didn't consider shear waves in this chapter 3, therefore it is thought to be reasonable. As the number of beam-type members increase from two to six in Fig. C1, the amplitudes of -1st and 0th diffraction modes decreased. We can conclude that more than four beam-type members show high performance in longitudinal wave steering. In previous metagrating researches, the structure with more DOFs than the number of diffraction modes is designed to control wave steering [37]. In our problems, we proposed the general beam-type metagrating model for the general problem solution. In most of

the wave steering (and beam split) problems, the number of diffraction modes are calculated to be three to five. Therefore, we chose the six beam-type members which can control general wave steering problem. In addition, more than six beam-type members can be possible, but the number of beam-type members should also be minimalized for compactness.

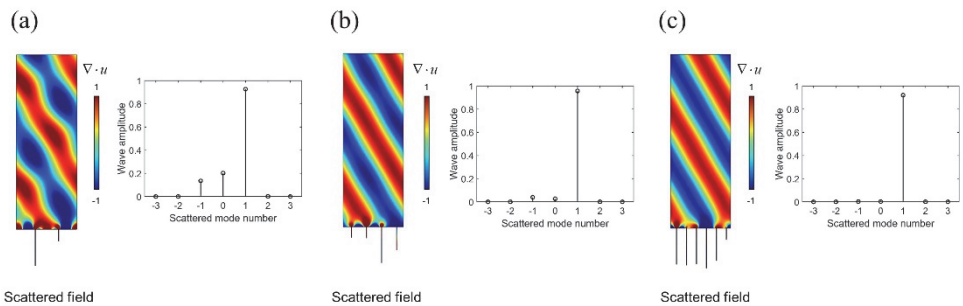

Fig. C.1 The performance of metagratings in the respect of the number of beam-type members. The problem is an anomalous longitudinal wave steering with the reflection angle of 60° in Fig. 3.5. The numerical simulation result are presented in both scattered divergence field and FFT in spatial domain using (a) two beam-type members, (b) four beam-type members, (c) six beam-type members.

APPENDIX D.

Effect of incidence angle on reflection angle of diffraction modes

We will analyze the effect of incident angle on reflection angle of diffraction modes. For a constant periodicity of metagratings as in Fig. 4.4(b) (See also Fig. 4.5(b)), every reflection angle can be obtained if incidence angle is well adjusted. However, for a given incidence angle, the possibility of reflection angle is checked in this part. By calculating diffraction grating theory, we can obtain the reflection angle respect to the unit cell length as in Fig. D1. If incidence angle and frequency is fixed, then the reflection angles of diffraction modes can only be changed by the periodicity of structures. So, we can check the possible reflection angle by changing the length of the unit cell. In Fig. D1(a), the reflection angle of all diffraction modes is presented with respect to periodicity for the normal incidence of longitudinal wave case. For simplicity, we will focus on incident longitudinal wave case. Similar result can be obtained for the incident shear wave case. Through the graph, we can conclude that every angle of reflection can be obtained when changing the unit cell length. However, in Fig. D1(b), we can get different form of graph when the longitudinal wave is obliquely incident. For the analysis, we used the 45° as an incidence angle. In this graph, we can see the lines of 0th modes act as vertical asymptotes. Therefore, between these 0th modes, no other reflection wave can be generated.

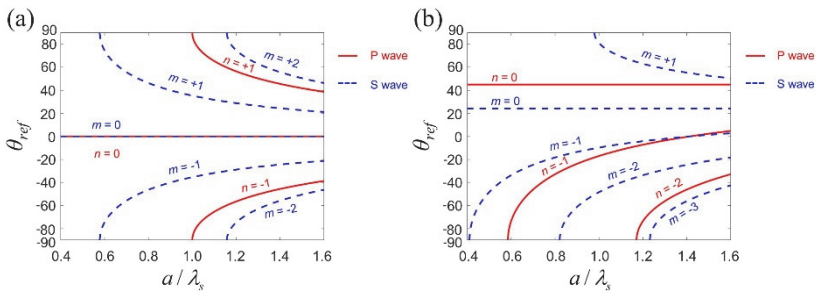

Fig. D.1 The reflection angle of diffraction modes with respect to the periodicity of structure. The longitudinal wave case for (a) normal incidence, (b) oblique incidence of 45°.

APPENDIX E.

Transfer matrix analysis of mode-converting specular reflection

The mode-converting specular reflection will be analyzed in this part using the transfer matrix method. In previous works, anisotropic metamaterial is designed to convert the elastic mode [19-24]. For analyzing anisotropic metamaterials, transfer matrix method is adopted to relate the anisotropic effective properties with the mode-converting phenomenon. In the same manner, we can adopt this transfer matrix analysis in our mode-converting specular reflection. The reflection problem in anisotropic medium is defined in Fig. E.1(a). The maximal reflective mode-conversion from the P wave to the S wave can be calculated from the transfer matrix and reformed as [19]:

$$d = n\frac{\lambda_{qp}}{2} = (2m-1)\frac{\lambda_{qs}}{4}, \quad (n,\ m:\ \text{integer}) \tag{E1}$$

where $\lambda_{qp}(\lambda_{qs})$ denotes quasi-longitudinal (quasi-shear) wave defined in an anisotropic effective medium, and d is the length of effective medium in reflection problem.

Then, proposed metagrating structure is homogenized into anisotropic medium as in Fig. E.1(b). In the effective medium length of 0.1 m, the property of anisotropic effective medium is determined to be $\rho_{eff} = 1308.0\ [\text{kg/m}^3]$,

$C_{11,eff} = 16.163\ [\text{GPa}]$, $C_{16,eff} = 3.6315\ [\text{GPa}]$, $C_{66,eff} = 18.162\ [\text{GPa}]$ at 120 kHz. Comparing theoretical and numerical values, the integer *n*, *m* in Eq. (E1) are approximately 15 and 5, respectively. Therefore, homogenization result and theoretical analysis show good agreement with each other. As a conclusion, we can explain the mode-converting specular reflection using anisotropic effective properties and transfer matrix analysis. However, the explanation for mode-converting anomalous reflection is still difficult with this method. In addition, if the correlation between the structure and anisotropic effective medium is found in the near future, then the analysis on elastic metagratings can be more strengthen.

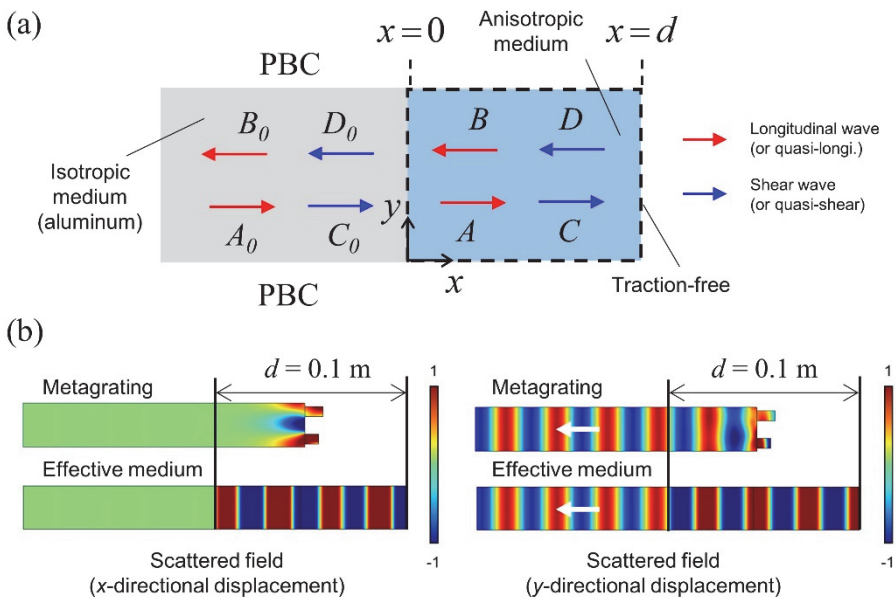

Fig. E.1 The reflection problem of anisotropic effective medium when longitudinal wave normally incidents. (a) The problem definition of reflection problem. (b) Homogenization result showing same performance as proposed metagratings.

REFERENCES

[1] C. R. Farrar and K. Worden, “An introduction to structural health monitoring”, *Philosophical Transactions of the Royal Society A*, 2007. **365**(1851): 303-315.

[2] P. Burrascano, S. Callegari, A. Montisci, M. Ricci, and M. Versaci, Ultrasonic nondestructive evaluation systems: industrial application issues, 2015: Springer International Publishing.

[3] J. L. Rose, Ultrasonic waves in solid media, 2004: Cambridge University Press.

[4] J. Miklowitz, The theory of elastic waves and waveguides, 2nd ed., 1980: North-Holland Publishing Company.

[5] Y. Liu and X. Zhang, “Metamaterials: a new frontier of science and technology”, *Chemical Society Reviews*, 2011. **40**(5): 2494-2507.

[6] J. Christensen, M. Kadic, M. Wegener, and O. Kraft, “Vibrant times for mechanical metamaterials”, *MRS Communications*, 2015. **5**: 453-462.

[7] S. A. Cummer, J. Christensen, and A. Alù, “Controlling sound with acoustic metamaterials”, *Nature Reviews Materials*, 2016. **1**: 16001.

[8] J. Jung, H. Park, J. Park, T. Chang, and J. Shin, “Broadband metamaterials and metasurfaces: a review from the perspectives of materials and devices”, *Nanophotonics*, 2020. **9**(10): 3165-3196.

[9] H.-T. Chen, A. J. Taylor, and N. Yu, “A review of metasurfaces: physics and

applications", *Reports on Progress in Physics*, 2016. **79**(7): 076401.

[10] B. Assouar, B. Liang, Y. Wu, Y. Li, J.-C. Cheng, and Y. Jing, "Acoustic metasurfaces", *Nature Reviews Materials*, 2018. **3**: 460-472.

[11] A-Li. Chen, Y.-S. Wang, Y.-F. Wang, H.-T. Zhou, and S.-M. Yuan, "Design of acoustic/elastic phase gradient metasurfaces: principles, functional elements, tenability, and coding", *Applied Mechanics Reviews*, 2022. **74**(2): 020801.

[12] Y. Ra'di and A. Alù, "Metagratings for efficient wavefront manipulation", *IEEE Photonics Journal*, 2022. **14**(1): 2207513.

[13] H. J. Lee, H. S. Lee, P. S. Ma, and Y. Y. Kim, "Effective material parameter retrieval of anisotropic elastic metamaterials with inherent nonlocality", *Journal of Applied Physics*, 2016. **120**(10): 104902.

[14] H. J. Lee, J.-R. Lee, S. H. Moon, T.-J. Je, E. Jeon, K. Kim, and Y. Y. Kim, "Off-centered double-slit metamaterial for elastic wave polarization anomaly", *Scientific Reports*, 2017. **7**: 15378.

[15] M. Zheng, C. I. Park, X. Liu, R. Zhu, G. Hu, and Y. Y. Kim, "Non-resonant metasurface for broadband elastic wave mode splitting", Applied Physics Letters, 2020. **116**(17): 171903.

[16] Y. Wu, Y. Lai, and Z.-Q. Zhang, "Elastic metamaterials with simultaneously negative effective shear modulus and mass density", *Physical Review Letters*, 2011. **107**(10): 105506.

[17] R. Zhu, X. N. Liu, G. K. Hu, C. T. Sun, and G. L. Huang, "Negative refraction

of elastic waves at the deep-subwavelength scale in a single-phase metamaterial", *Nature Communications*, 2014. **5**: 5510.

[18] S. W. Lee, H. M. Seung, W. Choi, M. Kim, and J. H. Oh, "Broad-angle refractive transmodal elastic metasurface", *Applied Physics Letters*, 2020. **117**(21): 213502.

[19] J. M. Kweun, H. J. Lee, J. H. Oh, H. M. Seung, and Y. Y. Kim, "Transmodal Fabry-Pérot resonance: theory and realization with elastic metamaterials", *Physical Review Letters*, 2017. **118**(20): 205901.

[20] X. Yang, J. M. Kweun, and Y. Y. Kim, "Theory for perfect transmodal Fabry-Perot interferometer", *Scientific Reports*, 2018. **8**: 69.

[21] X. Yang and Y. Y. Kim, "Topology optimization for the design of perfect mode-converting anisotropic elastic metamaterials", *Composite Structures*, 2018. **201**: 161-177.

[22] X. Yang and Y. Y. Kim, "Asymptotic theory of bimodal quarter-wave impedance matching for full mode-converting transmission", *Physical Review B*, 2018. **98**(14): 144110.

[23] X. Yang, M. Kweun, and Y. Y. Kim, "Monolayer metamaterial for full mode-converting transmission of elastic waves", *Applied Physics Letters*, 2019. **115**(7): 071901.

[24] J. Lee, M. Kweun, W. Lee, C. I. Park, and Y. Y. Kim, "Perfect transmission of elastic waves obliquely incident at solid-solid interfaces", *Extreme Mechanics Letters*, 2022. **51**: 101606.

[25] N. Yu, P. Genevet, M. A. Kats, F. Aieta, J.-P. Tetienne, F. Capasso, and Z. Gaburro, "Light propagation with phase discontinuities: generalized laws of reflection and refraction", *Science*, 2011. **334**(6054): 333-337.

[26] X. Su and A. N. Norris, "Focusing, refraction, and asymmetric transmission of elastic waves in solid metamaterials with aligned parallel gaps", *The Journal of the Acoustical Society of America*, 2016. **139**(6): 3386-3394.

[27] X. Su, Z. Lu, and A. N. Norris, "Elastic metasurfaces for splitting SV- and P-waves in elastic solids", *Journal of Applied Physics*, 2018. **123**(9): 091701.

[28] H. Lee, J. K. Lee, H. M. Seung, and Y. Y. Kim, "Mass-stiffness substructuring of an elastic metasurface for full transmission beam steering", *Journal of the Mechanics and Physics of Solids*, 2018. **112**: 577-593.

[29] L. Cao, Z. Yang, Y. Xu, S.-W. Fan, Y. Zhu, Z. Chen, B. Vincent, and B. Assouar, "Disordered elastic metasurfaces", *Physical Review Applied*, 2020. **13**(1): 014054.

[30] Y. Ra'di, D. L. Sounas, and A. Alù, "Metagratings: Beyond the limits of graded metasurfaces for wave front control", *Physical Review Letters*, 2017. **119**(6): 067404.

[31] M. Born and E. Wolf, Principles of optics – electromagnetic theory of propagation, interference and diffraction of light, 7th ed., 1999: Cambridge University Press.

[32] S. Larouche and D. R. Smith, "Reconciliation of generalized refraction with

diffraction theory", *Optics Letters*, 2012. **37**(12): 2391-2393.

[33] O. Rabinovich and A. Epstein, "Analytical design of printed circuit board (PCB) metagratings for perfect anomalous reflection", *IEEE Transactions on Antennas and Propagation*, 2018. **66**(8): 4086-4095.

[34] V. Popov, F. Boust, and S. N. Burokur, "Controlling diffraction patterns with metagratings", *Physical Review Applied*, 2018. **10**(1): 011002.

[35] D. Sell, J. Yang, S. Doshay, R. Yang, and J. A. Fan, "Large-angle, multifunctional metagratings based on freeform multimode geometries", Nano Letters, 2017. **17**(6): 3752-3757.

[36] Z. Zhang, M. Kang, X. Zhang, X. Feng, Y. Xu, X. Chen, H. Zhang, Q. Xu, Z. Tian, W. Zhang, A. Krasnok, J. Han, and A. Alù, "Coherent perfect diffraction in metagratings", *Advanced Materials*, 2020. **32**(36): 2002341.

[37] D. Torrent, "Acoustic anomalous reflectors based on diffraction grating engineering", *Physical Review B*, 2018. **98**(6): 060101(R).

[38] Y. Fu, Y. Cao, and Y. Xu, "Multifunctional reflection in acoustic metagratings with simplified design", *Applied Physics Letters*, 2019. **114**(5): 053502.

[39] Y. Fu, C. Shen. Y. Cao, L. Gao, H. Chen, C. T. Chan, S. A. Cummer, and Y. Xu, "Reversal of transmission and reflection based on acoustic metagratings with integer parity design", *Nature Communications*, 2019. **10**: 2326.

[40] Y. Jin, X. Fang, Y. Li, and D. Torrent, "Engineered diffraction gratings for acoustic cloaking", *Physical Review Applied*, 2019. **11**(1): 011004.

[41] H. Ni, X. Fang, Z. Hou, Y. Li, and B. Assouar, “High-efficiency anomalous splitter by acoustic meta-grating”, *Physical Review B*, 2019. **100**(10): 104104.

[42] Z. Hou, X. Fang, Y. Li, and B. Assouar, “Highly efficient acoustic metagrating with strongly coupled surface grooves”, *Physical Review Applied*, 2019. **12**(3): 034021.

[43] Y. Wang, Y. Cheng, and X. Liu, “Modulation of acoustic waves by a broadband metagrating”, *Scientific Reports*, 2019. **9**: 7271.

[44] S. R. Craig, X. Su, A. Norris, and C. Shi, “Experimental realization of acoustic bianisotropic gratings”, *Physical Review Applied*, 2019. **11**(6): 061002.

[45] L. Fan and J. Mei, “Metagratings for waterborne sound: various functionalities enabled by an efficient inverse-design approach”, *Physical Review Applied*, 2020. **14**(4): 044003.

[46] Y. K. Chiang, S. Oberst, A. Melnikov, L. Quan, S. Marburg, A. Alù, and D. A. Powell, “Reconfigurable acoustic metagrating for high-efficiency anomalous reflection”, *Physical Review Applied*, 2020. **13**(6): 064067.

[47] J. He, X. Jiang, D. Ta, and W. Wang, “Experimental demonstration of underwater ultrasound cloaking based on metagrating”, *Applied Physics Letters*, 2020. **117**(9): 091901.

[48] L. Fan and J. Mei, “Acoustic metagrating circulators: nonreciprocal, robust, and tunable manipulation with unitary efficiency”, *Physical Review Applied*, 2021. **15**(6): 064002.

[49] L. Fan and J. Mei, “Multifunctional waterborne acoustic metagratings: from extraordinary transmission to total and abnormal reflection”, *Physical Review Applied*, 2021. **16**(4): 044029.

[50] X. Fang, N. J. R. K. Gerard, Z. Zhou, H. Ding, N. Wang, B. Jia, Y. Deng, X. Wang, Y. Jing, and Y. Li, “Observation of higher-order exceptional points in a non-local acoustic metagrating”, *Communications Physics*, 2021. **4**: 271.

[51] Z. Hou, H. Ding, N. Wang, X. Fang, and Y. Li, “Acoustic vortices via nonlocal metagratings”, *Physical Review Applied*, 2021. **16**(1): 014002.

[52] Y. Lu, H. Zou, J. Qian, Y. Wang, Y. Ge, S. Yuan, H. Sun, and X. Liu, “Multifunctional reflected lenses based on aperiodic acoustic metagratings”, *Applied Physics Letters*, 2021. **119**(17): 173501.

[53] Y. K. Chiang, L. Quan, Y. Peng, S. Sepehrirahnama, S. Oberst, A. Alù, and D. A. Powell, “Scalable metagrating for efficient ultrasonic focusing”, *Physical Review Applied*, 2021. **16**(6): 064014.

[54] L.-S. Zeng, Y.-X. Shen, X.-S. Fang, Y. Li, and X.-F. Zhu, “Experimental realization of ultrasonic retroreflection tweezing via metagratings”, *Ultrasonics*, 2021. **117**: 106548.

[55] X. Li, D. Dong, J. Liu, Y. Liu, and Y. Fu, “Perfect retroreflection assisted by evanescent guided modes in acoustic metagratings”, *Applied Physics Letters*, 2022. **120**(15): 151701.

[56] A. Song, C. Sun, Y. Xiang, and F.-Z. Xuan, “Switchable acoustic metagrating

for three-channel retroreflection and carpet cloaking", *Applied Physics Express*, 2022. **15**(2): 024002.

[57] S. Bernard, F. Chikh-Bled, H. Kourchi, F. Chati, and F. Léon, "Broadband negative reflection of underwater acoustic waves from a simple metagrating: modeling and experiment", *Physical Review Applied*, 2022. **17**(2): 024059.

[58] P. Packo, A. N. Norris, and D. Torrent, "Inverse grating problem: efficient design of anomalous flexural wave reflectors and refractors", *Physical Review Applied*, 2019. **11**(1): 014023.

[59] P. Packo, A. N. Norris, and D. Torrent, "Metaclusters for the full control of mechanical waves", *Physical Review Applied*, 2021. **15**(1): 014051.

[60] Z. Tian and L. Yu, "Elastic phased diffraction gratings for manipulation of ultrasonic guided waves in solids", *Physical Review Applied*, 2019. **11**(2): 024052.

[61] S. Y. Kim, W. Lee, J. S. Lee, and Y. Y. Kim, "Longitudinal wave steering using beam-type elastic metagratings", *Mechanical Systems and Signal Processing*, 2021. **156**: 107688.

[62] Y. Hu, Y. Zhang, G. Su, M. Zhao, B. Li, Y. Liu, and Z. Li, "Realization of ultrathin waveguides by elastic metagratings", Communications Physics, 2022. **5**: 62.

[63] N. Yu and F. Capasso, "Flat optics with designer metasurfaces", *Nature Materials*, 2014. **13**: 139-150.

[64] A. V. Kildishev, A. Boltasseva, and V. M. Shalaev, “Planar photonics with metasurfaces”, *Science*, 2013. **339**(6125): 1232009.

[65] Y. Li, B. Liang, Z. Gu, X. Zou, and J. Cheng, “Reflected wavefront manipulation based on ultrathin planar acoustic metasurfaces”, *Scientific Reports*, 2013. **3**: 2546.

[64] Y. Li, X. Jiang, R. Li, B. Liang, X. Zou, L. Yin, and J. Cheng, “Experimental realization of full control of reflected waves with subwavelength acoustic metasurfaces”, *Physical Review Applied*, 2014. **2**(6): 064002.

[65] J. Zhao, B. Li, Z. Chen, and C.-W. Qiu, “Manipulating acoustic wavefront by inhomogeneous impedance and steerable extraordinary reflection”, *Scientific Reports*, 2013. **3**: 2537.

[66] Y.-F. Zhu, X.-Y. Zou, R.-Q. Li, X. Jiang, J. Tu, B. Liang, and J.-C. Cheng, “Dispersionless manipulation of reflected acoustic wavefront by subwavelength corrugated surface”, *Scientific Reports*, 2015. **5**: 10966.

[67] Y.-F. Zhu and B. Assouar, “Multifunctional acoustic metasurface based on an array of Helmholtz resonators”, *Physical Review B*, 2019. **99**(17): 174109.

[68] C. Pfeiffer and A. Grbic, “Metamaterial Huygens’ surfaces: Tailoring wave fronts with reflectionless sheets”, *Physical Review Letters*, 2013. **110**(19): 197401.

[69] F. Monticone, N. M. Estakhri, and A. Alù, “Full control of nanoscale optical transmission with a composite metascreen”, *Physical Review Letters*, 2013. **110** (20): 203903.

[70] F. Aieta, M. A. Kats, P. Genevet, and F. Capasso, "Multiwavelength achromatic metasurfaces by dispersive phase compensation", *Science*, 2015. **347**(6228): 1342-1345.

[71] J. Mei and Y. Wu, "Controllable transmission and total reflection through an impedance-matched acoustic metasurface", *New Journal of Physics*, 2014. **16**: 123007.

[72] K. Tang, C. Qiu, M. Ke, J. Lu, Y. Ye, and Z. Liu, "Anomalous refraction of airborne sound through ultrathin metasurfaces", *Scientific Reports*, 2014. **4**: 6517.

[73] Y. Tian, Q. Wei, Y. Cheng, Z. Xu, and X. Liu, "Broadband manipulation of acoustic wavefronts by pentamode metasurface", *Applied Physics Letters*, 2015. **107**(22): 221906.

[74] Y. Li, S. Qi, and M. B. Assouar, "Theory of metascreen-based acoustic passive phased array", *New Journal of Physics*, 2016. **18**: 043024.

[75] H. Zhu and F. Semperlotti, "Anomalous refraction of acoustic guided waves in solids with geometrically tapered metasurfaces", *Physical Review Letters*, 2016. **117**(3): 034302.

[76] A. Arbabi, E. Arbabi, Y. Horie, S. M. Kamali, and A. Faraon, "Planar metasurface retroreflector", *Nature Photonics*, 2017. **11**: 415-520.

[77] C. Shen, A. Díaz-Rubio, J. Li, and S. A. Cummer, "A surface impedance-based three-channel acoustic metasurface retroreflector", *Applied Physics Letters*, 2018. **112**(18): 183503.

[78] G. Y. Song, Q. Cheng, T. J. Cui, and Y. Jing, "Acoustic planar surface retroreflector", *Physical Review Materials*, 2018. **2**(6): 065201.

[79] Y. Ruan, X. Liang, and C. Hu, "Retroreflection of flexural wave by using elastic metasurface", *Journal of Applied Physics*, 2020. **128**(4): 045116.

[80] P. Zhang, T. Li, J. Zhu, X. Zhu, S. Yang, Y. Wang, X. Yin, and X. Zhang, "Generation of acoustic self-bending and bottle beams by phase engineering", *Nature Communications*, 2014. **5**: 4316.

[81] Y. Li, X. Jiang, B. Liang, J. Cheng, and L. Zhang, "Metascreen-based acoustic passive phased array", *Physical Review Applied*, 2015. **4**(2): 024003.

[82] Y. Li and M. B. Assouar, "Three-dimensional collimated self-accelerating beam through acoustic metascreen", *Scientific Reports*, 2015. **5**: 17612.

[83] S. Zhai, H. Chen, C. Ding, F. Shen, C. Luo, and X. Zhao, "Manipulation of transmitted wave front using ultrathin planar acoustic metasurfaces", *Applied Physics A*, 2015. **120**: 1283-1289.

[84] D.-C. Chen, X.-F. Zhu, Q. Wei, D.-J. Wu, and X.-J. Liu, "Broadband acoustic focusing by Airy-like beams based on acoustic metasurfaces", *Journal of Applied Physics*, 2018. **123**(4): 044503.

[85] H. Esfahlani, H. Lissek, and J. R. Mosig, "Generation of acoustic helical wavefronts using metasurfaces", *Physical Review B*, 2017. **95**(2): 024312.

[86] X. Jiang, B. Liang, X. Zou, J. Yang, L. Yin, J. Yang, and J. Cheng, "Acoustic one-way metasurfaces: asymmetric phase modulation of sound by subwavelength

layer", *Scientific Reports*, 2016. **6**: 28023.

[87] C. Shen, Y. Xie, J. Li, S. A. Cummer, and Y. Jing, "Asymmetric acoustic transmission through near-zero-index and gradient-index metasurfaces", *Applied Physics Letters*, 2016. **108**(22): 223502.

[88] X.-P. Wang, L.-L. Wan, T.-N. Chen, Q.-X. Liang, and A.-L. Song, "Broadband acoustic diode by using two structured impedance-matched acoustic metasurfaces", *Applied Physics Letters*, 2016. **109**(4): 044102.

[89] Y. Xie, C. Shen, W. Wang, J. Li, D. Suo, B.-I. Popa, Y. Jing, and S. A. Cummer, "Acoustic holographic rendering with two-dimensional metamaterial-based passive phased array", *Scientific Reports*, 2016. **6**: 35437.

[90] Y. Zhu, J. Hu, X. Fan, J. Yang, B. Liang, X. Zhu, and J. Cheng, "Fine manipulation of sound via lossy metamaterials with independent and arbitrary reflection amplitude and phase", *Nature Communications*, 2018. **9**: 1632.

[91] Y. Yang, H. Wang, F. Yu, Z. Xu, and H. Chen, "A metasurface carpet cloak for electromagnetic, acoustic and water waves", *Scientific Reports*, 2016. **6**: 20219.

[92] H. Esfahlani, S. Karkar, H. Lissek, and J. R. Mosig, "Acoustic carpet cloak based on an ultrathin metasurface", *Physical Review B*, **94**(1): 014302.

[93] C. Faure, O. Richoux, S. Félix, and V. Pagneux, "Experiments on metasurface carpet cloaking for audible acoustics", *Applied Physics Letters*, 2016. **108**(6): 064103.

[94] S. Zhai, H. Chen, C. Ding, L. Li, F. Shen, C. Luo, and X. Zhao, "Ultrathin skin

cloaks with metasurfaces for audible sound", *Journal of Physics D: Applied Physics*, **49**(22): 225302.

[95] A. Epstein and O. Rabinovich, "Unveiling the properties of metagratings via a detailed analytical model for synthesis and analysis", *Physical Review Applied*, 2017. **8**(5): 054037.

[96] L. Quan, Y. Ra'di, D. L. Sounas, and A. Alù, "Maximum Willis coupling in acoustic scatterers", *Physical Review Letters*, 2018. **120**(25): 254301.

[97] A. M. H. Wong and G. V. Eleftheriades, "Perfect anomalous reflection with a bipartite Huygens' metasurface", *Physical Review X*, 2018. **8**(1): 011036.

[98] K. Kim, C. I. Park, H. Lee, and Y. Y. Kim, "Near-zero effective impedance with finite phase velocity for sensing and actuation enhancement by resonator pairing", *Nature Communications*, 2018. **9**: 5255.

[99] S. Asano, "Reflection and refraction of elastic waves at a corrugated interface", *Bulletin of the Seismological Society of America*, 1966. **56**(1): 201-221.

[100] K. F. Graff, Wave motion in elastic solids, 1991: Dover Publications.

[101] D. J. Colquitt, A. Colombi, R. V. Craster, P. Roux, and S. R. L. Guenneau, "Seismic metasurfaces: sub-wavelength resonators and Rayleigh wave interaction", *Journal of the Mechanics and Physics of Solids*, 2017. **99**: 379-393.

[102] K. Svanberg, "The method of moving asymptotes-a new method for structural optimization", International Journal for Numerical Methods in Engineering, 1987. **24**: 359-373.

[103] H. Lee, J. H. Oh, H. M. Seung, S. H. Cho, and Y. Y. Kim, "Extreme stiffness hyperbolic elastic metamaterial for total transmission subwavelength imaging", *Scientific Reports*, 2016. **6**: 24026.

[104] Y. Y. Kim and Y. E. Kwon, "Review of magnetostrictive patch transducers and applications in ultrasonic nondestructive testing of waveguides", *Ultrasonics*, 2015. **62**: 3-19.

[105] D. A. Simons, "Reflection of Rayleigh waves by strips, grooves, and periodic arrays of strips or grooves", *The Journal of the Acoustical Society of America*, 1978. **63**(5): 1292.

[106] E. O. Brigham, The fast Fourier transform, 1974: Prentice-Hall.

[107] J. S. Lee, J. E. Kim, and Y. Y. Kim, "Damage detection by the topology design formulation using modal parameters", International Journal for Numerical Methods in Engineering, 2007. **69**: 1480-1498.

[108] B. Ahn, H. Lee, J. S. Lee, and Y. Y. Kim, "Topology optimization of metasurfaces for anomalous reflection of longitudinal elastic waves", *Computer Methods in Applied Mechanics and Engineering*, 2019. **357**: 112582.

[109] W. U. Yoon, J. H. Park, J. S. Lee, and Y. Y. Kim, "Topology optimization design for total sound absorption in porous media", *Computer Methods in Applied Mechanics and Engineering*, 2020. **360**: 112723.

[110] K. K. Choi and N. H. Kim, Structural sensitivity analysis and optimization 1: linear system, 2005: Springer-Verlag.

[111] C. Piao, X. Yang, J. M. Kweun, H. Kim, H. Park, S. H. Cho, and Y. Y. Kim, "Ultrasonic flow measurement using a high-efficiency longitudinal-to-shear wave mode-converting meta-slab wedge", *Sensors and Actuators A: Physical*, 2020. **310**: 112080.

[112] V. S. Asadchy, M. Albooyeh, S. N. Tcvetkova, A. Díaz-Rubio, Y. Ra'di, and S. A. Tretyakov, "Perfect control of reflection and refraction using spatially dispersive metasurfaces", *Physical Review B*, 2016. **94**(7): 075142.

[113] S. Y. Kim, Y. B. Oh, J. S. Lee, and Y. Y. Kim, "Anomalous mode-converting reflection of elastic waves using strip-type metagratings", *Mechanical Systems and Signal Processing*, 2023. **186**: 109867.

[114] K. Yi, M. Ouisse, E. Sadoulet-Reboul, and G. Matten, "Active metamaterials with broadband controllable stiffness for tunable band gaps and non-reciprocal wave propagation", *Smart Materials and Structures*, 2019. **28**: 065025.

ABSTRACT (KOREAN)

특이 파동 조향 및 모드 변환을 위한 반사형 탄성 메타그레이팅

김 신 영
서울대학교 대학원
기계항공공학부

본 연구에서는 특이 파동 조향 및 모드 변환을 위한 반사형 탄성 메타그레이팅을 다룬다. 탄성 메타그레이팅은 회절 격자 이론을 탄성 메타물질의 개념에 도입하여 새롭게 설계되는 인공적인 구조물을 말한다. 최근 들어 탄성 파동의 전파 특성을 효과적으로 조절할 수 있는 주기적인 구조물로서 탄성 메타물질이 주목받고 있다. 이와 같은 탄성 메타물질은 탄성 파동 및 진동을 제어하여 환자의 치료, 비파괴검사, 흡진 등을 목표로 광범위한 산업계에서 실용적으로 이용될 수 있다. 하지만 주기적인 구조물의 특성상 반사 또는 투과하는 파동의 회절 및 간섭 현상이 필연적으로 발생하며, 고차 회절 모드의 발생으로 인한 파동의 효율 저하 문제는 해결책에 있어서 여전히 본질적인 한계점을 지니고 있다. 이러한

한계를 극복하기 위해, 본 연구에서는 파면이 설계된 대로 정확하게 조향될 수 있도록 탄성 파동의 각 회절 모드별 크기 및 방향을 정밀하게 조절 가능한 반사형 탄성 메타그레이팅을 새롭게 제안한다.

본 연구에서는 일반적인 탄성 매질의 반사 문제에서 종파 및 횡파의 특이 파동 조향 및 모드 변환을 목표로 한다. 잘 설계된 탄성 메타그레이팅을 도입함으로써 태생적으로 발생하는 반사 파동의 효율 저하 문제를 해결하고자 한다. 이러한 반사 문제는 두 단계를 통해 해결되었다. 해결을 위한 첫 번째 단계에서는, 횡파의 고려없이 종파만을 제어하는 단일 모드 파동 제어 문제를 해결하였다. 이때, 다수의 빔-타입 부재를 탄성 파동 산란자로 사용하며, 이론적으로 모델링한 빔-타입 부재를 이용하여 잘 설계된 탄성 메타그레이팅을 통해 산란하는 종파의 제어 현상을 구현한다. 하지만 빔-타입 메타그레이팅은 그 설계 변수가 적으며, 굽힘 및 종적인 운동만 가능한 가느다란 형상으로 인하여 종파와 횡파의 다양한 회절 모드를 제어하기 어렵다. 이에 두 번째 단계에서는, 종파(또는 횡파)를 모드 변환하면서 동시에 조향하는 이중 모드 파동 제어 문제를 해결하는 데에 있어 파동 산란자로 부재의 폭 등이 고려되어 자유도가 보다 많은 스트립-타입 연속체 부재를 사용한다. 이 단계에서는 수치해석으로 구한 해를 바탕으로 종파와 횡파의 모드별 크기를 정량화하고, 이를 통해 탄성 파동을 모드 변환하면서 조향할 수 있는 스트립-타입 메타그레

이팅을 이용하여 현상을 구현한다. 정리하면, 최종 목표를 달성하기 위해, 두 단계로 나누어 반사형 탄성 메타그레이팅의 설계 방법을 제시하고, 이를 통해 탄성 파동의 고차 회절 모드를 제어하여 특이 파동 조향 및 모드 변환 현상을 구현한다. 본 연구는 각 단계에서 관련된 물리 현상을 분석하여 현상을 규명하며, 실험적으로 검증할 뿐만 아니라, 실제 초음파 비파괴검사 산업에서 적용 가능한 어플리케이션을 제시하여 탄성 메타그레이팅 실용화의 가능성을 열었다는 측면에서 그 의의가 있다.

주요어: 탄성 메타그레이팅, 회절 격자 이론, 특이 파동 조향,
탄성 모드 변환, 탄성 파동 산란자

학 번 : 2016-22851

ACKNOWLEDGEMENTS

This research was supported by the National Research Foundation of Korea (NRF) grant [No. 2014M3A6B3063711 and 2021R1F1A1063190] funded by the Korea Ministry of Science, ICT & Future Planning (MSIP) each contracted through the Institute of Advanced Machines and Design (IAMD) at Seoul National University in Korea and Chungnam National University in Korea, respectively. Furthermore, this research was supported by research fund of Chungnam National University and by the Basic Science Research Program [2018R1D1A1B07049771] funded by the Korea Ministry of Education, contracted through Chungnam National University in Korea.